



INTERNATIONAL ATOMIC ENERGY AGENCY

**INDC(BLR)-020**

**Distr. J+TU/EL**

---

**I N D C    I N T E R N A T I O N A L   N U C L E A R   D A T A   C O M M I T T E E**

---

**Neutron Data Evaluation of  $^{233}\text{Pa}$**

V.M. Maslov<sup>1</sup>, M. Baba<sup>2</sup>,  
A. Hasegawa<sup>3</sup>, N.V. Kornilov<sup>1\*</sup>, A.B. Kagalenko<sup>1\*</sup>,  
N.A. Tetereva<sup>1</sup>

- <sup>1)</sup> Joint Institute of Nuclear and Energy Research – SOSNY  
220109, Minsk-Sosny, Belarus
- <sup>2)</sup> Cyclotron and Radioisotope Center, Tohoku University,  
Sendai, Japan
- <sup>3)</sup> Department of Nuclear Energy System, Tokai Research  
Establishment, Japan Atomic Energy Research Institute,  
Tokai-mura, Naka-gun, Ibaraki-ken
- <sup>\*)</sup> Permanent address: Institute of Physics and Power Engineering,  
249020, Obninsk, Russia

February 2004

Documents in the EL series are available in only limited quantities in hardcopy form. They may be downloaded in electronic form from [http://www-nds.iaea.org.at/indc\\_sel.html](http://www-nds.iaea.org.at/indc_sel.html) or sent as an e-mail attachment. Requests for hardcopy or e-mail transmittal should be directed to [services@iaeand.iaea.org](mailto:services@iaeand.iaea.org) or to:

Nuclear Data Section  
International Atomic Energy Agency  
PO Box 100  
Wagramer Strasse 5  
A-1400 Vienna  
Austria

Produced by the IAEA in Austria  
February 2004

# Neutron Data Evaluation of $^{233}\text{Pa}$

V.M. Maslov<sup>1</sup>, M. Baba<sup>2</sup>,  
A.Hasegawa<sup>3</sup>, N.V. Kornilov<sup>1,\*</sup>, A. B. Kagalenko<sup>1,\*</sup>,  
N.A. Tetereva<sup>1</sup>

<sup>1</sup>) Joint Institute for Nuclear and Energy Research,  
220109, Minsk-Sosny, Belarus

<sup>2</sup>) Cyclotron and Radioisotope Center, Tohoku  
University, Sendai, Japan

<sup>3</sup>) Department of Nuclear Energy System, Tokai  
Research Establishment, Japan Atomic Energy  
Research Institute, Tokai-mura, Naka-gun, Ibaraki-ken

## Abstract

Consistent evaluation of  $^{233}\text{Pa}$  measured data base is performed. Hauser-Feshbach-Moldauer theory, coupled channel model and double-humped fission barrier model are employed. Total, differential scattering, fission and (n,xn) data are calculated, using fission cross section data description as a major constraint. The direct excitation of ground state band levels is calculated within rigid rotator model. Average resonance parameters are provided, which reproduce evaluated cross sections in the range of 16.5 -70.9 keV.

This work is performed under the Project Agreement B-404 with the International Science and Technology Center (Moscow). The Financing Party for the Project is Japan.

\*) Permanent address: Institute of Physics and Power Engineering, 249020, Obninsk, Russia



# Contents

<b>1</b>	<b>Introduction</b>	<b>5</b>
<b>2</b>	<b>Resolved resonance energy range</b>	<b>5</b>
<b>3</b>	<b>Unresolved resonance region</b>	<b>6</b>
3.1	Average resonance parameters . . . . .	7
3.1.1	Neutron resonance spacing . . . . .	7
3.1.2	Neutron width . . . . .	7
3.1.3	Radiative capture width . . . . .	7
3.1.4	Neutron inelastic width . . . . .	8
3.1.5	Fission width . . . . .	8
3.2	Average cross sections in the region 16.5 eV-70.9 keV . . . . .	8
3.2.1	Total cross section . . . . .	8
3.2.2	Elastic scattering cross section . . . . .	9
3.2.3	Fission cross section . . . . .	9
3.2.4	Capture cross section . . . . .	9
3.2.5	Inelastic scattering cross section . . . . .	9
3.2.6	Comparison of average resonance parameters . . . . .	10
<b>4</b>	<b>Optical Potential</b>	<b>10</b>
4.1	Total and elastic cross sections . . . . .	11
<b>5</b>	<b>Statistical Model</b>	<b>11</b>
5.1	Level Density . . . . .	12
5.2	Fission Cross Section . . . . .	15
5.3	Fission Channel . . . . .	15
5.3.1	Fission transmission coefficient, level density and transition state spectrum . . . . .	16
5.4	Fission Data Analysis . . . . .	16
5.5	Inelastic Scattering . . . . .	17
5.6	Neutron Channel . . . . .	17
5.7	Ground State Rotational Band . . . . .	17
5.8	Total inelastic cross section . . . . .	18
<b>6</b>	<b>Capture cross section</b>	<b>19</b>
<b>7</b>	<b>Cross sections above emissive fission threshold</b>	<b>20</b>
7.1	Fission cross section . . . . .	20
7.2	$^{233}\text{Pa}(\text{n},\text{xn})$ cross section . . . . .	22

<b>8</b>	<b>Neutron emission spectra</b>	<b>23</b>
8.1	Prompt fission neutron number $\nu_p$ . . . . .	23
8.2	Prompt fission neutron spectra . . . . .	24
8.2.1	Model for PFNS evaluation . . . . .	24
8.2.2	Pre-fission (n,xnf) neutron spectra . . . . .	26
8.2.3	Comparison with previous evaluations . . . . .	26
8.3	Neutron emission spectra comparison . . . . .	27
<b>9</b>	<b>Conclusions</b>	<b>29</b>
<b>10</b>	<b>Acknowledgments</b>	<b>29</b>
<b>11</b>	<b>Figure captions</b>	<b>33</b>

# 1 Introduction

Protactinium-233 is a precursor of  $^{233}\text{U}$  in uranium-thorium-fueled nuclear reactors. It is formed after capture of neutrons by  $^{232}\text{Th}$  and two subsequent  $\beta^-$ -decays, i.e.  $^{232}\text{Th}(\text{n},\gamma)^{233}\text{Th}(\beta^-)^{233}\text{Pa}(\beta^-)^{233}\text{U}$ . Because of  $\beta$ -decay half-life of 27 days,  $^{233}\text{Pa}$  inventory is very important for the reactor reactivity control. There is almost no measured neutron data for the  $^{233}\text{Pa}$ , except capture cross section at thermal point, one fission data point, measured for the fast neutron spectrum [1] and two fission data sets [2, 3, 4], which do not seem to be fully compatible. Application of the Hauser-Feshbach statistical model for the analysis of neutron-induced fission data [2, 3] and  $^{233}\text{Pa}(\text{n},\text{f})$  fission data [4], extracted from the transfer reaction  $^{232}\text{Th}(^3\text{He},\text{p})^{234}\text{Pa}$  would be of much interest. Fission data description would maintain almost the only constraint for the  $^{233}\text{Pa}$  capture, neutron elastic and inelastic scattering,  $(\text{n},2\text{n})$ ,  $(\text{n},3\text{n})$  and secondary neutron spectra evaluation. Current approach was validated recently in case of  $^{238}\text{U}$ ,  $^{232}\text{U}$ ,  $^{233}\text{U}$ ,  $^{234}\text{U}$ ,  $^{232}\text{Th}$  and  $^{231}\text{Pa}$  neutron data description [5, 6, 7, 8, 9].

## 2 Resolved resonance energy range

Here we will briefly review the status of resolved neutron resonance parameters of  $^{233}\text{Pa}$ . Resolved resonance region of ENDF/B-VI [10] data file extends up to 38.5 eV. Resolved resonance parameters were adopted from Simpson et al. [11] (28 resonances in the range of 0-17.5 eV) and Harris [12] (12 resonances in the range of 17.5 -37.5 eV), resolved resonance parameters are assumed to be single-level Breit-Wigner parameters. Thermal capture and fission cross sections are shown in Table 1.

Region of resolved resonances in JENDL-3.3 [13] extends up to 16.5 eV, neutron and radiative widths were adopted from Mughabghab [14] and modified to reproduce thermal cross sections and capture integral, recommended by Mughabghab [14]. A bound level was placed at  $E_r = -0.18$  eV to reproduce thermal total, fission, elastic and capture cross section of BNL-325 [14].

The resonance parameters of JENDL-3.3 [13], basically accepted in present data file of  $^{233}\text{Pa}$ , might provide a test of neutron width and resonance spacing distributions. We performed a resonance parameter analysis based on maximum likelihood estimates [15] both of mean level spacing  $\langle D_{l=0} \rangle$  and neutron strength function  $S_o$ . Correction for the missing of levels based on simultaneous analysis of level spacing distribution and neutron width distribution gives estimates of average  $s$ -wave neutron resonance spacing  $\langle D_{l=0} \rangle = 0.503 \pm 0.095$  eV (see Fig. 1) and strength function estimate  $S_o = 0.8007 \times 10^{-4}$ . This estimate is lower than Reference Input Parameter Library File [16] recommendation ( $\langle D_{l=0} \rangle = 0.7 \pm 0.10$  eV), but compatible with  $\langle D_{l=0} \rangle = 0.59$  eV value, adopted in JENDL-3.3 [13] data file. Cumulative sum of reduced neutron widths of  $s$ -resonances  $\Gamma_n^o$  is compared

with present strength function estimate of  $S_o = (0.8007) \times 10^{-4}$  on Fig. 2.

The resolution function parameters as well as  $\langle \Gamma_n^o \rangle$  and  $\langle D_{l=0} \rangle$  are obtained by maximum likelihood method when comparing experimental distributions of reduced neutron width and resonance spacing with Porter-Thomas and Wigner distributions, modified for the resonance missing. The latter distributions will be called expected distributions. Figures 3 and 4 demonstrate the comparison of predicted level spacing  $D_{l=0}$  and reduced neutron width  $\Gamma_n^o$  distributions with present resonance parameter set. Quantiles on Fig. 3 show eight equal probability intervals ( $P(x \leq x_{0.125} = \int p(x)dx = 0.125$ ) for expected level spacing distribution of  $s$ -wave resonances  $D_{l=0}$ . Expected level spacing distribution, which takes into account missing of weak resonances and unresolved doublets, is compatible with experimental distribution. Expected distribution is qualitatively similar to Wigner distribution. Quantiles on Fig. 4 show eight equal probability ( $P(x \leq x_{0.125} = \int p(x)dx = 0.125$ ) intervals for  $\Gamma_n^o$  expected distribution. It demonstrates that reduced neutron width distribution with account of missing is compatible with observed distribution also in the range of small reduced neutron width values.

Figure 5 shows a comparison of experimental distribution of reduced neutron widths with cumulative Porter-Thomas distribution of reduced neutron widths with (expected distribution) and without resonance missing correction. Cumulative Porter-Thomas distribution of reduced neutron widths without resonance missing correction (solid line on Fig. 5) is plotted for the number of resonances  $N=25$ , which takes into account present estimate of missing 4 levels.

Table 1  
Thermal cross sections and resonance integrals

Reaction	$\sigma^{th}$ , barns	RI	$\sigma^{th}$ , barns	RI	$\sigma^{th}$ , barns	RI	$\sigma^{th}$ , barns	RI
	Present		JENDL-3.3 [13]		ENDF/B-VI [10]		BNL-325 [14]	
Total	53.05	-	53.051	-				
Elastic	13.02	-	13.021					
Fission		1.61	0	2.1	0.01			
Capture	40.03	878.89	40.031	864	227	41.4605		

### 3 Unresolved resonance region

Here we will briefly review the status of unresolved neutron resonance parameters of  $^{233}\text{Pa}$  and provide a cross section parameterization of total, capture, elastic and inelastic scattering cross sections.

The unresolved resonance energy region of ENDF/B-VI [10] extends from 38.8 eV up to 10 keV. Provided are energy independent average  $s$ -wave resonance parameters  $\langle D_{J=1} \rangle = 1.5238$  eV,  $\langle D_{J=2} \rangle = 0.91427$  eV, which give  $\langle D \rangle = 0.5714$  eV,  $\langle \Gamma_\gamma \rangle = 0.055$  eV and  $\langle \Gamma_f \rangle = 0$ .



In JENDL-3.3 [13] unresolved resonance region extends from 16.5 eV up to 40 keV. Provided are energy independent average resonance parameters for  $s$ - and  $p$ -wave neutrons,  $\langle D_{J=1} \rangle = 1.5733$  eV,  $\langle D_{J=2} \rangle = 0.944$  eV, which give  $\langle D \rangle = 0.59$  eV, fission width  $\langle \Gamma_f \rangle$  being equal to zero, while  $\langle \Gamma_\gamma \rangle = 0.047$  eV are adopted. However, radiation strength function was estimated for  $\langle D \rangle = 0.79$  eV and  $\langle \Gamma_\gamma \rangle = 0.040$  eV

We assume that lower energy of unresolved resonance energy region in present evaluation is the end-point of resolved resonance region, i.e. 16.5 eV, the upper energy is 70.9 keV, twice lower, than in our recent evaluations of  $^{238}\text{U}$  and  $^{232}\text{Th}$  [6, 7, 8]. We suppose  $s$ -,  $p$ - and  $d$ -wave neutron-nucleus interactions to be effective.

### 3.1 Average resonance parameters

Average resonance parameters  $S_o = 0.8007 \times 10^{-4}$ ,  $\langle D_{l=0} \rangle = 0.503$  eV,  $\langle \Gamma_\gamma \rangle = 47$  meV are used for the cross section calculation from 16.5 eV up to 70.9 keV.

#### 3.1.1 Neutron resonance spacing

Neutron resonance spacing  $\langle D_J \rangle$  was calculated with the phenomenological model [17], which takes into account the shell, pairing and collective effects. The main parameter of the model, asymptotic value of level density parameter  $\tilde{a}$ , was normalized to the observed neutron resonance spacing  $\langle D_{l=0} \rangle = 0.503$  eV.

#### 3.1.2 Neutron width

Average neutron width is calculated as follows

$$\langle \Gamma_n^{lJ} \rangle = S_l \langle D_J \rangle E_n^{1/2} P_l \nu_n^{lJ}, \quad (1)$$

where  $E_n$  is the incident neutron energy,  $P_l$  is the transmission factor for the  $l$ -th partial wave, which was calculated within black nucleus model,  $\nu_n^{lJ}$  is the number of degrees of freedom of Porter-Thomas distribution (see Table 2). The  $p$ -wave neutron strength function  $S_1 = 1.5136 \times 10^{-4}$  at 16.5 eV was calculated with the optical model, using the deformed optical potential, described below.

#### 3.1.3 Radiative capture width

Energy and angular momentum dependence of radiative capture width are calculated within a two-cascade  $\gamma$ -emission model with allowance for the  $(n, \gamma n')$  [18] and  $(n, \gamma f)$  [19] reactions competition to the  $(n, \gamma \gamma)$  reaction. The  $(n, \gamma \gamma)$  reaction is supposed to be a radiative capture reaction. The radiative capture width was normalized to the value of  $\langle \Gamma_\gamma \rangle = 47$  meV.

### 3.1.4 Neutron inelastic width

Average neutron inelastic width is calculated as follows

$$\langle \Gamma_{n'}^{lJ} \rangle = S_l \langle D_J \rangle (E_n - E')^{1/2} P_l(E_n - E') \nu_{n'}^{lJ}, \quad (2)$$

where  $\nu_{n'}^{lJ}$  is number of degrees of freedom of Porter-Thomas distribution (see Table 2).

### 3.1.5 Fission width

Fission widths are calculated within a double-humped fission barrier model. Energy and angular momentum dependence of fission width is defined by the transition state spectra at inner and outer barrier humps. We constructed transition spectra by supposing the axially of inner saddle and mass asymmetry at outer saddle [16, 20]. Number of degrees of freedom  $\nu_f^{lJ}$  of Porter-Thomas distribution is defined in Table 2. They will be described below.

Table 2.  
Number of degrees of freedom

$l, J$	$\nu_{n'}^{lJ}$	$\nu_n^{lJ}$	$\nu_f^{lJ}$
0,1	2	1	2
0,2	1	1	2
1,0	2	1	1
1,1	1	2	2
1,2	2	2	2
1,3	2	1	2
2,0	1	1	1
2,1	2	2	2
2,2	1	2	2
2,3	2	2	2
2,4	1	1	2

## 3.2 Average cross sections in the region 16.5 eV-70.9 keV

### 3.2.1 Total cross section

There is no total cross section measurements above 10 keV, only rather old data at lower energies [11]. Above 10 keV total cross section was estimated assuming a decreasing trend of  $S_o$  and  $S_1$  strength function values as the latter and potential radius, which was adopted from the optical model calculations, define

total cross section up  $E_n = 70.9$  keV. To reproduce total cross section, calculated with optical model, we assume  $S_o$  value linearly decreasing starting from 10 keV to  $0.7543 \times 10^{-4}$ , while  $S_1$  to  $1.5207 \times 10^{-4}$  at 70.9 keV (see Fig. 6). The  $d$ -wave neutron strength function was assumed to be equal to  $S_2 = 1.0832 \times 10^{-4}$ . In JENDL-3.3 [13] evaluation the potential scattering radius is  $R = 10.092$  fm, while in ENDF/B-VI [10]  $R = 8.9184$  fm, we assumed  $R = 9.486$  fm, it is consistent with the coupled channel optical model calculations.

### 3.2.2 Elastic scattering cross section

Elastic scattering cross section estimate is rather insensitive to the  $^{233}\text{Pa}$  fission cross section estimate. The discrepancy of present, ENDF/B-VI [10] and JENDL-3.3 [13] estimates from  $\sim 16.5$  eV and up to  $\sim 70$  keV, shown on Fig. 7, appears to be correlated with the different estimates of potential scattering radius  $R$ .

### 3.2.3 Fission cross section

In ENDF/B-VI [10] and JENDL-3.3 [13] evaluation fission cross section is assumed to be zero. We estimated fission cross section in the unresolved resonance energy region using for  $^{234}\text{Pa}$  transition state spectra those of  $^{232}\text{Pa}$  [9], fission barrier parameters were obtained fitting fission cross section data in the first plateau region [2, 3, 4] (see Fig. 8).

### 3.2.4 Capture cross section

We adopted here  $s$ -wave radiative strength function  $S_{\gamma 0} = 8.344 \times 10^{-2}$  ( $\Gamma_\gamma = 47$  meV and  $\langle D_{l=0} \rangle = 0.503$  eV). The important peculiarity of the calculated  $^{238}\text{U}(n, \gamma)$  capture cross section, Wigner cusp above first excited level threshold, is not pronounced in case of calculated  $^{233}\text{Pa}(n, \gamma)$  reaction cross section, because first level is at very low position -  $\sim 6$  keV (see Fig. 9). The pattern of  $s$ -,  $p$ - and  $d$ -wave channel contributions to the capture cross section in the energy range of 0.0165 - 70 keV is rather similar to that of  $^{238}\text{U}$  target nuclide of similar fission probability. In case of  $^{238}\text{U}(n, \gamma)$  reaction main contribution comes from  $p$ -wave neutrons above  $\sim 10$  keV. The  $p$ -wave contribution to the  $^{233}\text{Pa}(n, \gamma)$  reaction cross section is higher than that of  $s$ -wave above  $\sim 30$  keV, while that of  $d$ -wave neutrons is the lowest. Capture cross sections in present data file and those of JENDL-3.3 [13] are rather similar, while that of ENDF/B-VI [10] is much lower (see Fig. 9).

### 3.2.5 Inelastic scattering cross section

Calculated inelastic scattering cross section is very much different from previous evaluations of ENDF/B-VI [10] and JENDL-3.3 [13]. Conventional ENDF/B

processing codes (i.e. RECENT [21], NJOY [22]) exemplify Hauser-Feshbach-Moldauer formalism. Figure 10 shows partial contributions to the inelastic scattering coming from different  $(l, J)$ -channels. Major contribution, like in case of  $^{238}\text{U}+n$  interaction, comes from  $p$ -wave channels ( $l = 1, J = 0$ ), ( $l = 1, J = 1$ ), ( $l = 1, J = 2$ ) and ( $l = 1, J = 3$ ), the intermediate comes from  $s$ -wave channel ( $l = 0, J = 1$ ) and ( $l = 1, J = 2$ ), though only  $d$ -wave neutrons could excite  $2^+$  excited level of  $^{231}\text{Pa}$ . The lowest contribution comes from ( $l = 2, J = 0, 1, 2, 3, 4$ ) entrance channels, since both  $s$ -wave and  $d$ -wave neutrons contribute to exit channel. Evaluated inelastic scattering cross section of ENDF/B-VI [10] is much different from the present calculation.

### 3.2.6 Comparison of average resonance parameters

Figures 11-14 compare average neutron resonance spacings. Reduced neutron widths  $\langle \Gamma_n^{lJ} \rangle$  are compared on Figs. 15-19. Differences are pronounced either in  $s$ -wave and  $p$ -wave reduced neutron widths.

Table 3  
Average resonance parameters for  $^{233}\text{Pa}$

	$D_{l=0}, \text{eV}$	$\Gamma_\gamma, \text{meV}$	$S_0 \times 10^{-4}$	$S_1 \times 10^{-4}$	$R, \text{fm}$
JENDL-3.3	0.59	47	.75	1.50	10.092
ENDF/B-VI	0.097	55			
RIPL	$0.70 \pm 0.10(44)$	$47 \pm 2$	$0.75 \pm 0.08$		
Present	$0.503 \pm 0.095$	47	.8007	1.5136	9.486

The advantage of present evaluation is that it provides average energy dependent resonance parameters which reproduce evaluated cross sections, using conventional ENDF/B processing codes [21, 22] up to 70.9 keV.

## 4 Optical Potential

A coupled channel model is employed for estimating differential scattering and total cross sections. Another important application of coupled channel model is calculation of direct inelastic scattering contribution of discrete levels. The direct excitation of ground state rotational band levels  $3/2^-$ - $5/2^-$ - $7/2^-$  is estimated within rigid rotator model, three levels of ground state band are assumed coupled.

We adopted here the optical potential parameters obtained for  $^{232}\text{Th}$  [23] by fitting total cross section data, angular distributions and  $s$ -wave strength function. Then we fitted  $^{233}\text{Pa}$   $s$ -wave strength function  $S_0 = (0.80003) \times 10^{-4}$  with  $\beta_2$  and  $\beta_4$  deformation parameters. The optical potential parameters are as follows:

$$W_D = \begin{cases} V_R = 45.722 - 0.334E_n, \text{ MeV}, r_R = 1.2668 \text{ fm}, a_R = 0.6468 \text{ fm} \\ 3.145 + 0.455E_n, \text{ MeV}, & E_n \leq 8 \text{ MeV}, r_D = 1.25 \text{ fm}, a_D = 0.5246 \text{ fm} \\ 6.785 \text{ MeV}, & 8 < E_n < 20 \text{ MeV} \\ V_{SO} = 6.2 \text{ MeV}, r_{SO} = 1.120 \text{ fm}, a_{SO} = 0.47 \text{ fm}, \\ \beta_2 = 0.179, \beta_4 = 0.070 \end{cases} \quad (3)$$

## 4.1 Total and elastic cross sections

Present total cross section is compared with JENDL-3.3 [13] and ENDF/B-VI [10] evaluated cross section on Fig. 20. Present and JENDL-3.3 [13] estimates are not much different, while shape of ENDF/B-VI [10] cross section is rather discrepant with both evaluations up to  $\sim 20$  MeV. Figure 21 compares elastic cross sections estimates of present coupled channels optical potential and those of JENDL-3.3 [13] and ENDF/B-VI [10], estimated as a difference of the total and partial reaction cross sections.

## 5 Statistical Model

We calculated neutron cross sections within Hauser-Feshbach theory, coupled channel optical model and double-humped fission barrier model, as distinct from the previous evaluations of JENDL-3.3 [13] and ENDF/B-VI [10]

Hauser-Feshbach-Moldauer [24] statistical theory is employed for partial cross section calculations below emissive fission threshold. Fissioning and residual nuclei level densities as well as fission barrier parameters are key ingredients, involved in actinide neutron-induced cross section calculations. First, level density parameters are defined, using neutron resonance spacing  $\langle D_{l=0} \rangle$  estimate for  $^{233}\text{Pa}$  target nuclide. Constant temperature level density parameters  $T_o$ ,  $E_o$ ,  $U_c$  are defined by fitting cumulative number of low-lying levels of  $^{233}\text{Pa}$  and  $^{231}\text{Pa}$  (see Fig. 22) [15]. Fig. 23 shows the estimate of cumulative number of low-lying levels of  $^{234}\text{Pa}$ , obtained using systematic of constant temperature level density parameters  $T_o$ ,  $E_o$ ,  $U_c$  [15]. On this figure levels of the odd-odd  $^{238}\text{Np}$  nuclide are compared with similar model estimate.

In case of fast neutron ( $E_n \leq 6$  MeV) interaction with  $^{233}\text{Pa}$  target nucleus, the main reaction channel is inelastic neutron scattering, but fission cross section data description serves as a major constraint for the neutron inelastic scattering and radiative neutron capture cross section estimates. Below there is an outline of the statistical model [25, 26, 27] employed.

Neutron-induced reaction cross section ( $n, x$ ) for excitation energies up to emissive fission threshold is defined as

$$\sigma_{nx}(E_n) = \frac{\pi \lambda^2}{2(2I+1)} \sum_{ljJ\pi} (2J+1) T_{lj}^{J\pi}(E_n) P_x^{J\pi}(E_n) S_{nx}^{ljJ\pi}, \quad (3)$$

the compound nucleus decay probability  $P_x^{J\pi}$  ( $x = n, f, \gamma$ ) is

$$P_x^{J\pi}(E_n) = \frac{T_x^{J\pi}(U)}{T_f^{J\pi}(U) + T_n^{J\pi}(U) + T_\gamma^{J\pi}(U)}, \quad (4)$$

where  $U = B_n + E_n$  is the excitation energy of the compound nucleus,  $B_n$  is the neutron binding energy,  $T_{lj}^{J\pi}$  are the entrance neutron transmission coefficients for the channel  $(ljJ\pi)$ ,  $I$  is the target nucleus spin. Decay probability  $P_x^{J\pi}(E_n)$  of the compound nucleus with excitation energy  $U$  for given spin  $J$  and parity  $\pi$ , depends on  $T_f^{J\pi}$ ,  $T_n^{J\pi}(U)$  and  $T_\gamma^{J\pi}(U)$ , transmission coefficients of the fission, neutron scattering and radiative decay channels,  $S_{nx}^{ljJ\pi}$  denotes partial widths Porter-Thomas fluctuation factor. Below incident neutron energy equal to the cut-off energy of discrete level spectra, neutron cross sections are calculated within Hauser-Feshbach approach with correction for width fluctuation by Moldauer [24]. For width fluctuation correction calculation only Porter-Thomas fluctuations are taken into account. Effective number of degrees of freedom for fission channel is defined at the higher fission barrier saddle as  $\nu_f^{J\pi} = T_f^{J\pi}/T_{f\max}^{J\pi}$ , where  $T_{f\max}^{J\pi}$  is the maximum value of the fission transmission coefficient  $T_f^{J\pi}$ . At higher incident neutron energies the Tepel et al. [28] approach is employed, it describes cross section behavior in case of large number of open channels correctly.

## 5.1 Level Density

Level density is the main ingredient of statistical model calculations. Level density of fissioning, residual and compound nuclei define transmission coefficients of fission, neutron scattering and radiative decay channels, respectively. We will briefly discuss here level densities of odd-even  $^{233}\text{Pa}$  and odd-odd  $^{234}\text{Pa}$  nuclides.

The level densities were calculated with a phenomenological model by Ignatyuk et al. [17], which takes into account shell, pairing and collective effects in a consistent way

$$\rho(U, J, \pi) = K_{rot}(U, J)K_{vib}(U)\rho_{qp}(U, J, \pi), \quad (5)$$

where quasiparticle level density

$$\rho_{qp}(U, J, \pi) = \frac{(2J+1)\omega_{qp}(U)}{4\sqrt{2\pi}\sigma_\perp^2\sigma_\parallel} \exp\left(-\frac{J(J+1)}{2\sigma_\perp^2}\right), \quad (6)$$

$\omega_{qp}(U, J, \pi)$  is state density,  $K_{rot}(U, J)$  and  $K_{vib}(U)$  are factors of rotational and vibrational enhancement of the level density. The collective contribution of the level density of deformed nuclei is defined by the nuclear deformation order of symmetry. The actinide nuclei at equilibrium deformation are axially symmetric. The order of symmetry of nuclear shape at inner and outer saddles were adopted from calculations within shell correction method (SCM) by Howard & Möller [29],

protactinium nuclei of interest ( $A \leq 232$ ) are assumed to be axially symmetric, then

$$K_{rot}(U) = \sigma_{\perp}^2 = F_{\perp} t, \quad (7)$$

where  $\sigma_{\perp}^2$  is the spin cutoff parameter,  $F_{\perp}$  is the nuclear momentum of inertia (perpendicular to the symmetry axis), which equals the rigid-body value at high excitation energies, where the pairing correlations are destroyed, experimental value at zero temperature and is interpolated in between, using the pairing model,  $F_{\parallel} = 6/\pi^2 \langle m^2 \rangle (1 - 2/3\varepsilon)$ , where  $\langle m^2 \rangle$  is the average value of the squared projection of the angular momentum of the single-particle states, and  $\varepsilon$  is quadrupole deformation parameter. At outer saddle deformations mass asymmetry, which doubles the level density, is assumed. The closed-form expressions for thermodynamic temperature and other relevant equations which one needs to calculate  $\rho(U, J, \pi)$  are provided by Ignatyuk et al. model [17].

To calculate the residual nucleus level density at the low excitation energy, i.e. just above the last discrete level excitation energy where  $N^{exp}(U) \sim N^{theor}(U)$ , we employ a Gilbert-Cameron-type approach. The constant temperature approximation of

$$\rho(U) = dN(U)/dU = T^{-1} \exp((U - U_o)/T) \quad (8)$$

is extrapolated up to the matching point  $U_c$  to the  $\rho(U)$  value, calculated with a phenomenological model by Ignatyuk et al. [17] with the condition

$$U_c = U_o - T \ln(T \rho(U_c)). \quad (9)$$

In this approach  $U_o \simeq -n\Delta_o$ , where  $\Delta_o$  is the pairing correlation function,  $\Delta_o = 12/\sqrt{A}$ ,  $A$  is the mass number,  $n = 2$  for odd-odd, 1 for odd-even nuclei, i.e.  $U_o$  has the meaning of the odd-even energy shift. The value of nuclear temperature parameter  $T$  is obtained by the matching conditions at the excitation energy  $U_c$ .

In present approach the modelling of total level density

$$\rho(U) = K_{rot}(U) K_{vib}(U) \frac{\omega_{qp}(U)}{\sqrt{2\pi\sigma}} = T^{-1} \exp((U - U_o)/T) \quad (10)$$

in Gilbert-Cameron-type approach looks like a simple renormalization of quasiparticle state density  $\omega_{qp}(U)$  at excitation energies  $U < U_c$ . The cumulative number of observed levels for odd-even  $^{233}\text{Pa}$  and odd-odd nuclide  $^{238}\text{Np}$  [30, 31] are compared with constant temperature approximations for  $^{233}\text{Pa}$  and  $^{234}\text{Pa}$  on Figs. 22 and 23, respectively. In case of  $^{234}\text{Pa}$  missing of levels above  $\sim 0.35$  MeV is markedly pronounced. In case of  $^{234}\text{Pa}$  nuclide missing seems to start much earlier.

Few-quasiparticle effects which are due to pairing correlations are essential for state density calculation at low intrinsic excitation energies only for equilib-

rium  $^{233}\text{Pa}$  deformations. Few-quasiparticle effects in fissioning nuclide  $^{234}\text{Pa}$  are unimportant because of its odd-odd nature.

The partial  $n$ -quasiparticle state densities for odd  $^{233}\text{Pa}$ , which sum-up to intrinsic state density of quasiparticle excitations could be modelled using the Bose-gas model prescriptions [32, 33]. The intrinsic state density of quasiparticle excitations  $\omega_{qp}(U)$  could be represented as a sum of  $n$ -quasiparticle state densities  $\omega_{nqp}(U)$ :

$$\omega_{qp}(U) = \sum_n \omega_{nqp}(U) = \sum_n \frac{g^n (U - U_n)^{n-1}}{((n/2)!)^2 (n-1)!}, \quad (11)$$

where  $g = 6a_{cr}/\pi^2$  is a single-particle state density at the Fermi surface,  $n$  is the number of quasiparticles. The important model parameters are threshold values  $U_n$  for excitation of  $n$ -quasiparticle configurations  $n = 1, 3, \dots$  for odd-A nuclei [33]. The detailed treatment of this approach and approximations employed, as applied for fission, inelastic scattering or capture reaction calculations, is provided in [34, 35].

In case of and odd-odd nucleus  $^{234}\text{Pa}$  Gilbert-Cameron-type approximation of  $\rho(U)$  is employed. Nuclear level density  $\rho(U)$  of odd nuclide  $^{233}\text{Pa}$  at equilibrium deformation, as compared with the Gilbert-Cameron-type approximation of  $\rho(U)$  is shown on Fig. 24. The arrows on the horizontal axis of Fig. 24 indicate the excitation thresholds of odd  $n$ -quasiparticle configurations.

Main parameters of the level density model for equilibrium, inner and outer saddle deformations are as follows: shell correction  $\delta W$ , pairing correlation functions  $\Delta$  and  $\Delta_f$ , at equilibrium deformations  $\Delta = 12/\sqrt{A}$ , quadrupole deformation  $\varepsilon$  and momentum of inertia at zero temperature  $F_0/\hbar^2$  are given in Table 4. For ground state deformations the shell corrections were calculated as  $\delta W = M^{exp} - M^{MS}$ , where  $M^{MS}$  denotes liquid drop mass (LDM), calculated with Myers-Swiatecki parameters [36], and  $M^{exp}$  is the experimental nuclear mass. Shell correction values at inner and outer saddle deformations  $\delta W_f^{A(B)}$  are adopted following the comprehensive review by Bjornholm and Lynn [37].

Table 4

Level density parameters of fissioning nucleus and residual nucleus

Parameter	inner saddle	outer saddle	neutron channel
$\delta W$ , MeV	1.5	0.6	LDM
$\Delta$ , MeV	$\Delta_o + \delta^*$	$\Delta_o + \delta^*$	$\Delta_o$
$\varepsilon$	0.6	0.8	0.24
$F_0/\hbar^2$ , $\text{MeV}^{-1}$	100	200	73



\*)  $\delta = \Delta_f - \Delta$  value is defined by fitting fission cross section in the plateau region.

## 5.2 Fission Cross Section

Fission data fit is used as a major constraint for capture, elastic and inelastic scattering, (n,2n) and (n,3n) cross sections as well as secondary neutron spectrum estimation. Description of measured fission cross section might justify a validity of level density description and fission barrier parameterization.

## 5.3 Fission Channel

Fission barrier of Pa is three-humped [29], that is, the outer barrier has one more shallow well. However, inner barrier height is rather low as compared with the outermost one [29]. That means in the first "plateau" region and at higher energies we can use double-humped barrier model and relevant barrier parameters. Even at lower energies we could describe the general shape of the fission cross section starting from  $\sim 0.01$  keV.

Neutron-induced fission in a double humped fission barrier model could be viewed as a two-step process, i.e. a successive crossing over the inner hump  $A$  and over the outer hump  $B$ . Hence, the transmission coefficient of the fission channel  $T_f^{J\pi}(U)$  can be represented as

$$T_f^{J\pi}(U) = \frac{T_{fA}^{J\pi}(U)T_{fB}^{J\pi}(U)}{(T_{fA}^{J\pi}(U) + T_{fB}^{J\pi}(U))}. \quad (12)$$

The transmission coefficient  $T_{fi}^{J\pi}(U)$  is defined by the level density  $\rho_{fi}(\epsilon, J, \pi)$  of the fissioning nucleus at the inner and outer humps ( $i = A, B$ , respectively):

$$T_{fi}^{J\pi}(U) = \sum_{K=-J}^J T_{fi}^{JK\pi}(U) + \int_0^U \frac{\rho_{fi}(\epsilon, J, \pi)d\epsilon}{(1 + \exp(2\pi(E_{fi} + \epsilon - U)/h\omega_i))}, \quad (13)$$

where the first term denotes the contribution of low-lying collective states and the second term that from the continuum levels at the saddle deformations,  $\epsilon$  is the intrinsic excitation energy of fissioning nucleus. The first term contribution due to discrete transition states depends upon saddle symmetry. The total level density  $\rho_{fi}(\epsilon, J, \pi)$  of the fissioning nucleus is determined by the order of symmetry of nuclear saddle deformation.

Inner and outer fission barrier heights and curvatures as well as level densities at both saddles are the model parameters. They are defined by fitting fission cross section data at incident neutron energies below emissive fission threshold. Fission barrier height values and saddle order of symmetry are strongly interdependent.

The order of symmetry of nuclear shape at saddles was defined by Howard and Möller [29] within shell correction method (SCM) calculation. We adopt the saddle point asymmetries from SCM calculations. According to shell correction method (SCM) calculations of Howard and Möller [29] the inner and outer barriers were assumed axially symmetric. Outer barrier for the protactinium nuclei is assumed mass-asymmetric.

### 5.3.1 Fission transmission coefficient, level density and transition state spectrum

Adopted level density description allows to describe shape of measured fission cross section data of  $^{233}\text{Pa}$  (see Figs. 8, 25 and 26). One- and two-quasiparticle states in odd residual nuclide  $^{231}\text{Pa}$  could be excited. The transition state spectra of odd-odd  $^{232}\text{Pa}$  nuclide for the band-heads of Table 5 were constructed using values of  $F_0/\hbar^2$  at the inner and outer saddles shown in Table 4.

We construct the discrete transition spectra up to  $\sim 130$  keV, using collective states of Table 5. The discrete transition spectra, as well as continuous level contribution to the fission transmission coefficient are dependent upon the order of symmetry for fissioning nucleus at inner and outer saddles. With transition state spectra thus defined the fission barrier parameters are obtained.

Table 5.  
Transition spectra band-heads, Z-even, N-odd nuclei

inner saddle		outer saddle	
$K^\pi$	$E_{K^\pi}$ , MeV	$K^\pi$	$E_{K^\pi}$ , MeV
$6^-$	0.0	$6^-$	0.0
$1^-$	0.22	$1^-$	0.22
$0^-$	0.05	$0^-$	0.05
$1^+$	0.01	$1^+$	0.01
$2^+$	0.01	$0^+$	0.01
$0^+$	0.01	$3^+$	0.01
$3^+$	0.01	$2^+$	0.01
$0^+$		$1^-$	0.21
$0^+$		$6^+$	0.24
$0^+$		$6^-$	0.24

## 5.4 Fission Data Analysis

Fission cross section of  $^{233}\text{Pa}(\text{n},\text{f})$  was measured by Tovesson et al. [2] between 1 and 3 MeV and then by Hambsch et al. [3] between 5 and 8.5 MeV, relative to that of  $^{235}\text{U}(\text{n},\text{f})$ . Evaluation of JENDL-3.3 is compatible with this measurement only between 3 and 5 MeV (see Fig. 25).

$^{233}\text{Pa}(\text{n},\text{f})$  fission data [4], extracted from the transfer reaction  $^{232}\text{Th}(^3\text{He},\text{p})^{234}\text{Pa}$  for the neutron energy range of 0.5 - 10 MeV are somewhat higher than the direct neutron-induced fission data by data Tovesson et al. [2] and Hambsch et al. [3].

We fit the decreasing trend of data above  $E_n \sim 3$  MeV increasing the correlation function value at outer saddle, which controls the cross section shape. For incident neutron energies up to  $E_n \sim 2.5$  MeV the threshold shape is roughly reproduced by varying the density of one-quasiparticle states of residual nuclide  $^{233}\text{Pa}$ , as described in [35] (see Fig. 25).

## 5.5 Inelastic Scattering

Fission data fit defines the compound inelastic neutron scattering contribution to the total inelastic scattering cross section. The relative contribution of direct discrete level excitation cross sections is about the same as in case of  $^{238}\text{U}$  target nuclide because of similar fission competition to compound neutron scattering.

## 5.6 Neutron Channel

The lumped transmission coefficient of the neutron scattering channel (see Eqs. (4), (5)) is given by

$$T_n^{J\pi}(U) = \sum_{l'j'q} T_{l'j'}^{J\pi}(E_n - E_q) + \sum_{l'j'I'} \int_0^{U-U_c} T_{l'j'}^{J\pi}(E'_n) \rho(U - E'_n, I', \pi) dE'_n, \quad (14)$$

where  $\rho(U - E'_n, I', \pi)$  is the level density of the residual nucleus. Levels of residual nuclide  $^{233}\text{Pa}$  [38] are provided in Table 6. The entrance channel neutron transmission coefficients  $T_{lj}^{J\pi}$  are calculated within a rigid rotator coupled channel approach. For the compound nucleus formation cross section calculation, the cross sections of the direct excitation of ground state band levels were subtracted from the absorption cross section. The compound and direct inelastic scattering components are added incoherently.

The exit neutron transmission coefficients  $T_{l'j'}^{J\pi}(E'_n)$  were calculated using the re-normalized deformed optical potential of entrance channel without coupling, which describes a neutron absorption cross section.

## 5.7 Ground State Rotational Band

Predicted discrete level excitation cross section shape, calculated within a rigid rotator model, depends upon optical potential used. We assume strong missing of levels above excitations of  $\sim 0.367$  MeV (see Fig. 22), so only 19 levels up to this excitation energy were included when calculating inelastic scattering cross sections. Predicted discrete level excitation cross section shape, calculated within

a rigid rotator model, depends upon optical potential used. Calculated compound contribution is controlled mainly by fission competition (see Figs. 27-44). Figures 29 and 42 show that direct scattering essentially defines the excitation cross section of  $J^\pi = 5/2^-$  and  $7/2^-$  levels of ground state band levels at  $E_n \gtrsim 2$  MeV. Discrepancies with previous evaluation of JENDL-3.3 [13] are due to both compound and direct contributions differences. The compound component tends to be zero above  $\sim 3$  MeV incident neutron energy.

Table 6  
Levels of  $^{233}\text{Pa}$

	$E_q$ , keV	$J^\pi$	$K^\pi$
1	0.0	$3/2^-$	$3/2^-$
2	0.0067	$1/2^-$	$1/2^-$
3	0.0572	$7/2^-$	$7/2^-$
4	0.0706	$5/2^-$	$3/2^-$
5	0.0865	$5/2^+$	
6	0.0947	$3/2^+$	
7	0.1036	$7/2^+$	
8	0.109	$9/2^+$	
9	0.1634	$11/2^+$	
10	0.1691	$1/2^+$	
11	0.1792	$9/2^-$	
12	0.2017	$3/2^+$	
13	0.2123	$5/2^+$	
14	0.2379	$9/2^+$	
15	0.2573	$5/2^-$	
16	0.2796	$7/2^+$	
17	0.3004	$7/2^-$	$3/2^-$
18	0.3061	$7/2^+$	
19	0.3661	$9/2^+$	

## 5.8 Total inelastic cross section

Calculated total inelastic cross section is compared with previous evaluated data on Figs. 45 and 46. Lumped contribution of direct excitation of ground state band levels is shown to attain only  $\sim 10\%$  of the total inelastic cross section at  $E_n \gtrsim 2$  MeV. The calculated curve is consistent with the JENDL-3.3 evaluation [13] up to  $E_n \sim 1$  MeV, while at higher energies the discrepancy might be attributed to differences in the models. Our estimate is incompatible with ENDF/B-VI [10] evaluation (see Figs. 45, 46).

Shape of calculated continuum inelastic scattering cross section is rather similar to that of JENDL-3.3 [13] evaluated total inelastic scattering cross section

(see Fig. 47), but the absolute values at  $E_n \lesssim 7$  MeV are rather discrepant. Continuum inelastic scattering cross section of ENDF/B-VI [10] evaluation seems to be too high.

Above emissive fission threshold evaluations of inelastic scattering cross section differ severely, present estimate being the highest (see Fig. 46). In our calculations pre-equilibrium neutron emission contribution is defined by description of  $^{238}\text{U}$  secondary neutron spectra and consistent description of  $^{238}\text{U}(\text{n},\text{f})$ ,  $^{238}\text{U}(\text{n},2\text{n})$  and  $^{238}\text{U}(\text{n},3\text{n})$  reaction cross sections [34]. Pre-equilibrium neutron emission contribution is essential to reproduce the observed fission cross section of  $^{231}\text{Pa}(\text{n},\text{f})$  up to  $E_n \sim 10$  MeV.

## 6 Capture cross section

We have demonstrated by the analysis of measured capture cross sections of  $^{238}\text{U}(\text{n},\gamma)$  and  $^{232}\text{Th}(\text{n},\gamma)$  [39] that neutron capture data could be described within a Hauser-Feshbach-Moldauer statistical model. Specifically, in a few-keV energy region calculated capture cross section is defined by the radiative strength function value  $S_\gamma = \Gamma_\gamma/D$ . At incident neutron energies above  $\sim 100$  keV calculated capture cross section shape is defined by the energy dependence of radiative strength function  $S_\gamma$ . Energy dependence of  $S_\gamma$  is controlled mainly by the energy dependence of the level density of the compound nuclide  $^{234}\text{Pa}$ . Rather high fission threshold for the  $^{234}\text{Pa}$  nuclide defines weak competition of fission [19] alongside with neutron emission [18] at the second  $\gamma$ -cascade, i.e. after first  $\gamma$ -quanta emission. Then "true" capture reaction cross section  $(\text{n},\gamma\gamma)$  is defined using transmission coefficient  $T_{\gamma\gamma}^{J\pi}(U)$ , which is defined in a two-cascade approximation as

$$T_{\gamma\gamma}^{J\pi} = \frac{2\pi C_{\gamma 1}}{3(\pi\hbar c)^2} \int \varepsilon_\gamma^2 \sigma_\gamma(\varepsilon_\gamma) \sum_{I=|J-1|}^{I=J+1} \rho(U - \varepsilon_\gamma, I, \pi) \frac{T_\gamma^{I\pi}}{T_f^{I\pi} + T_{n'}^{I\pi} + T_\gamma^{I\pi}} d\varepsilon_\gamma, \quad (15)$$

The last term of the integrand describes the competition of fission, neutron emission and  $\gamma$ -emission at excitation energy  $(U - \varepsilon_\gamma)$  after emission of first  $\gamma$ -quanta,  $C_{\gamma 1}$  is the normalizing coefficient. That means that transmission coefficients  $T_\gamma^{I\pi}$ ,  $T_{n'}^{I\pi}$  and  $T_f^{I\pi}$  are defined at excitation energy  $(U - \varepsilon_\gamma)$ . The neutron emission after emission of first  $\gamma$ -quanta strongly depends on the  $^{233}\text{Pa}$  residual nuclide level density at excitations around  $U_3$ . The contribution of  $(\text{n},\gamma\text{f})$ -reaction [19] to fission cross section is defined by  $T_{\gamma f}^{J\pi}$  value. The energy dependence of  $(\text{n},\gamma\text{f})$  reaction transmission coefficient  $T_{\gamma f}^{J\pi}$  was calculated with the expression

$$T_{\gamma f}^{J\pi} = \frac{2\pi C_{\gamma 1}}{3(\pi\hbar c)^2} \int \varepsilon_\gamma^2 \sigma_\gamma(\varepsilon_\gamma) \sum_{I=|J-1|}^{I=J+1} \rho(U - \varepsilon_\gamma, I, \pi) \frac{T_f^{I\pi}}{T_f^{I\pi} + T_{n'}^{I\pi} + T_\gamma^{I\pi}} d\varepsilon_\gamma, \quad (16)$$

The capture cross section is shown on Fig. 48. The  $(n,\gamma f)$  reaction competition to the "true" capture  $(n,\gamma\gamma)$  reaction competition is very weak. The competition of  $(n,\gamma n')$  reaction to the "true" capture  $(n,\gamma\gamma)$  reaction is essential above  $E_n \sim 1$  MeV. We adopted here radiative capture strength function  $S_{\gamma o}$ , which actually corresponds to  $\langle \Gamma_\gamma \rangle = 47$  meV and  $\langle D_{l=0} \rangle = 0.503$  eV. Above  $E_n \sim 1$  MeV capture cross section decrease is defined by  $(n,\gamma n')$  reactions competition.

Previous evaluated capture cross sections are drastically discrepant with present calculation at  $E_n \gtrsim 10$  keV (see Fig. 48). For higher incident neutron energies competition of fission and inelastic scattering with  $\gamma$ -emission seems to be modelled correctly within present approach. A consistent description of a most complete set of measured data on the  $(n,\gamma)$ ,  $(n,f)$  and  $(n,n')$  reaction cross sections for the  $^{238}\text{U}$  and  $^{232}\text{Th}$  target nuclides [5, 6, 7, 39] enables one to consider the statistical theory estimates of  $^{233}\text{Pa}(n,\gamma)$  reaction as fairly realistic.

## 7 Cross sections above emissive fission threshold

At incident neutron energies when fission of  $^{233}\text{Pa}$  or  $^{232}\text{Pa}$  nuclides is possible after emission of 1 or 2 pre-fission neutrons, the observed  $^{233}\text{Pa}(n,f)$  fission cross section being a superposition of non-emissive or first chance fission of  $^{234}\text{Pa}$  and  $x$ th-chance fission contributions. These contributions are weighted with a probability of  $x$  neutron emission before fission. Above emissive fission threshold the fission probabilities of  $^{233}\text{Pa}$  and  $^{232}\text{Pa}$  nuclides, fissioning in  $^{233}\text{Pa}(n,nf)$  and  $^{233}\text{Pa}(n,2nf)$  reactions, respectively, could be estimated using data of transfer reactions  $^{232}\text{Th}(^3\text{He},d)^{233}\text{Pa}$  and  $^{231}\text{Pa}(d,p)^{232}\text{Pa}$  [40]. A consistent description of a most complete set of measured data on the  $(n,f)$ ,  $(n,2n)$ ,  $(n,3n)$  and  $(n,4n)$  reaction cross sections for the  $^{238}\text{U}$  target nuclide up to 20 MeV enables one to consider the estimates of first neutron spectra of composite  $^{234}\text{Pa}$  nuclide as fairly realistic.

### 7.1 Fission cross section

Above emissive fission threshold contributions of emissive fission to the observed fission cross section coming from  $(n,xnf)$ ,  $x = 1, 2, 3 \dots X$ , fission reactions of relevant equilibrated uranium nuclei, could be calculated as

$$\sigma_{nF}(E_n) = \sigma_{nf}(E_n) + \sum_{x=1}^X \sigma_{n,xnf}(E_n), \quad (17)$$

emissive fission contributions could be calculated using fission probability estimates  $P_{fi}^{J\pi}(U)$  as

$$\sigma_{n,xf}(E_n) = \sum_{J\pi} \int_0^{U_{max}} W_{x+1}^{J\pi}(U) P_{f(x+1)}^{J\pi}(U) dU, \quad (18)$$

where  $W_x^{J\pi}(U)$  is the population of  $(x+1)$ -th nucleus at excitation energy  $U$  after emission of  $x$  neutrons, excitation energy  $U_{max}$  is defined by the incident neutron energy  $E_n$  and energy, removed from the composite system by  $^{233}\text{Pa}(n,xf)$  reaction neutrons. Fission probabilities  $P_{fx}^{J\pi}$  for fissioning nuclei  $^{233}\text{Pa}$  and  $^{232}\text{Pa}$  could be estimated using transfer reactions  $^{232}\text{Th}(^3\text{He},d)^{233}\text{Pa}$  and  $^{231}\text{Pa}(d,p)^{232}\text{Pa}$  [40].

Contribution of first-chance fission is defined by the pre-equilibrium emission of first neutron and level densities of fissioning  $^{234}\text{Pa}$  and residual  $^{233}\text{Pa}$  nuclides. The behavior of the first-chance fission cross section  $\sigma_{nf}$  is obviously related to the energy dependence of the fission probability of the  $^{234}\text{Pa}$  nuclide  $P_{f1}$  [41]:

$$\sigma_{nf} = \sigma_r(1 - q(E_n))P_{nf}. \quad (19)$$

Once the contribution of first neutron pre-equilibrium emission  $q(E_n)$  is fixed [5], the first-chance fission probability  $P_{nf}$  of the  $^{234}\text{Pa}$  composite nuclide depends only on the level density parameters of fissioning and residual nuclei. Actually, it depends on the ratio of shell correction values  $\delta W_{fA(B)}$  and  $\delta W_n$ . The results of different theoretical calculations of the shell corrections as well as of the fission barriers vary by 1 ~ 2 MeV. The same is true for the experimental shell corrections, which are obtained with a smooth component of potential energy calculated according to the liquid-drop or droplet model. However the isotopic changes of  $\delta W_{fA(B)}$  and  $\delta W_n$  [37] are such that  $P_{nf}$  viewed as a function of the difference  $(\delta W_{fA(B)} - \delta W_n)$  is virtually independent on the choice of smooth component of potential energy. Therefore, we shall consider the adopted  $\delta W_{fA(B)}$  estimates (see Table 4) to be effective, provided that  $\delta W_n$  are obtained with the liquid drop model. Fission barrier of Pa is three-humped [29], that is, the outer barrier has one more shallow well. However, the inner barrier height is rather low as compared with the outermost one [29]. So, in the first "plateau" region and at higher energies we can safely use double-humped barrier model and relevant barrier parameters (see Table. 7).

Neutron-induced fission cross section of  $^{233}\text{Pa}$ , shown on the Fig. 49 demonstrates strong step-like structures, relevant to the contributions of  $(n,xf)$  reactions to the observed  $^{233}\text{Pa}(n,f)$  fission cross section. Figure 50 shows relative contributions of emissive fission chances to the observed fission cross sections of  $^{233}\text{Pa}(n,f)$ . The contributions of first-chance fission to the  $^{233}\text{Pa}(n,f)$  and  $^{238}\text{U}(n,f)$  reaction cross sections are similar functions of incident neutron energy. In both cases a local minimum is observed near  $(n,nf)$  reaction threshold. The second-chance fission contribution  $^{233}\text{Pa}(n,nf)$  is a smooth increasing function of excitation energy up to  $E_n \sim 7$  MeV, it is much higher than in case of  $^{238}\text{U}(n,f)$  reaction. The contribution of  $^{233}\text{Pa}(n,2nf)$  reaction to the total fission cross section is also

generally higher than in case of  $^{238}\text{U}(\text{n},2\text{n}\text{f})$  reaction. Figure 51 compares calculated fission cross sections of  $^{232}\text{Pa}(\text{n},\text{f})$  with simulated fission cross section data obtained by Britt and Wilhelmy [40] as  $\sigma_f = 3.1 \times P_f$ . The discrepancies of calculated curved and simulated data below 2 MeV are explained by the entrance channel influence in transfer reactions and neutron-induced fission reaction. Figure 52 compares  $^{231}\text{Pa}(\text{n},\text{f})$  calculated and measured neutron-induced fission data.

Above (n,nf) reaction threshold (see Fig. 49) calculated curve is fitted to indirect data by Petit et al. [4] up to 10 MeV. Data points by Hambsch [3] in  $E_n \sim 5 - 8$  MeV energy range seem to be too low. Actually, the fission cross section shape, predicted by measured data by Hambsch [3], could be fitted, but for that the contribution of second chance fission cross section  $^{233}\text{Pa}(\text{n},\text{nf})$  should be very low, so that calculated  $^{232}\text{Pa}(\text{n},\text{f})$  cross section would be drastically discrepant with indirect data by Britt and Wilhelmy [40] on  $^{232}\text{Pa}(\text{n},\text{f})$  at  $E_n \sim 0.5 - 5$  MeV (see Fig. 51). In case we choose to fit data by Britt and Wilhelmy [40] on  $^{232}\text{Pa}(\text{n},\text{f})$  at  $E_n \sim 1 - 5$  MeV, the strong decrease of  $^{233}\text{Pa}(\text{n},\text{f})$  cross section above  $E_n \sim 7$  MeV would not be reproduced, calculated  $^{233}\text{Pa}(\text{n},\text{f})$  cross section would remain rather flat in the second plateau region. This change of shape of  $^{233}\text{Pa}(\text{n},\text{f})$  cross section as well as fit of data by Britt and Wilhelmy [40] on  $^{232}\text{Pa}(\text{n},\text{f})$  at  $E_n \sim 1 - 5$  MeV is obtained by decreasing the  $\delta = \Delta_f - \Delta$  parameter value, which is usually defined by fitting fission cross section in the plateau region, from 0.165 MeV to 0.07 MeV, the latter value corresponds to the  $\delta$ -parameter value for  $^{231}\text{Pa}$  fissioning nuclide. It is obvious, that the data by Petit et al. [4] on  $^{231}\text{Pa}(\text{n},\text{f})$  cross section were derived with rather approximate procedure, however, we will keep for the time being as an evaluated cross section a curve, fitting these data above emissive fission threshold. We assume, nonetheless, that the  $^{231}\text{Pa}(\text{n},\text{f})$  calculated cross section, obtained by fitting  $^{232}\text{Pa}(\text{n},\text{f})$  data by Britt and Wilhelmy [40] in  $E_n \sim 1 - 5$  MeV energy range, looks more reasonable.

Table 7  
Fission barrier parameters of Pa nuclei

Nuclide	$E_A$	$E_B$	$\hbar\omega_A$	$\hbar\omega_B$	$\delta$
$^{234}\text{Pa}$	5	6.4	.6	.42	.21
$^{233}\text{Pa}$	5	5.9	1	.5	.165
$^{232}\text{Pa}$	5	6.2	.6	.42	.20
$^{231}\text{Pa}$	5.25	5.45	1.	.5	.075
$^{230}\text{Pa}$	5.0	5.5	.6	.4	.25
$^{229}\text{Pa}$	4.8	6.0	.7	.5	.075

## 7.2 $^{233}\text{Pa}(\text{n},\text{xn})$ cross section

There is no measurements of  $^{233}\text{Pa}(\text{n},2\text{n})$  or  $^{233}\text{Pa}(\text{n},3\text{n})$  reaction cross section. These cross sections would be estimated using  $^{233}\text{Pa}(\text{n},\text{f})$  fission cross section fit



up to  $E_n = 20$  MeV as the only constraint. Present estimate of  $^{233}\text{Pa}(n,2n)$  cross section for  $E_n \lesssim 10$  MeV is about twice lower than that of JENDL-3.3 [13], the estimate of ENDF/B-VI shows unrealistic structures around  $E_n \sim 10$  MeV (Fig. 58). For  $E_n \gtrsim 10$  MeV calculated  $(n,2n)$  reaction cross section shape corresponds to pre-equilibrium emission contribution to the first neutron spectrum.

Present estimate of  $^{233}\text{Pa}(n,3n)^{232}\text{U}$  cross section is much lower than those of JENDL-3.3 [13] and ENDF/B-VI [10], both seem to be unrealistically high (see Fig. 59).

## 8 Neutron emission spectra

Neutron emission spectra are inclusive of both fission and scattered neutrons. First we will describe the approach used for the prompt fission neutron number  $\nu_p$  and prompt fission neutron spectra (PFNS) calculation and then return to the discussion on neutron emission spectra. A brief survey of the model used to estimate prompt fission neutron number  $\nu_p$  value and PFNS is provided below.

### 8.1 Prompt fission neutron number $\nu_p$

There are no experimental data for prompt fission neutron spectra and prompt neutron multiplicity  $\nu_p$  for  $^{233}\text{Pa}$ . The evaluated data for JENDL-3.3 and ENDF/B-6 files are based on the systematics [42] that uses simple linear extrapolation in the incident neutron energy range up to 20 MeV (see Fig. 55). We applied more complicated approach with incorporation of the pre-fission neutron emission and fission chances. The incident neutron energy dependence of neutron multiplicity in the energy range  $E_n \lesssim 6$  MeV for all fissioning nuclei was taken from evaluation by Malinovskij [43]. At incident neutron energies above emissive fission threshold the number of prompt fission neutron  $\nu_p(E_n)$  was calculated as

$$\begin{aligned} \nu_p(E_n) = & \beta_o \nu_o(E_n) + \beta_1(1 + \nu_1(E_n - B_{nA} - \langle E_1 \rangle)) + \\ & \beta_2(2 + \nu_2(E_n - B_{nA} - B_{nA-1} - \langle E_1 \rangle - \langle E_2 \rangle)). \end{aligned} \quad (20)$$

Here,  $\nu_i(E_n)$  is a prompt fission neutron number for  $i$ -th fissioning nucleus,  $B_{nA}$  - neutron binding energy for the  $A$  nucleus,  $\langle E_i \rangle$  - average energy of  $i$ -th pre-fission neutron. To calculate the  $\nu_p$  for  $^{233}\text{Pa}(n,f)$  reaction up to  $E_n = 20$  MeV we need to estimate  $\nu_p$  values for  $^{232}\text{Pa}$  and  $^{231}\text{Pa}$  target nuclides, which contribute to the observed  $\nu_p$ -value of neutron-induced fission of  $^{233}\text{Pa}$  target nuclide via  $(n,xnf)$  emissive fission processes. Relevant partial contributions are shown on Fig. 56. We assumed that excitation energy

$$U_i = E_n - \sum_j (B_{nj} + \langle E_{ij} \rangle), \quad (21)$$

is brought into  $A_i$  nucleus with the reaction:  $n + (A_i - 1) \rightarrow fission$ . Incident neutron energy in this hypothetical reaction equals to  $U_i - B_{nA_i}$ . In this way the  $\nu_i(E_n)$  functions for all nuclides in the mass chain  $A+1, A, A-1$  were calculated.

Energy dependence of  $\nu_p$  versus incident neutron energy estimated with this equation is compared on Fig. 55 with previous evaluations. Bump in  $\nu_p$  above (n,nf) reaction threshold is due to the pre-fission neutrons, emitted in  $^{233}\text{Pa}(\text{n,nf})$  reaction. The similar behavior was evidenced in measured data for  $^{232}\text{Th}(\text{n,f})$  and  $^{238}\text{U}(\text{n,f})$ , it was reproduced with the present model. The delayed neutrons yield and decay parameters were taken to be the same as in JENDL-3.3 [13], i.e. from [44].

Table 8

The evaluated first chance  $\nu$ -values for  $^{229,230,231}\text{Pa}$  target nuclides.

Target	$\nu^{th}$	$\nu(3 \text{ MeV})$	$\nu(6 \text{ MeV})$
$^{231}\text{Pa}$	2.298	2.561	2.821
$^{232}\text{Pa}$	2.418	2.681	2.941
$^{233}\text{Pa}$	2.442	2.708	2.970

## 8.2 Prompt fission neutron spectra

Prompt Fission Neutron Spectra (PFNS) for  $^{231}\text{Pa}$  have been calculated with the model that was previously applied for  $^{238}\text{U}$  and  $^{232}\text{Th}$  PFNS data analysis [45, 46]. Here is enclosed a brief description of the PFNS model.

### 8.2.1 Model for PFNS evaluation

For the first chance fission reaction the PFNS are calculated as a sum of two Watt distributions [47]:

$$S_i(E, E_n) = 0.5 \cdot \sum_{j=1,2} W_i(E, E_n, T_{ij}(E_n), \alpha) \quad (22)$$

where

$$T_{ij} = k_{ij} \cdot \sqrt{E^*} = \sqrt{E_r + E_n + B_n - TKE} \quad (23)$$

is the temperature parameters of light and heavy fragments ( $j=1,2$ ) for nucleus " $i$ ", is the ratio of the total kinetic energy ( $TKE$ ) at the moment of the neutron emission to the  $TKE$  value at full acceleration limit. Ratio  $\alpha$  was used as a free parameter to fit PFNS experimental data for a number of actinide nuclei, its values for various nuclei scatter only slightly. The ratio of the "temperatures" for light and heavy fragment was the second semi-empirical fitting parameter, it also varies from one target nucleus to another only slightly, we assumed  $r=1.248$  for all actinide nuclei.

Above emissive fission threshold PFNS are described by the equation

$$\begin{aligned}
S(E, E_n) &= \nu^{-1}(E_n)(\nu_o(E_n) \cdot \beta_o(E_n) \cdot S_o(E, E_n) + \\
&\quad \nu_1(E_n) \cdot \beta_1(E_n) \cdot S_1(E, E_n) + \beta_1(E_n) \cdot P_{11}(E, E_n) + \\
&\quad \nu_2(E_n) \cdot \beta_2(E_n) \cdot S_2(E, E_n) + \\
&\quad \beta_2(E_n) \cdot [P_{21}(E, E_n) + P_{22}(E, E_n)] + \dots), \\
\int P_{ik}(E, E_n) dE &= 1, \\
\nu(E_n) &= \sum_{i=0} [(\nu_i(E_n) + i) \cdot \beta_i(E_n)], \tag{24}
\end{aligned}$$

where subscript  $i$  denotes  $i$ -th chance fission reaction of the  $A + 1$ ,  $A$ ,  $A - 1$  nuclei after emission of  $i$  pre-fission neutrons,  $\beta_i(E_n)$  is the  $i$ -th chance fission contribution to the observed fission cross section (see Figs. 49 and 50),  $\nu_i(E_n)$  is the number of the prompt fission neutron for relevant nucleus,  $S_i(E, E_n)$  is the PFNS spectrum without pre-fission neutrons,  $P_{ik}(E, E_n)$  is the spectrum of  $k$ -th pre-fission neutron for  $i$ -th chance fission. To estimate observed PFNS,  $\nu_i(E_n)$ ,  $\beta_i(E_n)$  and  $T_{ij}$  values should be calculated.

The pre-fission neutron spectra  $P_{ik}(E, E_n)$  were calculated as described in [46]. The pre-equilibrium pre-fission neutron emission was also taken into account.

The excitation energy  $U_i$  of the nucleus  $A_i = A + 1 - i$  after emission of  $i$  neutrons was calculated as:

$$U_i = B_n + E_n - \sum_j (B_j + \langle E_{ij} \rangle), \tag{25}$$

where  $B_j$  is the neutron binding energy. This allows to estimate the excitation energy of fission fragments as  $E^* = E_r + U - TKE$  and calculate the  $T_{ij}(E_n)$  energy for each nucleus in the mass chain. The equation for the  $\nu_i(E_n)$  calculation is given in previous section.

For  $E_n \gtrsim 10$  MeV we incorporated an additional correction, used previously to remove a discrepancy between measured and calculated data for PFNS of  $^{238}\text{U}(\text{n,f})$  and  $^{232}\text{Th}(\text{n,f})$  reactions [45]. We assume that the same correction for CMS energy per nucleon  $E_{v0}$  should be introduced for  $^{233}\text{Pa}(\text{n,f})$  reaction. The CMS energy was calculated as

$$E_v = \alpha \cdot \alpha_1 \cdot E_{v0}, \tag{26}$$

$\alpha_1=1$  for  $E_n \leq 10$  MeV and  $\alpha_1=0.8$  for  $E_n > 12$  MeV and linearly interpolated for  $10 < E_n < 12$  MeV. This correction was made either for non-emissive and emissive fission reactions.

### 8.2.2 Pre-fission (n,xnf) neutron spectra

Partial neutron energy distributions  $P_{ik}(E, E_n)$  of (n,xnf),  $x = 1, 2, 3$ , reactions are calculated with Hauser-Feshbach model taking into account fission and gamma-emission competition to neutron emission, actually neutron spectra are calculated simultaneously with fission and (n,xn) reaction cross sections [46]. The pre-equilibrium emission of first neutron is fixed by the description of high energy tails of (n,2n) reaction cross sections and (n,f) reaction cross sections for  $^{238}\text{U}$  and  $^{232}\text{Th}$  target nuclides. First neutron spectrum of the  $^{233}\text{Pa}(\text{n},\text{nf})$  reaction is the sum of evaporated and pre-equilibrium emitted neutron contributions. Second and third neutron spectra for  $^{233}\text{Pa}(\text{n},\text{xnf})$  fission reactions are assumed to be evaporative. Pre-fission neutron spectrum of  $^{233}\text{Pa}(\text{n},\text{nf})$  reaction, especially its hard energy tail, is sensitive to the description of fission probability of  $^{233}\text{Pa}$  nuclide near fission threshold (see below).

Partial neutron spectra are shown on Figs. 57-63. Components of first, second, third and fourth neutron spectra for  $E_n = 20$  MeV are shown on Figs. 57, 58, 59 and 60. Components of first, second and neutron spectra for  $E_n = 14$  MeV are shown on Figs. 61, 62 and 63, for  $E_n = 8$  MeV - on Figs. 64 and 65.

At  $E_n = 20$  and 14 MeV major contributions to the first neutron spectrum come from (n,2n) and (n,3n) reactions spectra (see Figs. 57, 61), at lower energy  $E_n = 8$  MeV major contribution comes from (n,2n) reaction (see Fig. 64). Spectrum of (n,n $\gamma$ ) reaction actually is just hard energy tail of ‘pre-equilibrium’ component of first neutron spectrum. Shapes of first neutron spectra of (n,n $\gamma$ ) and (n,2n $\gamma$ ) reactions at  $E_n = 20$  (Fig. 57) and 14 MeV (Fig. 61) are rather similar, soft part being defined by neutron emission competition of higher neutron multiplicity reactions. This lowering of soft part of first neutron spectrum of (n,2n $\gamma$ ) reaction disappears for  $E_n = 8$  MeV (see Fig. 64).

At  $E_n = 20$  MeV major contribution to the second neutron spectrum (up to  $E \sim 8$  MeV) comes from (n,3n) reaction (see Fig. 58). Soft parts of the second neutron spectra of (n,2n) and (n,2nf) reactions are comparable. At lower incident neutron energy  $E_n = 14$  MeV major contribution to the second neutron spectrum comes from (n,2n $\gamma$ ) reaction (see Fig. 62). At lower energy  $E_n = 8$  MeV major contribution to the second neutron spectrum, obviously, comes from (n,2n $\gamma$ ) reaction (see Fig. 65).

At  $E_n = 20$  MeV most contribution to the third neutron spectrum comes from (n,3n $\gamma$ ) reaction (see Fig. 59), that of the (n,3nf) reaction being rather low.

### 8.2.3 Comparison with previous evaluations

The PFNS for the  $^{233}\text{Pa}$  data files of ENDF/B-VI [10] and JENDL-3.3 [13] libraries coincide, they were assumed to be Maxwellian. The peculiarities similar to  $^{238}\text{U}$ ,  $^{232}\text{Th}$  nuclei [46] for which the experimental data are available, are also noticed. The PFNS calculated with present model demonstrate more complicated

shape as compared with simple Maxwellian estimate for  $E_n = 2$  MeV (Fig. 66).

Above emissive fission threshold at  $E_n \gtrsim 7$  MeV the contribution of the second chance fission reaction  $^{233}\text{Pa}(n,f)$  is much higher than that of non-emissive fission (see Figs. 49, 50). The average energy removed by first pre-fission neutron is much smaller than the average energy of post-fission neutrons. This peculiarity explains appearance of low energy bump in the spectrum of fission neutrons (see Fig. 67). At higher incident neutron energies of  $E_n = 14$  and 20 MeV (see Figs. 68 and 69), the PFN spectrum also consists of several components. One of them is connected with pre-equilibrium first neutron emission and produces bump at  $E_{th} \sim E_n - B_{fA} \sim 7$  MeV prompt fission neutron energy for  $E_n = 14$  MeV or  $E_{th} \sim 12$  MeV for  $E_n = 20$  MeV,  $B_{fA}$  is the effective fission barrier of  $^{233}\text{Pa}$  fissioning nuclide. Soft neutron component connected with pre-fission neutrons from  $(n,2nf)$  reaction is noticed on Fig. 68 for  $E_n = 14$  MeV. Irregularity around 7 MeV for PFNS for  $E_n = 20$  MeV (see Fig. 69) might be correlated with the first neutron spectrum of  $^{233}\text{Pa}(n,2nf)$  reaction,  $P_{21}(E, E_n) ((n,2nf)^1)$ , it is sensitive to the description of fission probability of  $^{232}\text{Pa}$  near fission threshold.

The average energy of the fission neutron versus incident energy is shown in Fig. 70. At incident neutron energy  $E_n \lesssim 5.5$  MeV, the  $\nu_p$ -value energy dependence is proportional to  $\sqrt{U_i}$ , however, at higher excitations we have more complicated excitation energy dependence. At  $E_n \sim 7$  MeV the average energy reduces by  $\sim 400$  keV due to the contribution of low energy neutrons from  $(n,nf)$  reaction. This tendency, visible in measured data for the  $^{238}\text{U}(n,f)$  PFNS, is predicted for the  $^{233}\text{Pa}(n,f)$  reaction.

### 8.3 Neutron emission spectra comparison

There is no measured data on neutron emission spectra for  $^{233}\text{Pa}+n$  interaction. For incident neutron energy higher than emissive fission threshold, emissive neutron spectrum is deconvoluted, components of 1st, 2nd and 3d neutron spectra are provided, where applicable. We have calculated 1st, 2nd and 3d neutron spectra for the  $(n,n\gamma)$ ,  $(n,2n)$  and  $(n,3n)$  reactions.

According to the ENDF/B-VI format specifications the secondary neutron spectra are included in the following way. Calculated spectra were summed up and tabular spectra for the  $(n,n\gamma)$ ,  $(n,2n)$  and  $(n,3n)$  reactions were obtained.

Spectrum of  $(n,n\gamma)$  reaction actually is just hard energy tail of ‘pre-equilibrium’ component of first neutron spectrum. Spectrum of the first neutron of  $(n,2n)$  reaction is much softer, although ‘pre-equilibrium’ component still comprise appreciable part of it. First neutron spectrum of  $(n,3n)$  reaction is actually of evaporative nature. First neutron spectrum of  $(n,nf)$  reaction has rather long pre-equilibrium high-energy tail. First neutron spectrum of  $(n,2nf)$  reaction, as that of  $(n,3n)$  reaction, is of evaporative nature.

Figures 71-76 compare neutron spectra of  $(n,n\gamma)$  reaction of JENDL-3.3 [13] and ENDF/B-VI [10] with present calculation. Neutron spectra of ENDF/B-VI

[10] and JENDL-3.3 [13] are evaporative. At  $E_n = 20$  and 14 MeV hard energy tails of ‘pre-equilibrium’ component of first neutron spectrum of JENDL-3.3 [13] and present evaluation are rather pronounced. Average energies of first neutron spectra for ENDF/B-VI are much lower than that of present evaluation.

Table 9

Average energies of secondary neutron spectra for  $^{233}\text{Pa}+n$

1st neutron average energy $\langle E \rangle$ , MeV							
$E_n, \text{MeV}$	(n,n')			(n,2n)	(n,n'f)	(n,3n)	(n,2n'f)
	Present	B-VI	J-3.3	Present			
6.0	1.118	-	0.902	0.000	0.030		
8.0	2.621	-	1.050	0.622	1.077		
10.0	4.708	-	1.178	1.192	1.582		
14.0	8.820	-	1.399	2.748	2.657	0.954	0.657
20.0	14.644	1.886	1.676	8.650	3.274	3.401	2.712

Table 9 (continued)

Average energies of secondary neutron spectra for  $^{233}\text{Pa}+n$

$\langle E \rangle$ for (n,2n), MeV				$\langle E \rangle$ for (n,3n), MeV		
$E_n, \text{MeV}$	Present	J-3.3	B-VI	Present	J-3.3	B-VI
8.0	0.524	0.677	0.552	-	-	-
10.0	0.952	0.950	-	-	-	-
14.0	1.873	1.175	-	0.643	0.817	-
20.0	4.900	1.495	1.257	1.874	1.264	2.227

Figures 86, 87, 88 and 89 show the comparison of (n,2n) reaction spectra of JENDL-3.2, ENDF/B-VI and present evaluation at  $E_n = 20, 14, 10$  and 8 MeV. The discrepancies above  $\sim 5$  MeV and  $\sim 3$  MeV,  $\sim 1$  MeV and  $\sim 0.5$  MeV respectively, are due to first neutron spectra of (n,2n) reaction in present calculation being of hard pre-equilibrium nature. Figure 89 shows the comparison of (n,2n) reaction spectra at 8 MeV. Figures 90 and 91 show spectra of (n,3n) reaction for incident neutron energy of 14 and 20 MeV, respectively.

In summary, inclusion of pre-equilibrium emission changes significantly the average energies of emitted neutron spectra. That is shown in Table 11, where the average secondary neutron energies for current, ENDFB-VI and JENDL-3.2 evaluations are compared. The most significant is the change of neutron spectra of (n,n $\gamma$ ) reaction.

## 9 Conclusions

The statistical Hauser-Feshbach-Moldauer model calculation of neutron-induced reaction cross sections for  $^{233}\text{Pa}$  target nuclide shows the fair description of available data base on fission cross section. Statistical calculations were employed for predicting total, capture, inelastic, (n,2n) and (n,3n) reaction cross sections. Rigid and soft rotator coupled channel models were used to predict inelastic scattering cross sections for level excitation. Prompt fission neutron spectra are predicted with the model, tested on the PFNS description of  $^{238}\text{U}(\text{n,f})$  and  $^{232}\text{Th}(\text{n,f})$  reactions.

## 10 Acknowledgments

This work was supported within the Project B-404 "Actinide Nuclear Data Evaluation" of International Science and Technology Center (Funding Party Japan).

## References

- [1] Von Gunten H.R., Buchanan R.F., Wytttenbach A. Nucl. Sci. Eng, 27, 85 (1966).
- [2] Tovesson F., Hambsch F.-J., Oberstedt A., et al., Phys. Rev. Lett., 88 (6), 062502-1 (2002).
- [3] Hambsch F.-J, Tovesson F., Oberstedt S., et al., 10th International Seminar on Interaction of Neutron with Nuclei, 22-25 May 2002, Dubna, 202 (2003).
- [4] Petit M., Aiche M., Andriamonje S., et al., Actinide and Fission Product Partitioning and Transmutation, Madrid, Spain, December, 11-13, 2000, p. 751 (2000).
- [5] Maslov V.M., Porodzinskij Yu. V., Baba M., Hasegawa A., Kornilov N.V., Kagalenko A.B., Proc. International Conference on Nuclear Data for Science and Technology, October 7-12, 2001, Tsukuba, Japan, p. 148, 2002.
- [6] Maslov V.M. , Yu. V. Porodzinskij, M. Baba, A. Hasegawa, Ann. Nucl. Energy, 29, 1707 (2002).
- [7] Maslov V.M., Porodzinskij Yu. V., Baba M., Hasegawa A., Nucl. Sci. Eng. (2003).

- [8] Maslov V.M., Porodzinskij Yu. V., Baba M., Hasegawa A., Ann. Nucl. Energy, 30, 1155 (2003).
- [9] Maslov V.M., Baba M., Hasegawa A., Kornilov N.V., Kagalenko A.B. and Tetereva N.A., INDC(BLR)-019, Vienna, (in print).
- [10] Roussin R.W., Young P.G., McKnight R., Proc. Int. Conf. Nuclear Data for Science and Technology, Gatlinburg, USA, May 9-13, 1994, p. 692, J.K. Dickens (Ed.), ANS, 1994.
- [11] Simpson F.B., Coddington Jr J.W. Nucl. Sci. Eng., 28, 133, (1967).
- [12] Harris D.R., WAPD-TM-814 (1969).
- [13] Shibata K., Kawano T., Nakagawa T. et al., J. Nucl. Sci. Technol., 39, 1125 (2002).
- [14] Mughabghab S.F. Neutron Cross Sections, V. 1, Part B, (1984).
- [15] Maslov V.M., Porodzinskij Yu.V. JAERI-Research 98-038, Japan, 1998.
- [16] Handbook for Calculations of Nuclear Reaction Data: Reference input parameter library, IAEA-TECDOC-1034, p.81, 1998, Vienna.
- [17] Ignatjuk A.V., Istekov K.K., Smirenkin G.N. Sov. J. Nucl. Phys. 29, 450 (1979).
- [18] Moldauer P.A., Proc. Conf. on Neutron Cross Sections and Technology, Washington, D.C., USA, March 22-24, 1966, p. 613-622, AEC (1966).
- [19] Stavinskij V.S., Shaker M.O., Nucl. Phys., 62, 667 (1965).
- [20] Maslov V.M., INDC(BLR)-013, IAEA, Vienna, 1998.
- [21] Cullen D. PREPRO2000: 2000 ENDF/B Pre-Processing Codes.
- [22] NJOY 94.10 Code System for Producing Pointwise and Multigroup Neutron and Photon Cross Sections from ENDF/B Data, RSIC Peripheral Shielding Routine Collection, ORNL, PSR-355, LANL, Los Alamos, New Mexico (1995).
- [23] Maslov V.M., Porodzinskij Yu.V., Baba M., Hasegawa A., Kornilov N.V., Kagalenko A.B. and Tetereva N.A., INDC(BLR)-016, Vienna, 2003.
- [24] Moldauer P.A., Phys. Rev., C11, 426 (1975).
- [25] Maslov V.M., Nuclear Reaction data and Nuclear Reactors, Trieste, Italy, 2000, pp. 231-268, ICTP, 2001.



- [26] Ignatjuk A.V., Maslov V.M., Proc. Int. Symp. Nuclear Data Evaluation Methodology, Brookhaven, USA, October 12-16, 1992, p.440, World Scientific, 1993.
- [27] Maslov V.M., Kikuchi Y., JAERI-Research 96-030, 1996.
- [28] Tepel J.W., Hoffman H.M., Weidenmuller H.A. Phys. Lett. 49, 1 (1974).
- [29] Howard W.M., Möller P. Atomic Data and Nuclear Data Tables, 25, 219 (1980).
- [30] Shurshikov E.N., Nuclear Data Sheets, 53, 601 (1988).
- [31] ENSDF: Evaluated Nuclear Structure Data File, BNL/NNDC, 1993.
- [32] Maslov V.M., Zeit. Phys. A, Hadrons & Nuclei, 347, 211 (1994).
- [33] Fu C. Nucl. Sci. Engng. 86, 344 (1984).
- [34] Maslov V.M., Porodzinskij Yu.V., Hasegawa A., Shibata K. JAERI-Research 98-040, Japan, 1998.
- [35] Maslov V.M., Physics of Atomic Nuclei, 63, 161 (2000).
- [36] Myers W.O., Swiatecky W.J., Ark. Fyzik, 36, 243 (1967).
- [37] Bjornholm S., Lynn J.E. Rev. Mod. Phys., 52, 725 (1980).
- [38] Ellis Y.A. Nucl. Data Sheets, 24, 289 (1978).
- [39] V.M. Maslov, Yu. V. Porodzinskij, M. Baba, A. Hasegawa, Proc. 11th Intern. Symp. on Capture and Gamma-ray Spectroscopy, September 2-6, 2002, Prague, Czech Republic.
- [40] Britt H.C., Wilhelmy J.B., Nucl. Sci. Eng., 72, 222 (1979).
- [41] Uhl M., Strohmaier B., IRK-76/01, IRK, Vienna (1976).
- [42] Bois, R., Frehaut, J.: CEA-R-4791 (1976).
- [43] Malinovskij V.V. VANT (ser. Yadernye constanty), 1987, No.2, 25.
- [44] Tuttle R.J.: INDC(NDS)-107/G+Special, p.29 (1979).
- [45] V.M. Maslov, Yu. V. Porodzinskij, M. Baba, A. Hasegawa, N.V. Kornilov, A.B. Kagalenko, Tetereva N.A., EuroPhysics Journal A, 18 (2003) 93.
- [46] V.M. Maslov, Yu. V. Porodzinskij, M. Baba, A. Hasegawa, N.V. Kornilov, A.B. Kagalenko, Proc. X International Seminar on Interaction of Neutrons with Nuclei, Dubna, Russia, May 17-20, 2002, 2002.

- [47] Kornilov N.V., Kagalenko A.B., Hambsch F.-J. Physics of Atomic Nuclei, 62, 173 (1999)

## 11 Figure captions

- Fig. 1 Cumulative sum of levels of  $^{233}\text{Pa}$ .  
Fig. 2 Cumulative sum of reduced neutron widths of  $^{233}\text{Pa}$ .  
Fig. 3 Level spacing distribution of  $^{233}\text{Pa}$ .  
Fig. 4 Reduced neutron width distribution of  $^{233}\text{Pa}$ .  
Fig. 5 Cumulative distribution of reduced neutron widths of  $^{233}\text{Pa}$ .  
Fig. 6 Total cross section of  $^{233}\text{Pa}$ .  
Fig. 7 Elastic cross section of  $^{233}\text{Pa}$ .  
Fig. 8 Fission cross section of  $^{233}\text{Pa}$ .  
Fig. 9 Capture cross section of  $^{233}\text{Pa}$ .  
Fig. 10 Inelastic cross section of  $^{233}\text{Pa}$ .  
Fig. 11 Average level spacing of  $^{233}\text{Pa}$ ,  $l = 0$ ,  $J = 1$ .  
Fig. 12 Average level spacing of  $^{233}\text{Pa}$ ,  $l = 0$ ,  $J = 2$ .  
Fig. 13 Average level spacing of  $^{233}\text{Pa}$ ,  $l = 1$ ,  $J = 0$ .  
Fig. 14 Average level spacing of  $^{233}\text{Pa}$ ,  $l = 1$ ,  $J = 3$ .  
Fig. 15 Average reduced neutron width of  $^{233}\text{Pa}$ ,  $l = 0$ ,  $J = 1$ .  
Fig. 16 Average reduced neutron width of  $^{233}\text{Pa}$ ,  $l = 0$ ,  $J = 2$ .  
Fig. 17 Average reduced neutron width of  $^{233}\text{Pa}$ ,  $l = 1$ ,  $J = 0$ .  
Fig. 18 Average reduced neutron width of  $^{233}\text{Pa}$ ,  $l = 1$ ,  $J = 1$ .  
Fig. 19 Average reduced neutron width of  $^{233}\text{Pa}$ ,  $l = 1$ ,  $J = 2$ .  
Fig. 20 Total cross section of  $^{233}\text{Pa}$ .  
Fig. 21 Elastic scattering cross section of  $^{233}\text{Pa}$ .  
Fig. 22 Cumulative number of levels of  $^{233}\text{Pa}$ .  
Fig. 23 Cumulative number of levels of  $^{234}\text{Pa}$ .  
Fig. 24 Level density of  $^{233}\text{Pa}$ .  
Fig. 25 Fission cross section of  $^{233}\text{Pa}$ .  
Fig. 26 Fission cross section of  $^{233}\text{Pa}$ .  
Fig. 27 Cross section of  $^{233}\text{Pa}$ : 0.0067 MeV,  $1/2^-$  level excitation.  
Fig. 28 Cross section of  $^{233}\text{Pa}$ : 0.0572 MeV,  $7/2^-$  level excitation..  
Fig. 29 Cross section of  $^{233}\text{Pa}$ : 0.0706 MeV,  $5/2^-$  level excitation.  
Fig. 30 Cross section of  $^{233}\text{Pa}$ : 0.0865 MeV,  $5/2^+$  level excitation.  
Fig. 31 Cross section of  $^{233}\text{Pa}$ : 0.0947 MeV,  $3/2^+$  level excitation.  
Fig. 32 Cross section of  $^{233}\text{Pa}$ : 0.1036 MeV,  $7/2^+$  level excitation.  
Fig. 33 Cross section of  $^{233}\text{Pa}$ : 0.1090 MeV,  $9/2^+$  level excitation.  
Fig. 34 Cross section of  $^{233}\text{Pa}$ : 0.1634 MeV,  $11/2^+$  level excitation.  
Fig. 35 Cross section of  $^{233}\text{Pa}$ : 0.1691 MeV,  $1/2^+$  level excitation.  
Fig. 36 Cross section of  $^{233}\text{Pa}$ : 0.1792 MeV,  $9/2^-$  level excitation.  
Fig. 37 Cross section of  $^{233}\text{Pa}$ : 0.2017 MeV,  $3/2^+$  level excitation.  
Fig. 38 Cross section of  $^{233}\text{Pa}$ : 0.21234 MeV,  $5/2^+$  level excitation.  
Fig. 39 Cross section of  $^{233}\text{Pa}$ : 0.2379 MeV,  $9/2^+$  level excitation.  
Fig. 40 Cross section of  $^{233}\text{Pa}$ : 0.2573 MeV,  $5/2^-$  level excitation.  
Fig. 41 Cross section of  $^{233}\text{Pa}$ : 0.2796 MeV,  $7/2^+$  level excitation.

Fig. 42 Cross section of  $^{233}\text{Pa}$ : 0.3004 MeV,  $7/2^-$  level excitation.

Fig. 43 Cross section of  $^{233}\text{Pa}$ : 0.3061 MeV,  $7/2^+$  level excitation.

Fig. 44 Cross section of  $^{233}\text{Pa}$ : 0.3661 MeV,  $9/2^+$  level excitation.

Fig. 45 Total inelastic scattering cross section of  $^{233}\text{Pa}$ .

Fig. 46 Continuum inelastic scattering cross section  $^{233}\text{Pa}$ .

Fig. 47 Total inelastic scattering cross section of  $^{233}\text{Pa}$ .

Fig. 48 Capture cross section of  $^{233}\text{Pa}$ .

Fig. 49 Fission cross section of  $^{233}\text{Pa}$ .

Fig. 50 Chance fission contributions to the fission cross section of  $^{233}\text{Pa}$ .

Fig. 51. Fission cross section of  $^{232}\text{Pa}$ .

Fig. 52 Fission cross section of  $^{231}\text{Pa}$ .

Fig. 53 (n,2n) cross section of  $^{233}\text{Pa}$ .

Fig. 54 (n,3n) cross section of  $^{233}\text{Pa}$ .

Fig. 55 Prompt fission neutron number of  $^{233}\text{Pa}$ .

Fig. 56 Prompt fission neutron number of  $^{233}\text{Pa}$ .

Fig. 57 Components of first neutron spectrum of  $^{233}\text{Pa}$  for incident neutron energy 20 MeV.

Fig. 58 Components of second neutron spectrum of  $^{233}\text{Pa}$  for incident neutron energy 20 MeV.

Fig. 59 Components of third neutron spectrum of  $^{233}\text{Pa}$  for incident neutron energy 20 MeV.

Fig. 60 Components of fourth neutron spectrum of  $^{233}\text{Pa}$  for incident neutron energy 20 MeV.

Fig. 61 Components of first neutron spectrum of  $^{233}\text{Pa}$  for incident neutron energy 14 MeV.

Fig. 62 Components of second neutron spectrum of  $^{233}\text{Pa}$  for incident neutron energy 14 MeV.

Fig. 63 Components of third neutron spectrum of  $^{233}\text{Pa}$  for incident neutron energy 14 MeV.

Fig. 64 Components of first neutron spectrum of  $^{233}\text{Pa}$  for incident neutron energy 8 MeV.

Fig. 65 Components of second neutron spectrum of  $^{233}\text{Pa}$  for incident neutron energy 8 MeV.

Fig. 66 PFNS for  $^{233}\text{Pa}$  at incident neutron energy 2 MeV.

Fig. 67 PFNS for  $^{233}\text{Pa}$  at incident neutron energy 7 MeV.

Fig. 68 PFNS for  $^{233}\text{Pa}$  at incident neutron energy 14 MeV.

Fig. 69 PFNS for  $^{233}\text{Pa}$  at incident neutron energy 20 MeV.

Fig. 70 Average neutron energy of the PFNS for  $^{233}\text{Pa}$ .

Fig. 71 Comparison of (n,n' $\gamma$ ) reaction neutron spectra of  $^{233}\text{Pa}$  for incident neutron energy 20 MeV.

Fig. 72 Comparison of (n,n' $\gamma$ ) reaction neutron spectra of  $^{233}\text{Pa}$  for incident neutron energy 14 MeV.

Fig. 73 Comparison of (n,n' $\gamma$ ) reaction neutron spectra of  $^{233}\text{Pa}$  for incident

neutron energy 10 MeV.

Fig. 74 Comparison of  $(n,n'\gamma)$  reaction neutron spectra of  $^{233}\text{Pa}$  for incident neutron energy 8 MeV.

Fig. 75 Comparison of  $(n,n'\gamma)$  reaction neutron spectra of  $^{233}\text{Pa}$  for incident neutron energy 6 MeV.

Fig. 76 Comparison of  $(n,n'\gamma)$  reaction neutron spectra of  $^{233}\text{Pa}$  for incident neutron energy 4 MeV.

Fig. 77 Comparison of  $(n,2n)$  reaction neutron spectra of  $^{233}\text{Pa}$  for incident neutron energy 20 MeV.

Fig. 78 Comparison of  $(n,2n)$  reaction neutron spectra of  $^{233}\text{Pa}$  for incident neutron energy 14 MeV.

Fig. 79 Comparison of  $(n,2n)$  reaction neutron spectra of  $^{233}\text{Pa}$  for incident neutron energy 10 MeV.

Fig. 80 Comparison of  $(n,3n)$  reaction neutron spectra of  $^{233}\text{Pa}$  for incident neutron energy 20 MeV.

Fig. 81 Comparison of  $(n,3n)$  reaction neutron spectra of  $^{233}\text{Pa}$  for incident neutron energy 14 MeV.

# $^{233}\text{Pa}$ CUMULATIVE SUM OF LEVELS

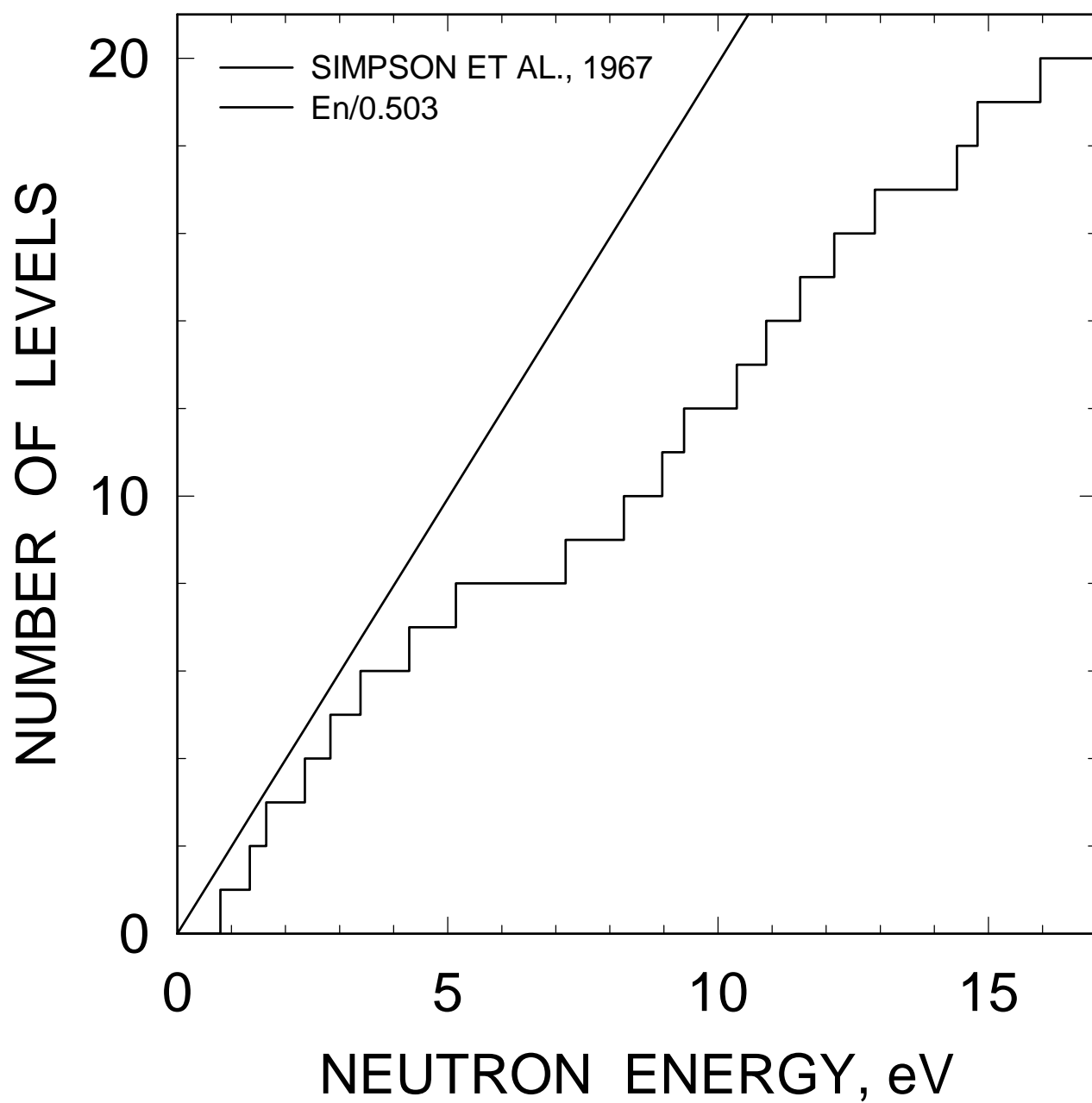


FIG. 1

# $^{233}\text{Pa}$ CUMULATIVE SUM OF REDUCED NEUTRON WIDTHS

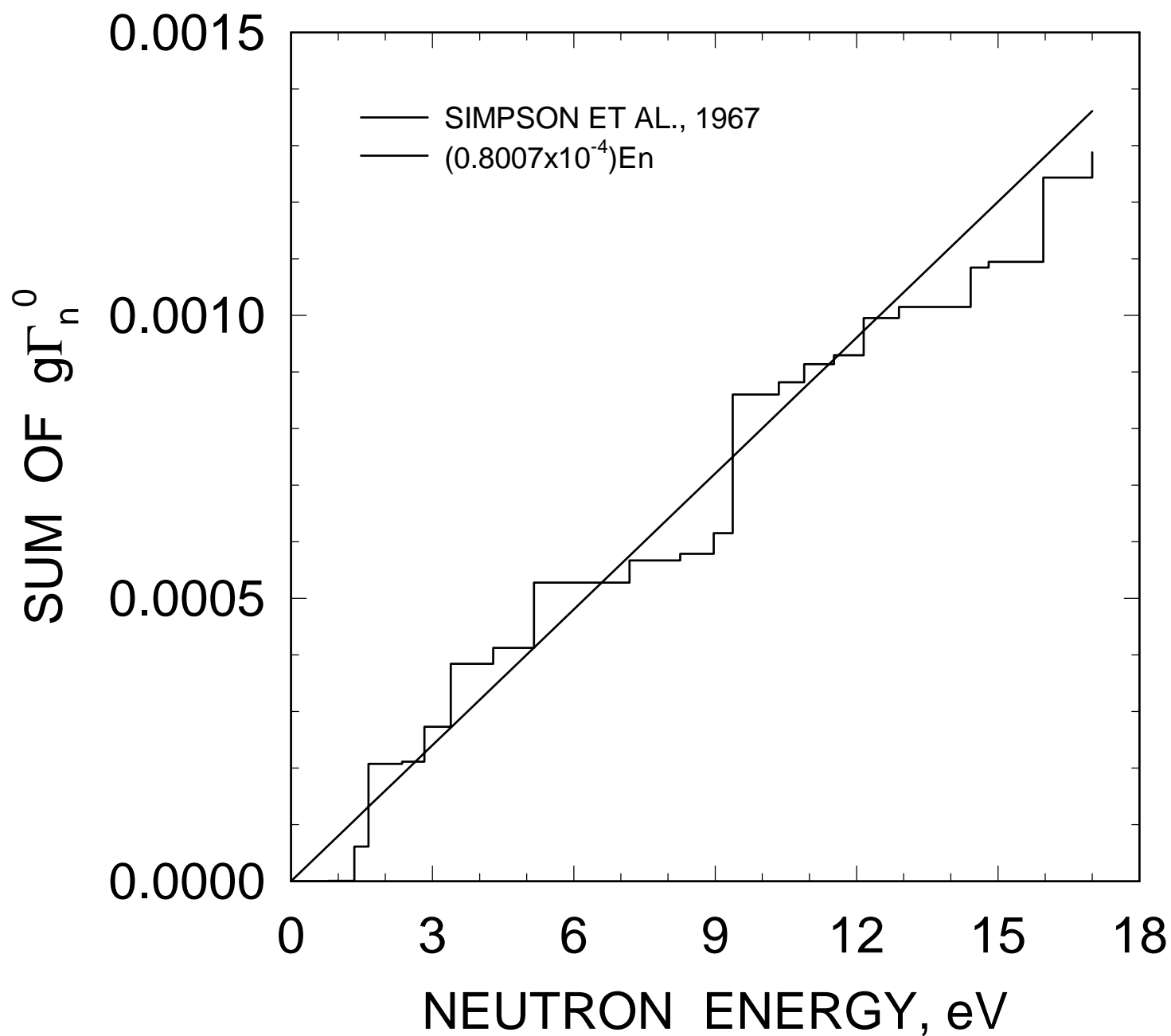


FIG. 2

# $^{233}\text{Pa}$ LEVEL SPACING DISTRIBUTION

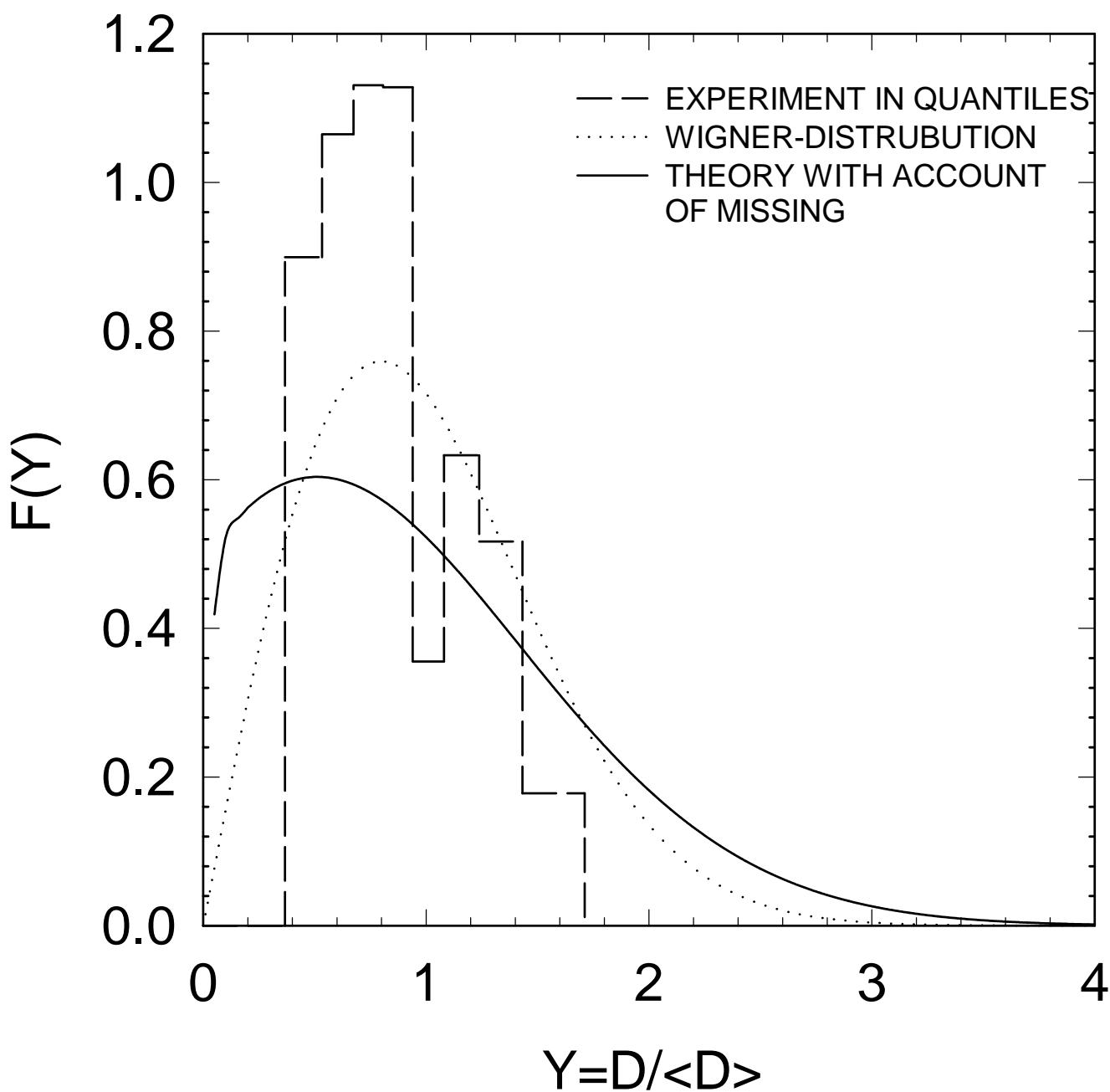


FIG. 3



# $^{233}\text{Pa}$ REDUCED NEUTRON WIDTH DISTRIBUTION

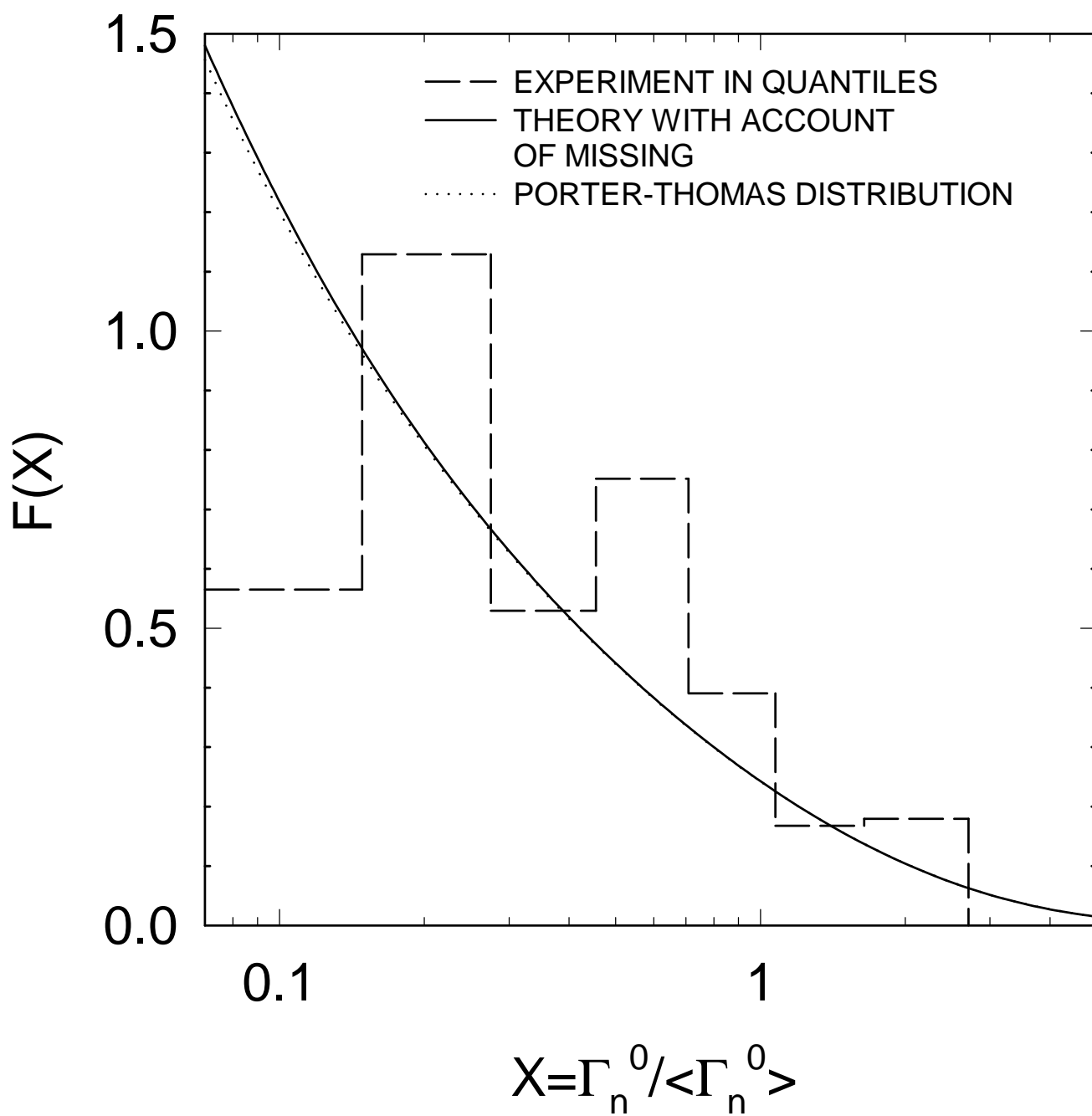


FIG. 4

<sup>233</sup>Pa CUMULATIVE PORTER-THOMAS  
DISTRIBUTION OF REDUCED  
NEUTRON WIDTHS

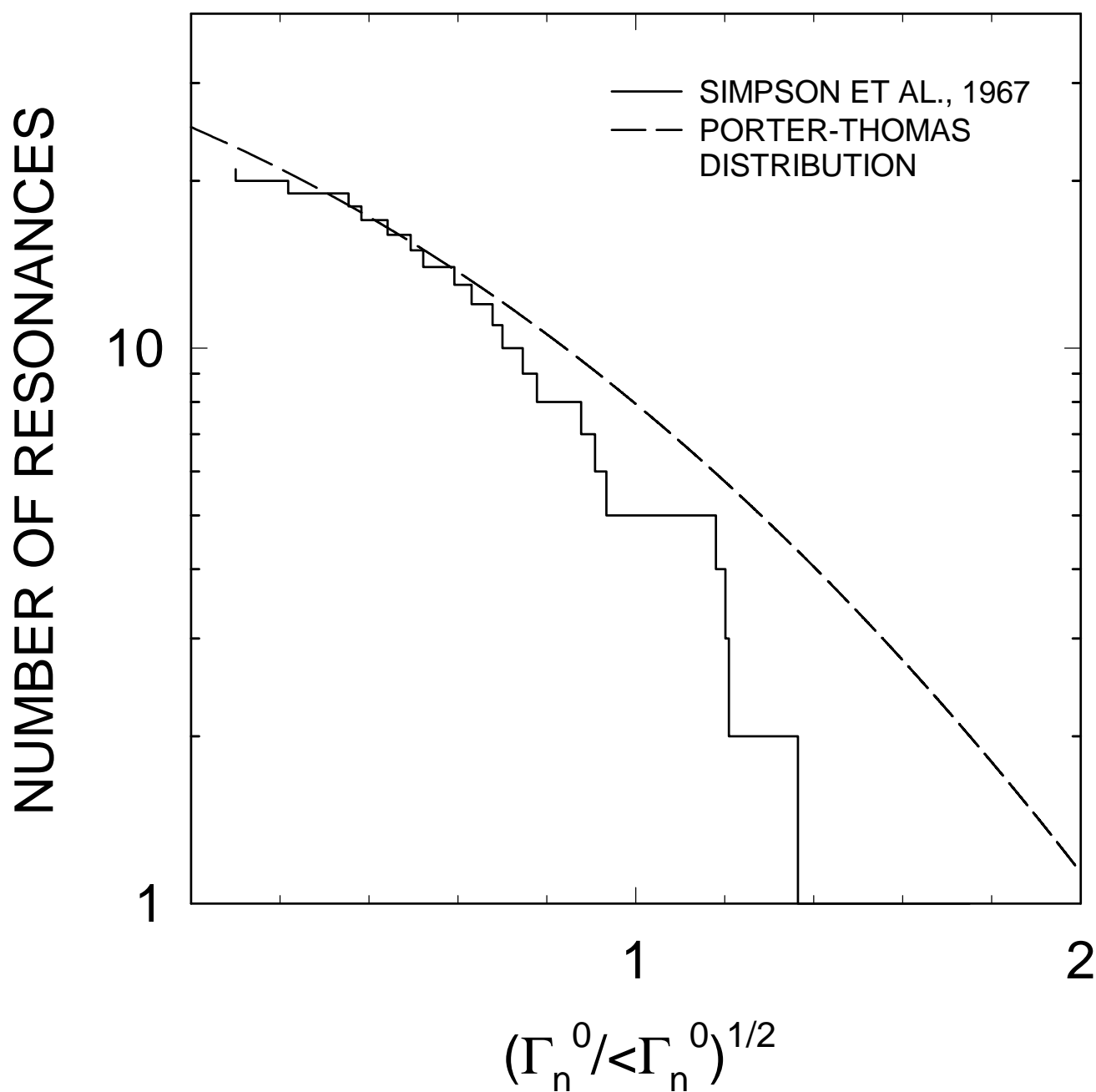


FIG. 5

# $^{233}\text{Pa}$ TOTAL CROSS SECTION

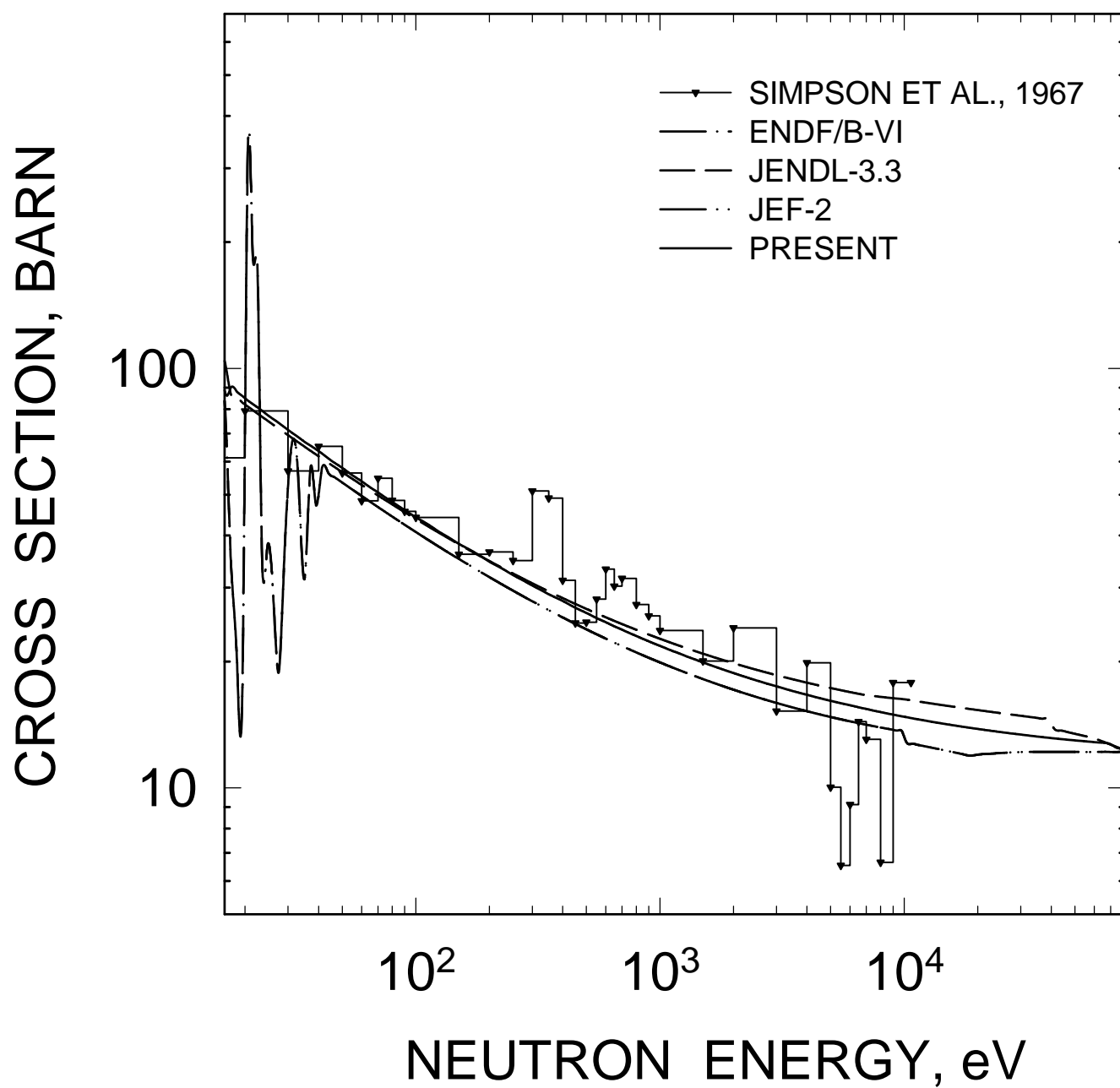


FIG. 6

# $^{233}\text{Pa}$ ELASTIC CROSS SECTION

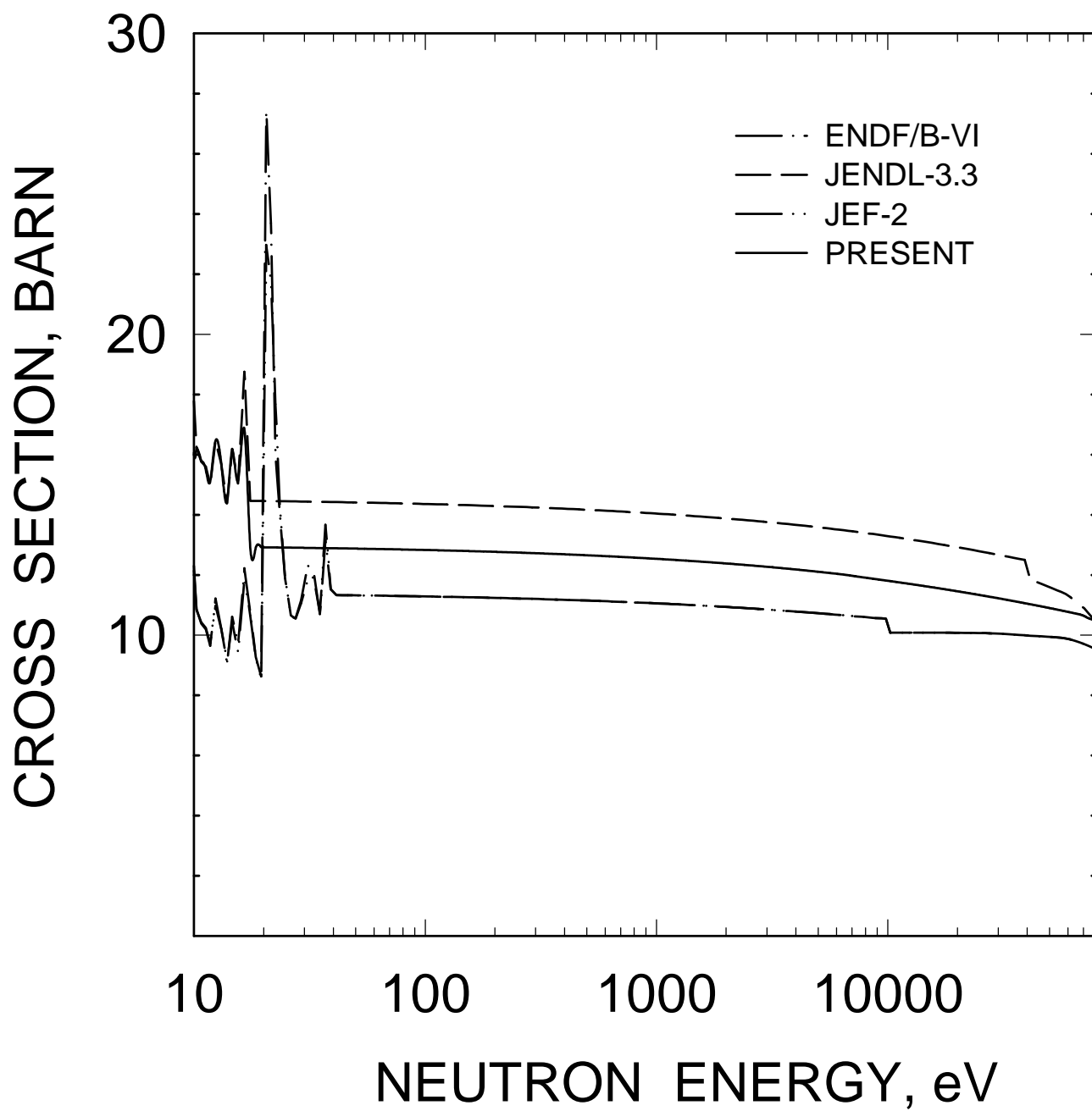


FIG. 7

# $^{233}\text{Pa}$ FISSION CROSS SECTION

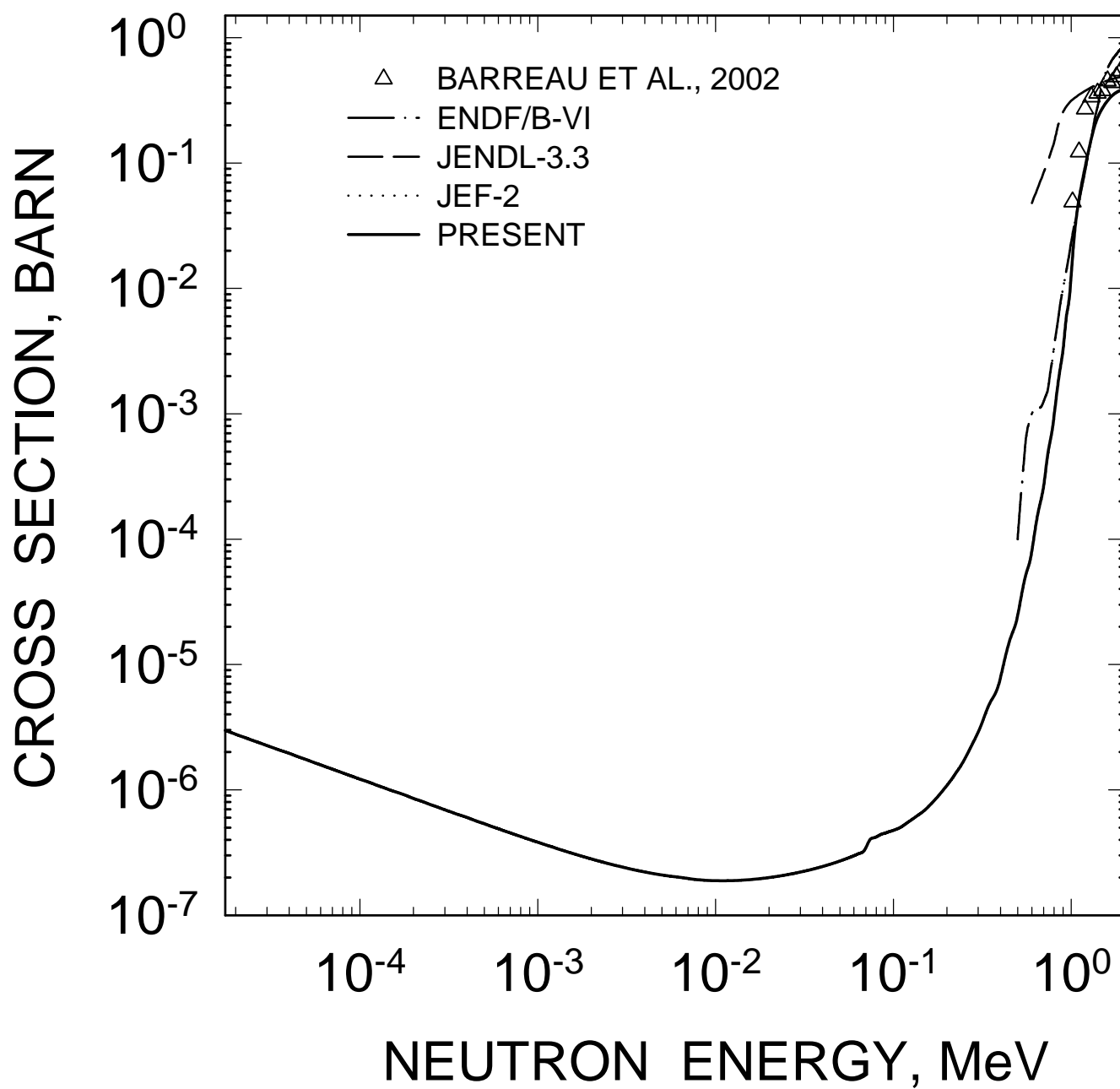


FIG. 8

# $^{233}\text{Pa}$ ( $n,\gamma$ ) CROSS SECTION

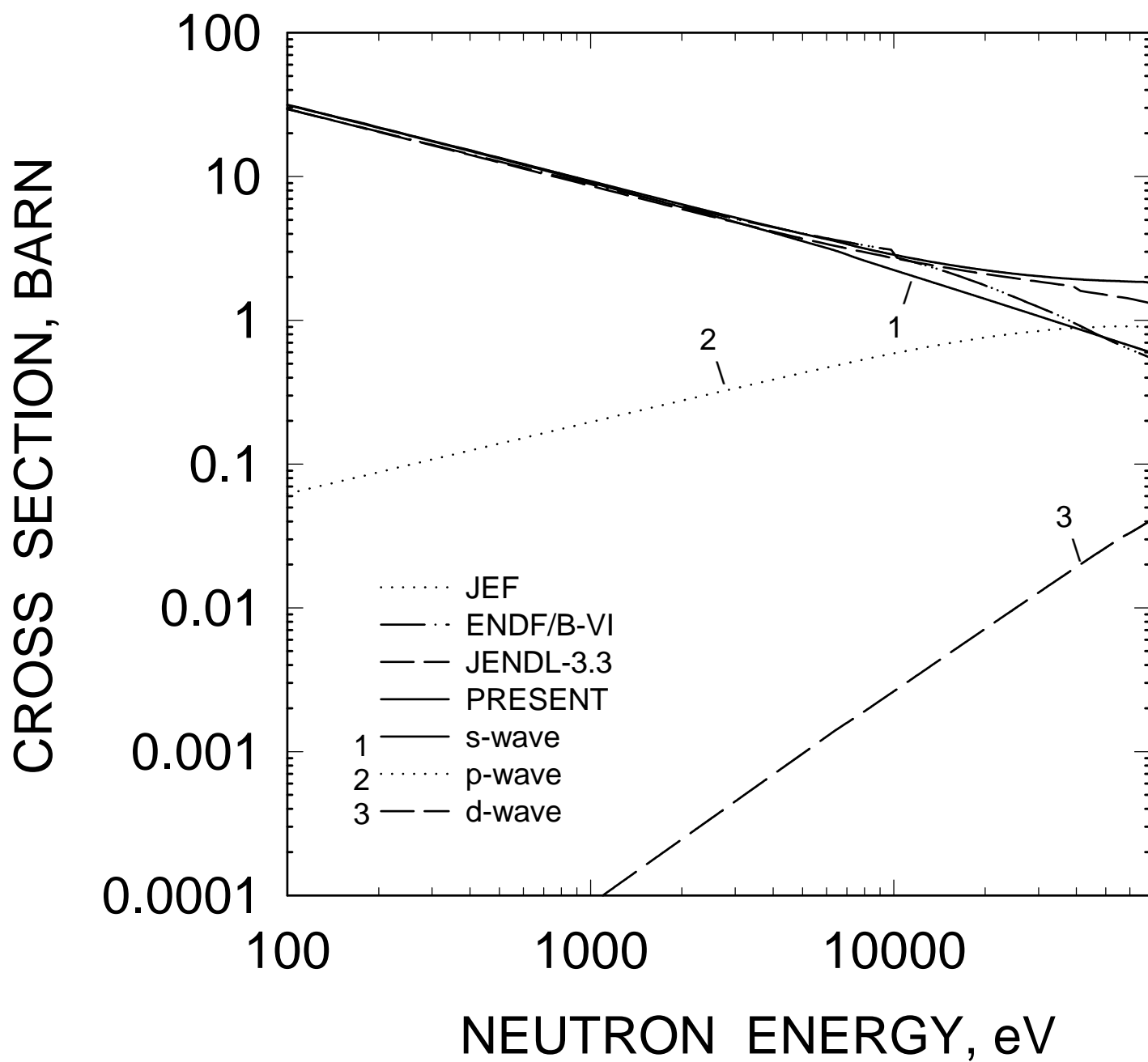


FIG. 9

# $^{233}\text{Pa}$ INELASTIC CROSS SECTION

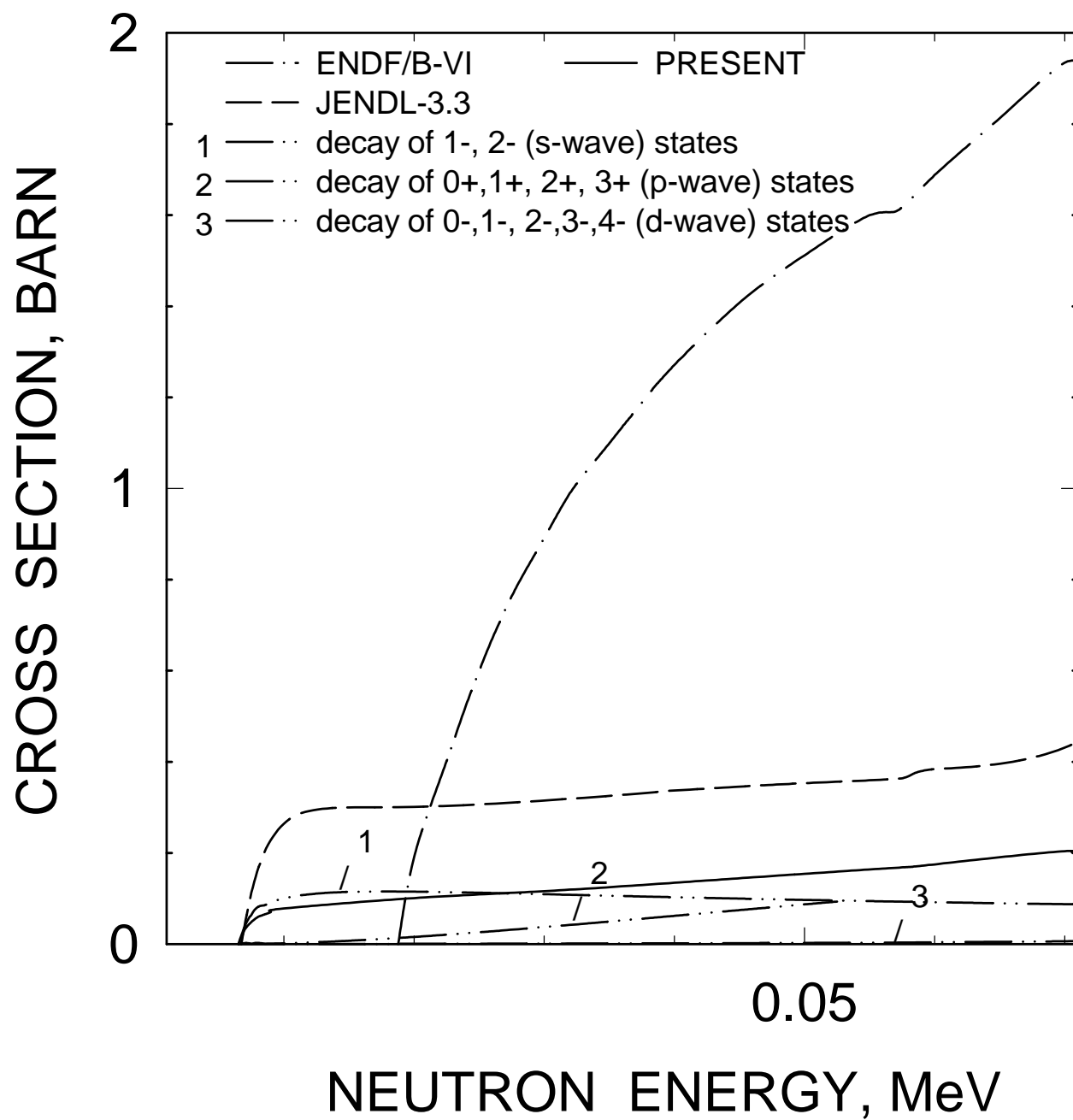


FIG. 10

$^{233}\text{Pa}$ : AVERAGE LEVEL SPACING  
( $L=0$ ,  $J=1$ )

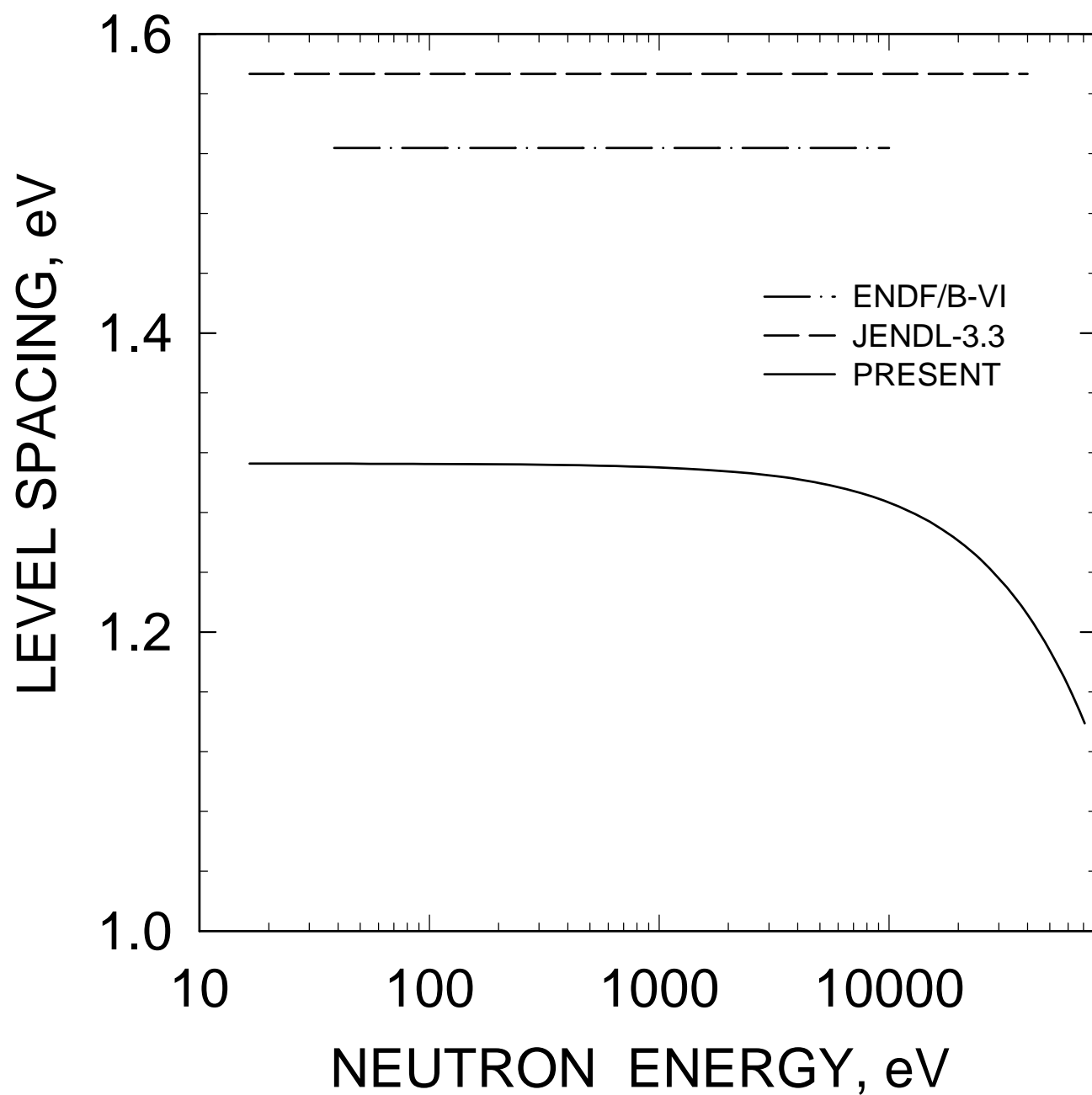


FIG. 11



<sup>233</sup>Pa: AVERAGE LEVEL SPACING  
(L=0, J=2)

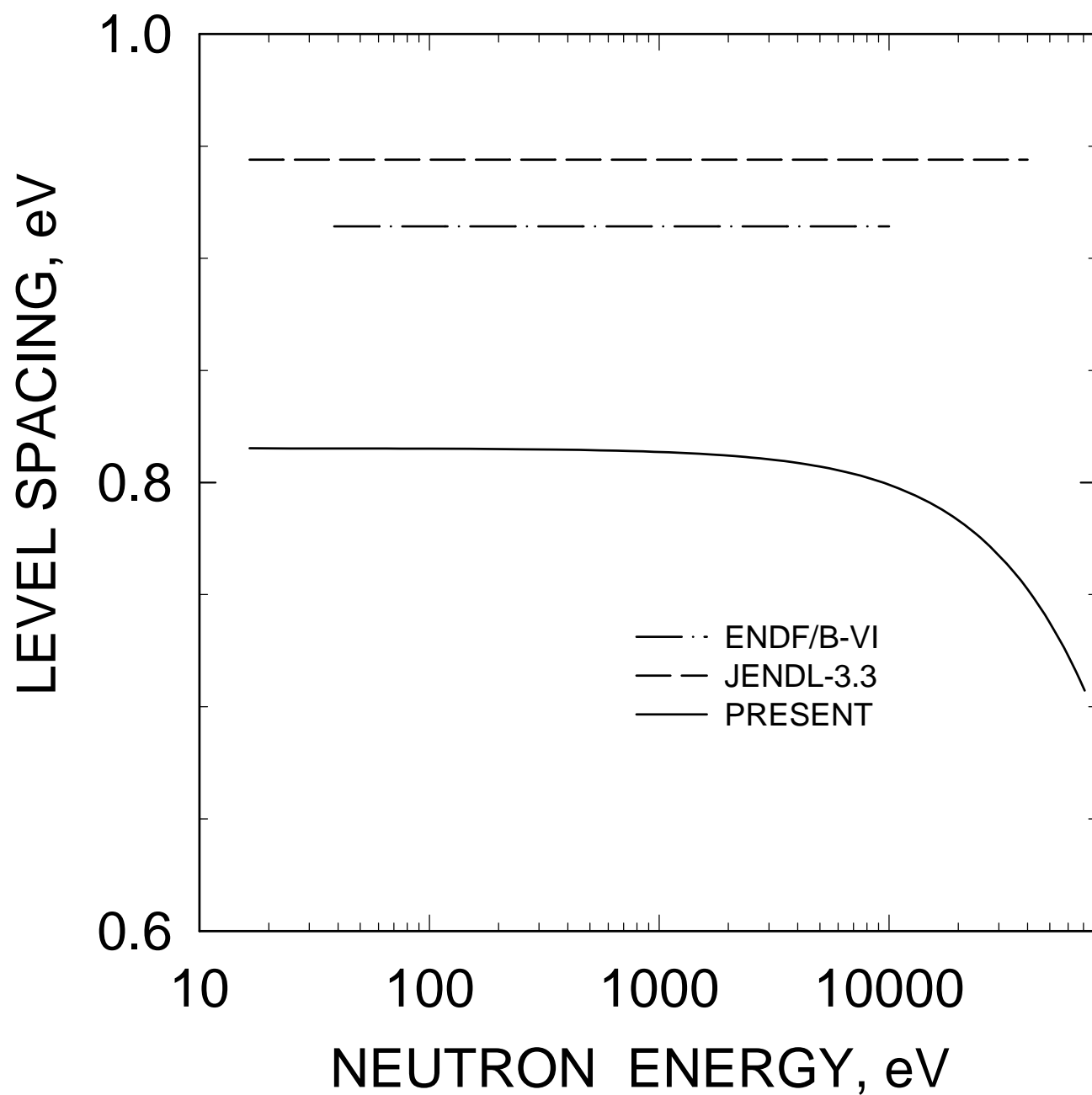


FIG. 12

<sup>233</sup>Pa: AVERAGE LEVEL SPACING  
(L=1, J=0)

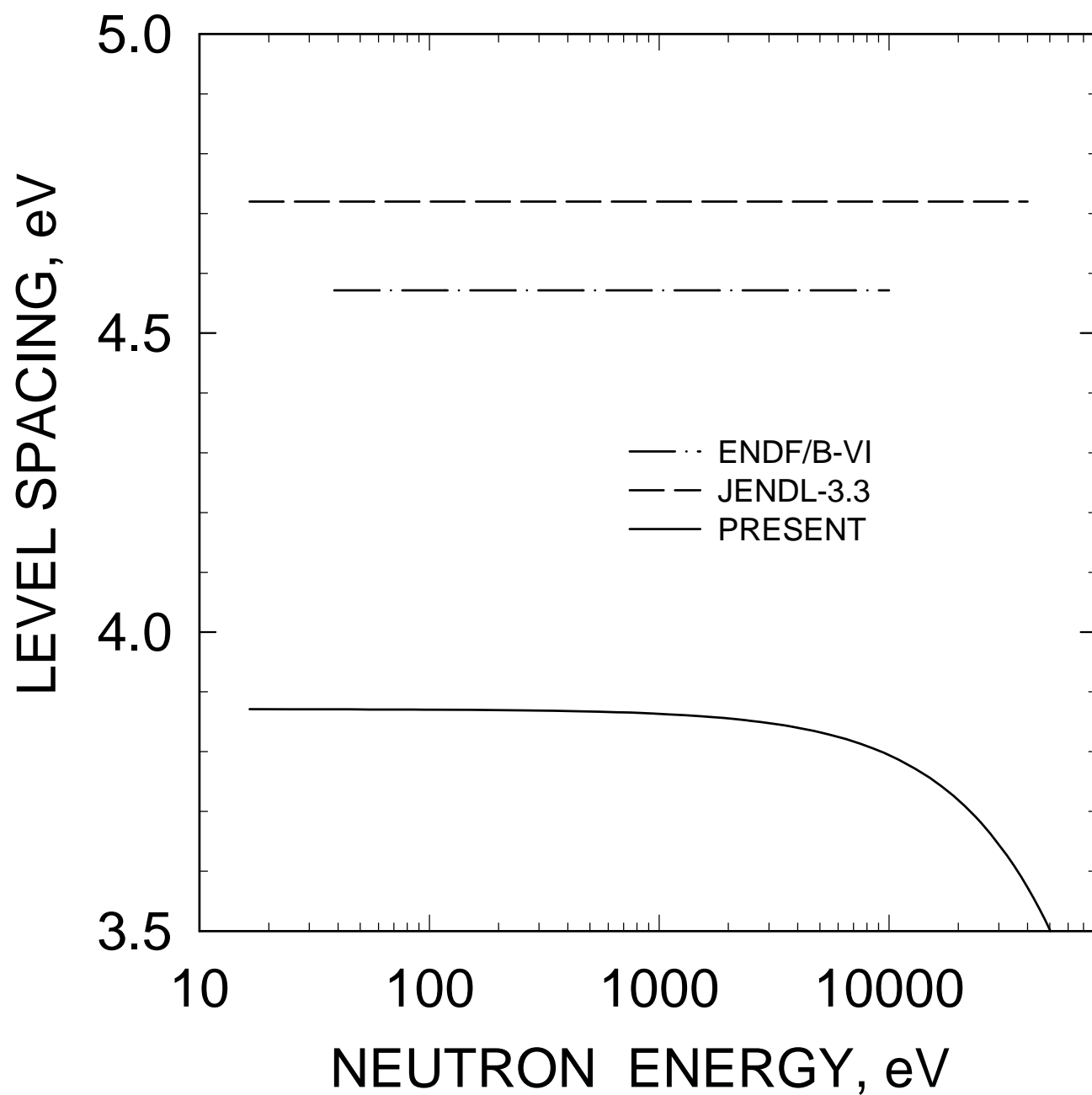


FIG. 13

<sup>233</sup>Pa: AVERAGE LEVEL SPACING  
(L=1, J=3)

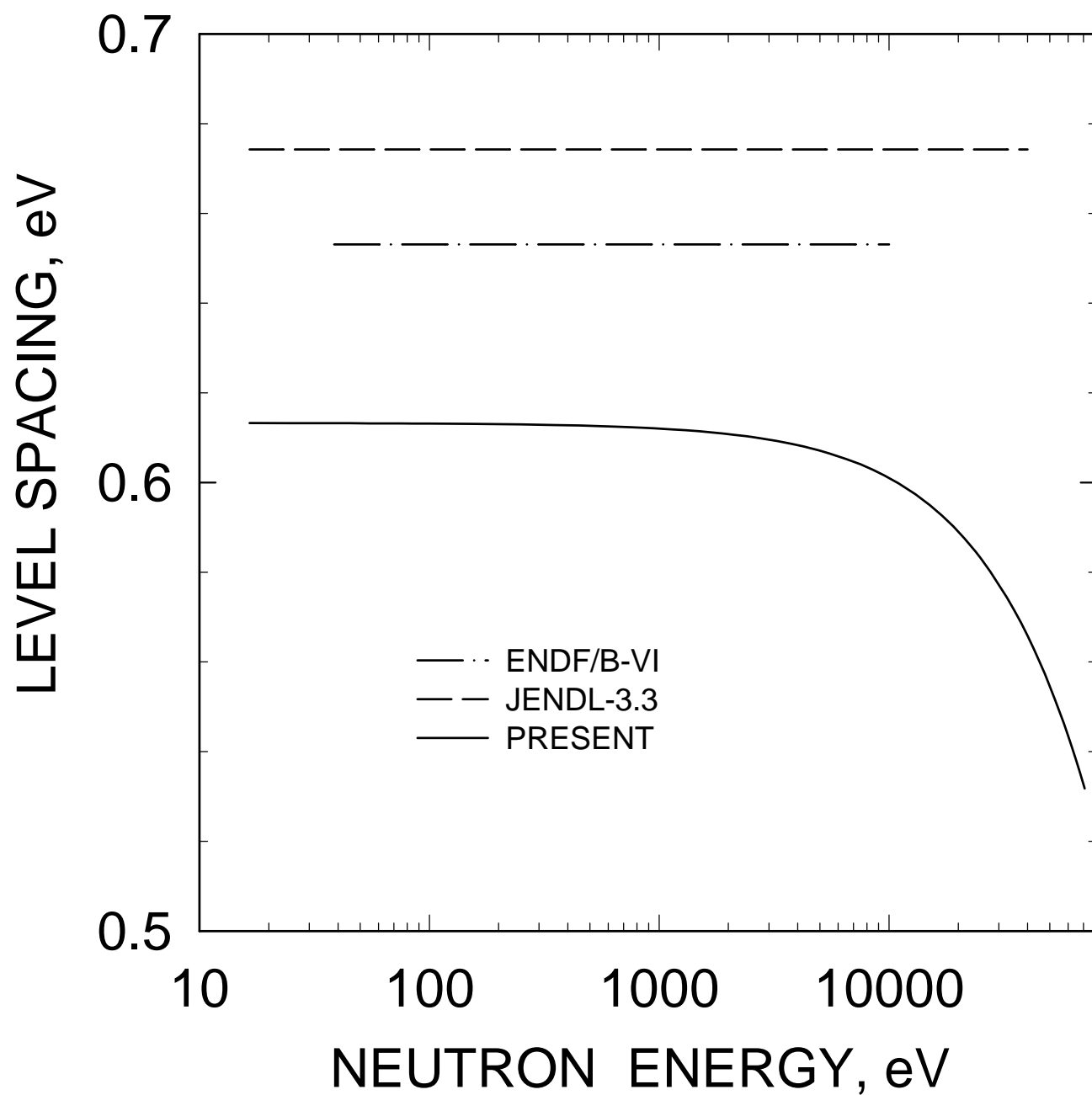


FIG. 14

$^{233}\text{Pa}$ : AVERAGE REDUCED  
NEUTRON WIDTH  
( $L=0$ ,  $J=1$ )

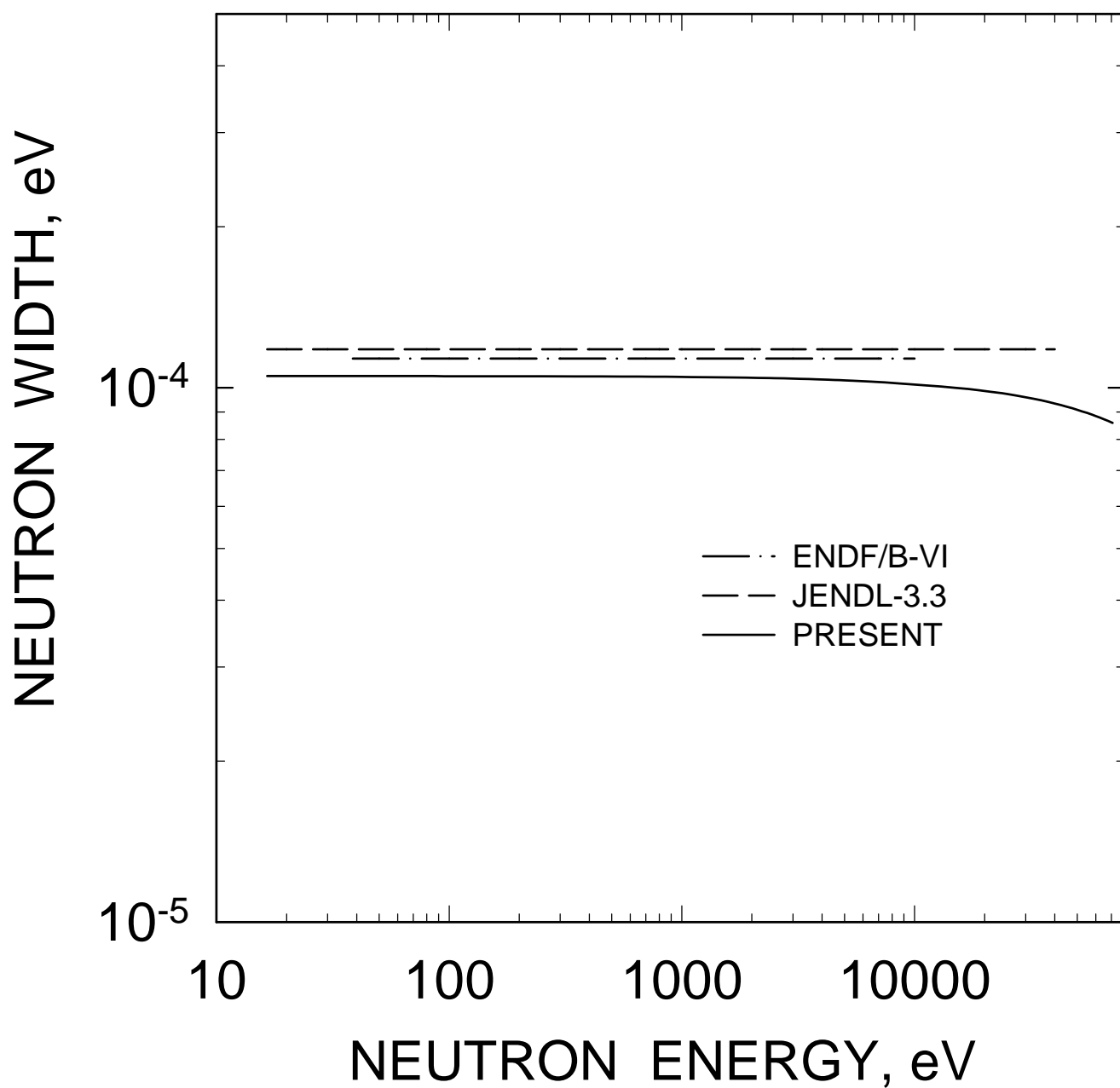


FIG. 15

$^{233}\text{Pa}$ : AVERAGE REDUCED  
NEUTRON WIDTH  
( $L=0$ ,  $J=2$ )

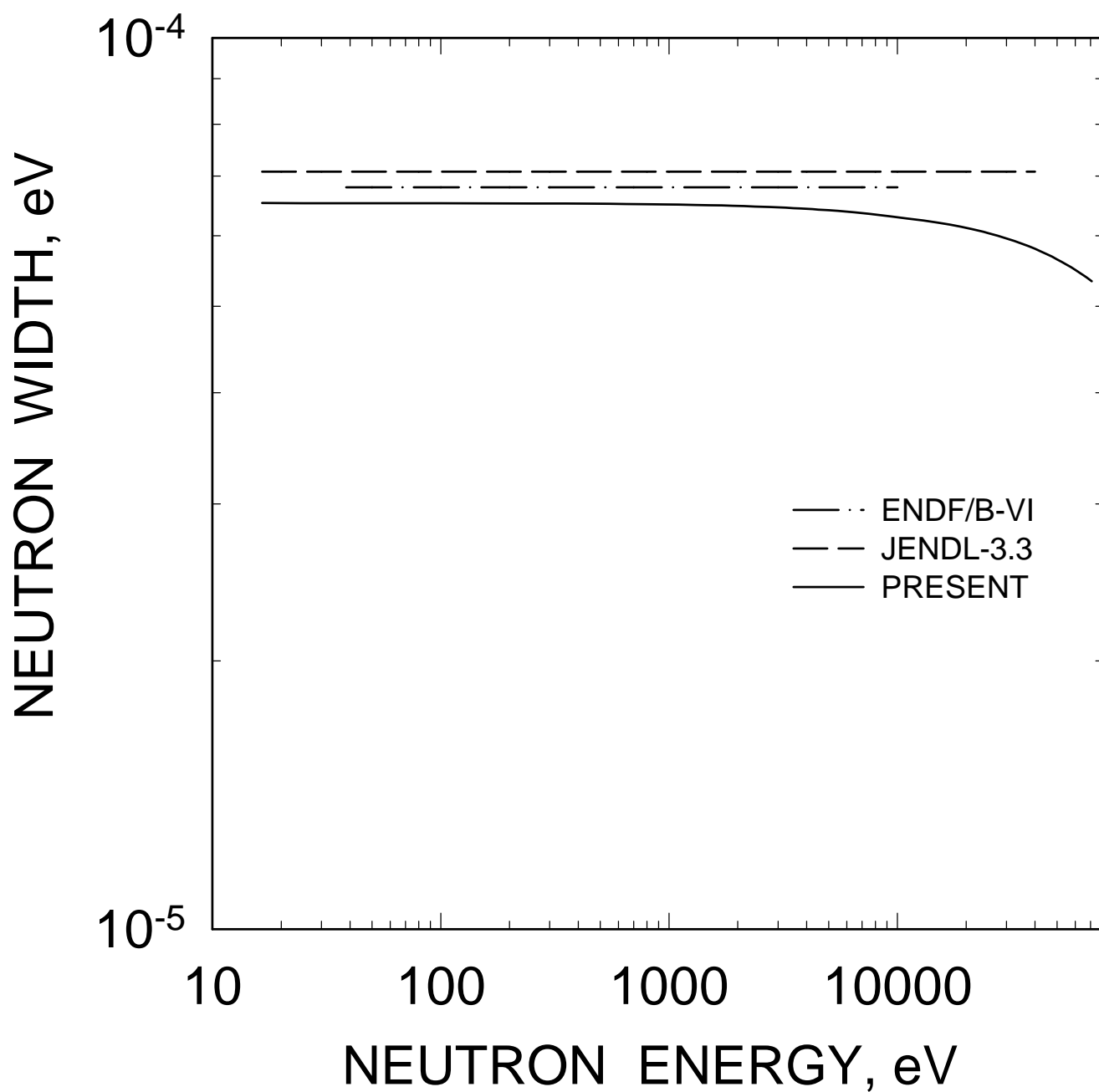


FIG. 16

$^{233}\text{Pa}$ : AVERAGE REDUCED  
NEUTRON WIDTH  
( $L=1, J=0$ )

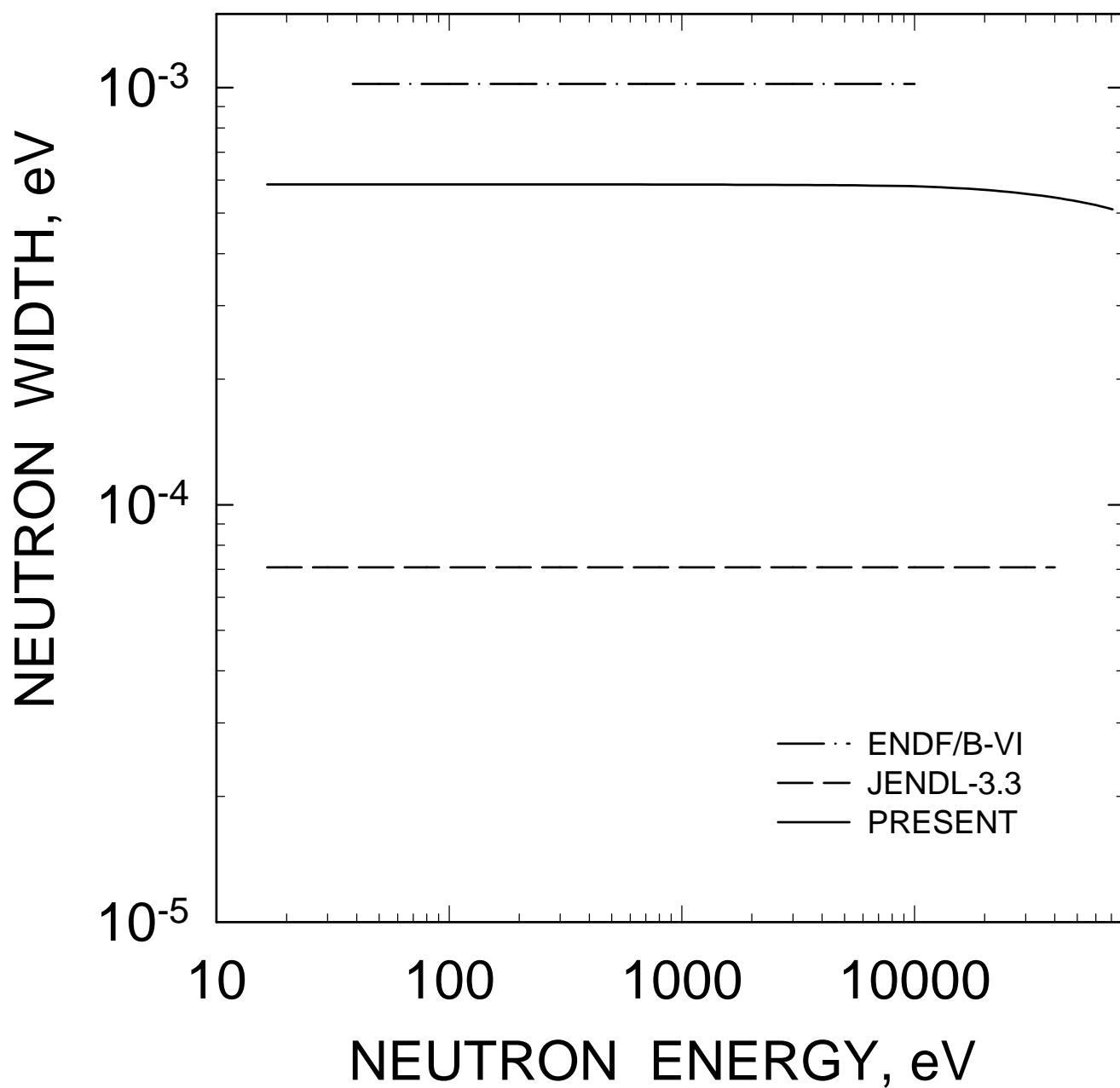


FIG. 17

$^{233}\text{Pa}$ : AVERAGE REDUCED  
NEUTRON WIDTH  
( $L=1, J=1$ )

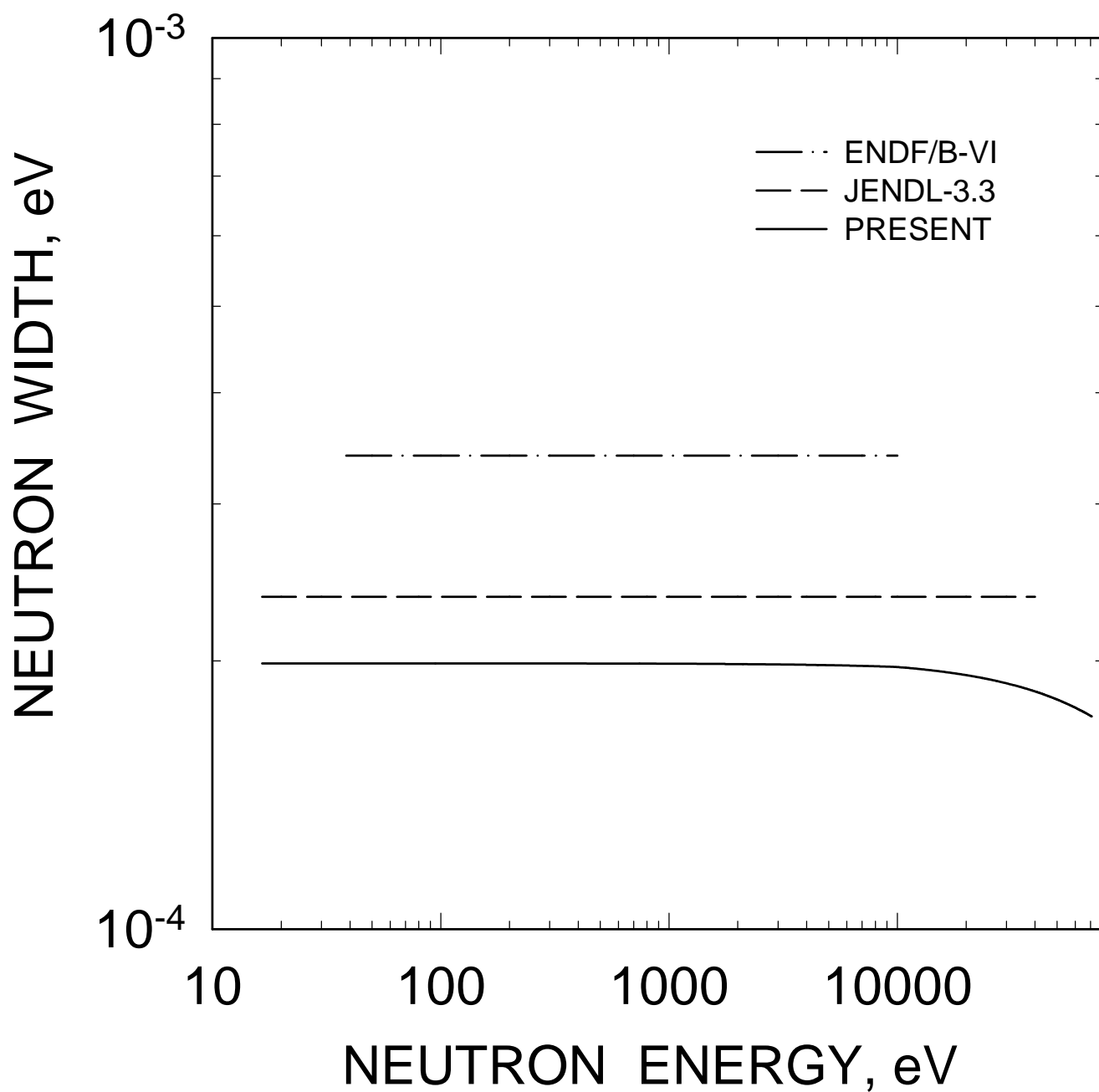


FIG. 18

$^{233}\text{Pa}$ : AVERAGE REDUCED  
NEUTRON WIDTH  
( $L=1, J=2$ )

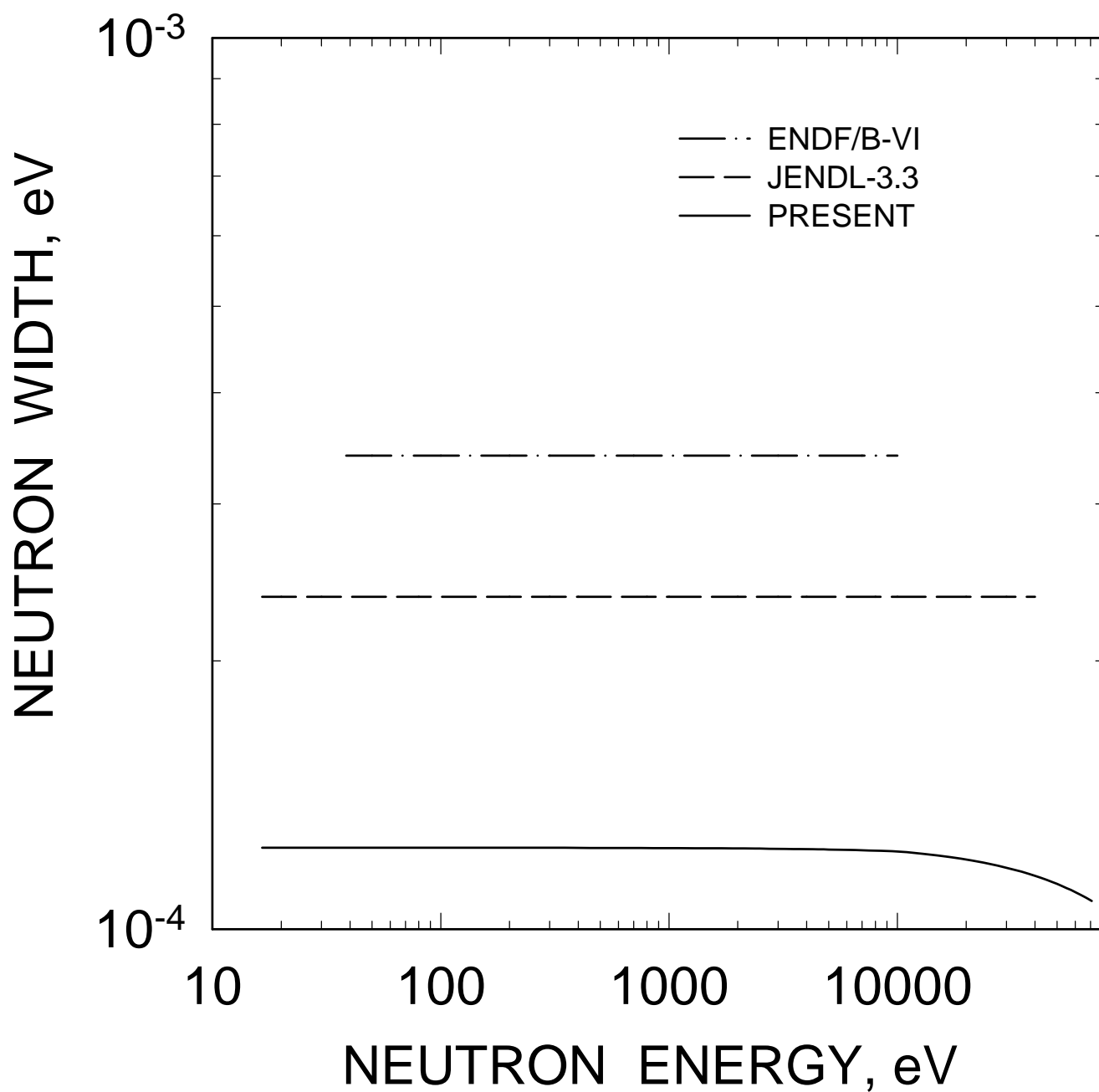


FIG. 19



# $^{233}\text{Pa}$ TOTAL CROSS SECTION

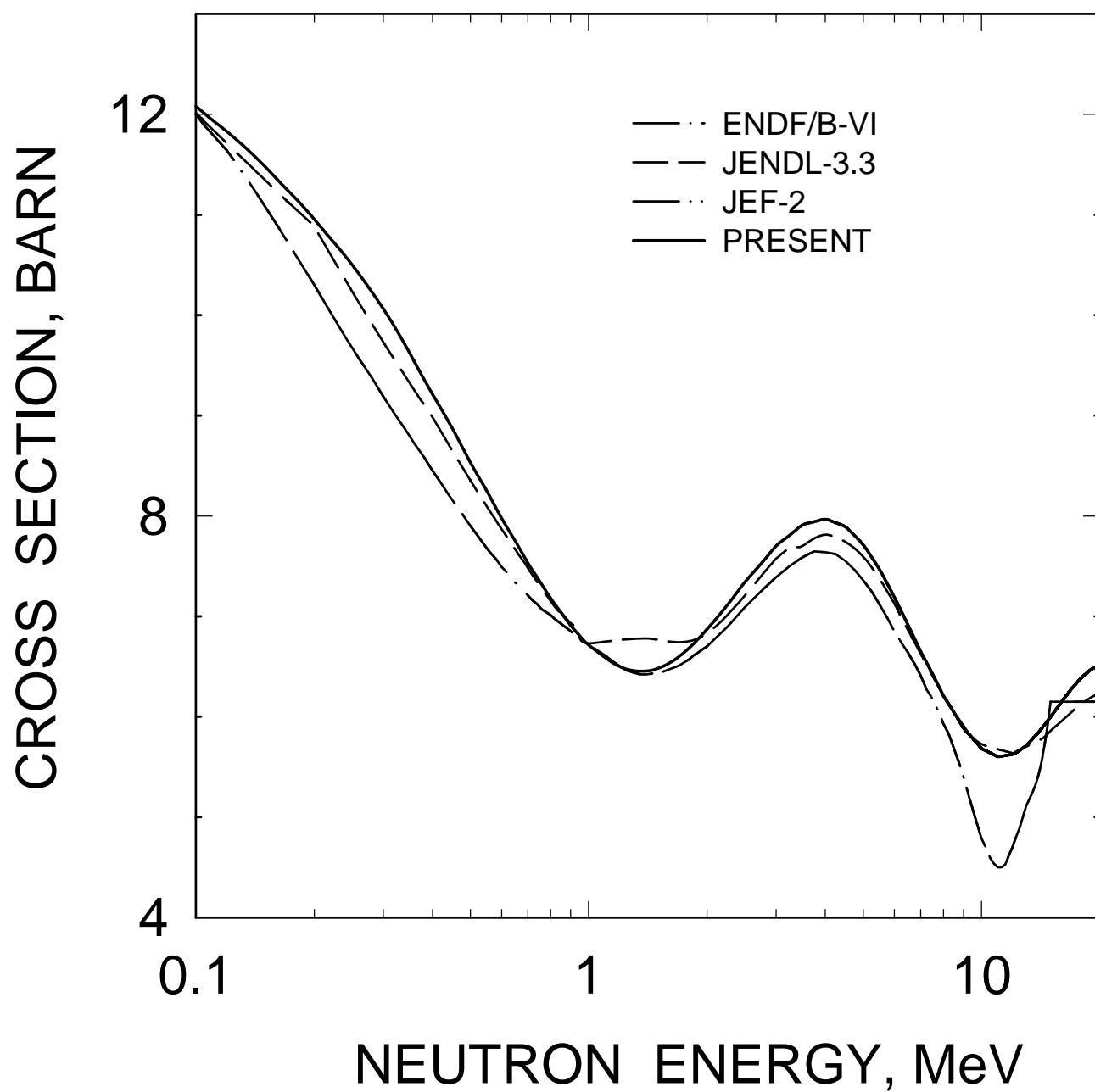


FIG. 20

# $^{233}\text{Pa}$ ELASTIC CROSS SECTION

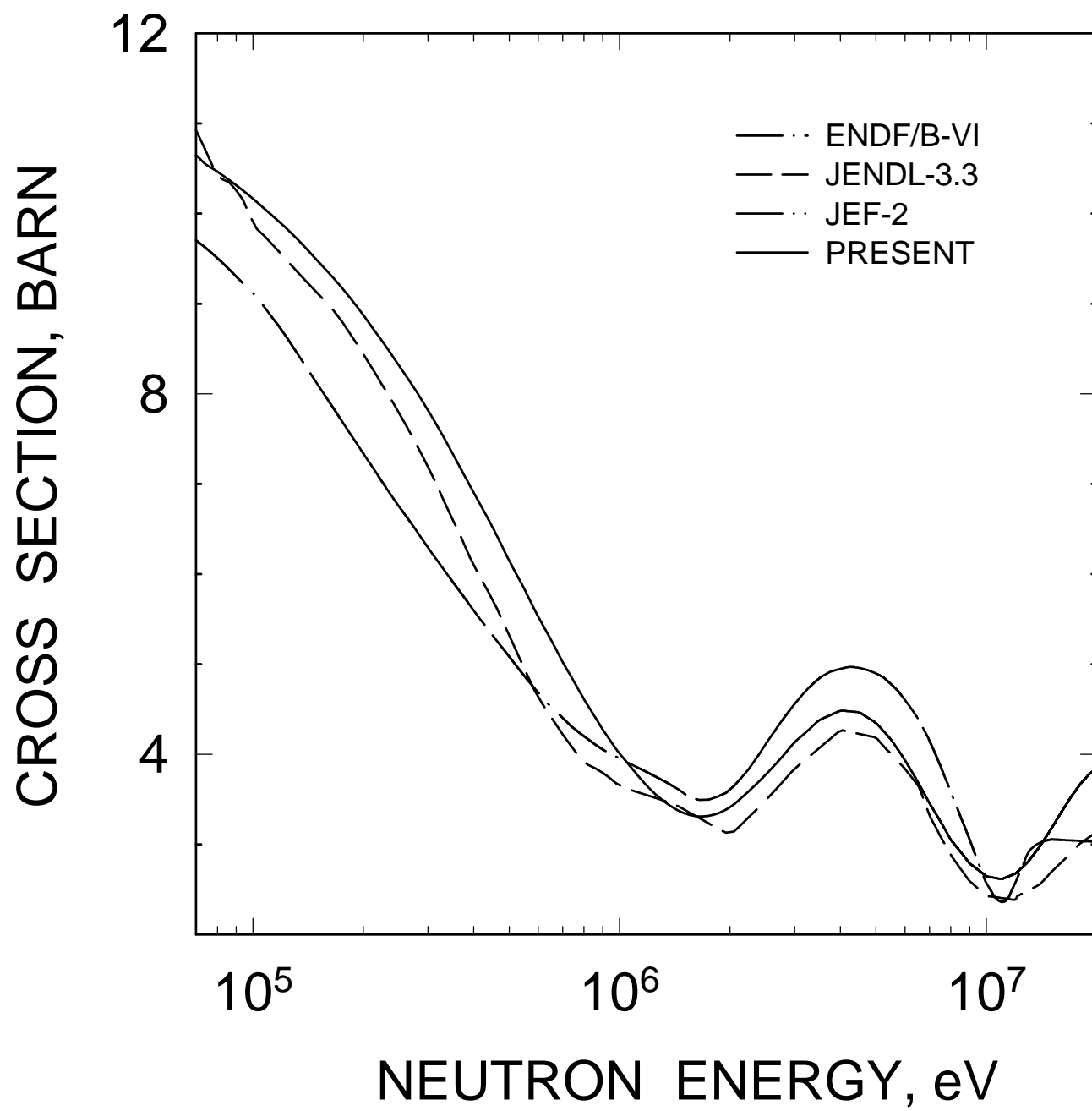


FIG. 21

$^{233}\text{Pa}$

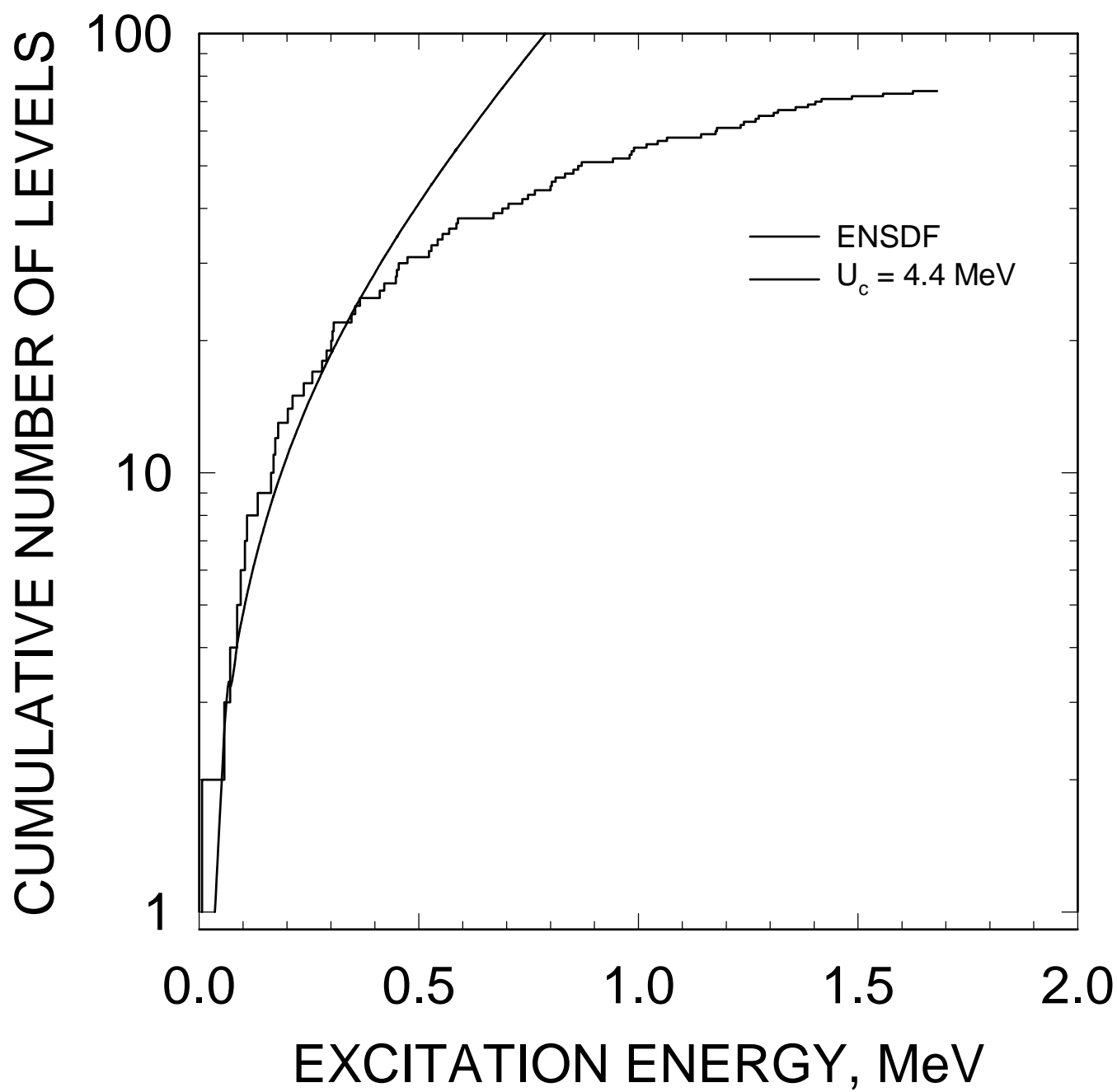


FIG. 22

$^{234}\text{Pa}$

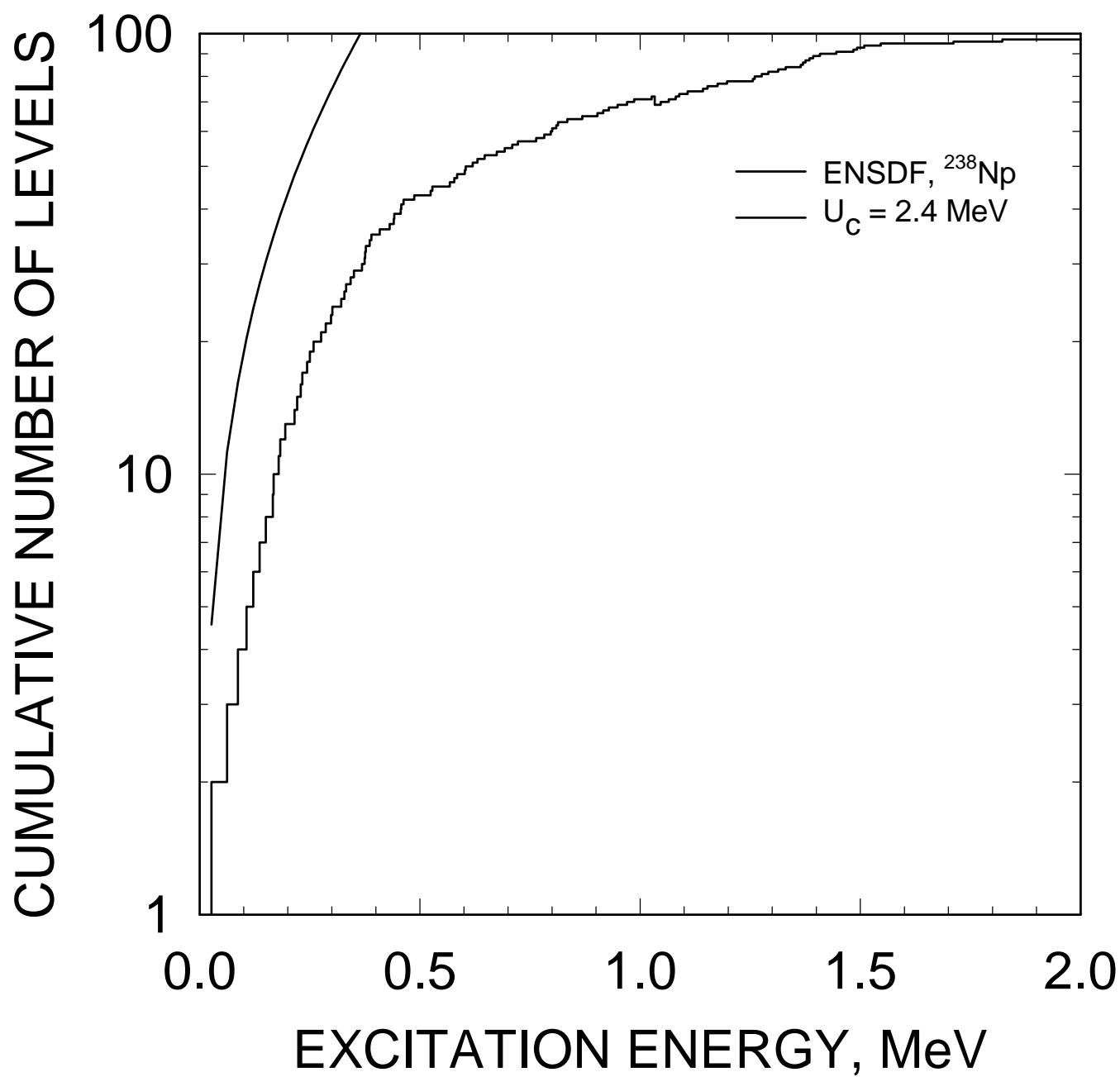


FIG. 23

$^{233}\text{Pa}$

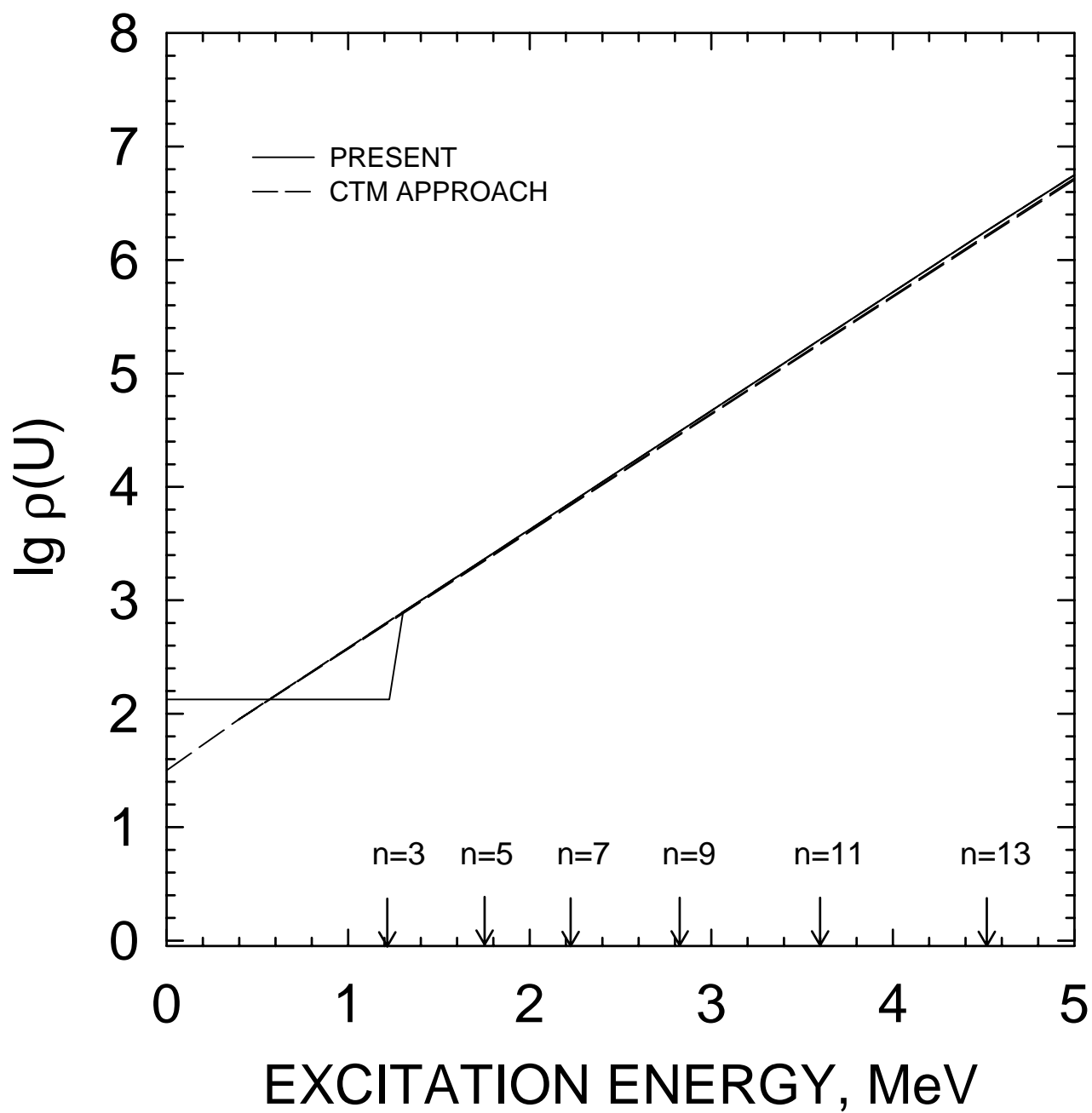


FIG. 24

# $^{233}\text{Pa}$ FISSION CROSS SECTION

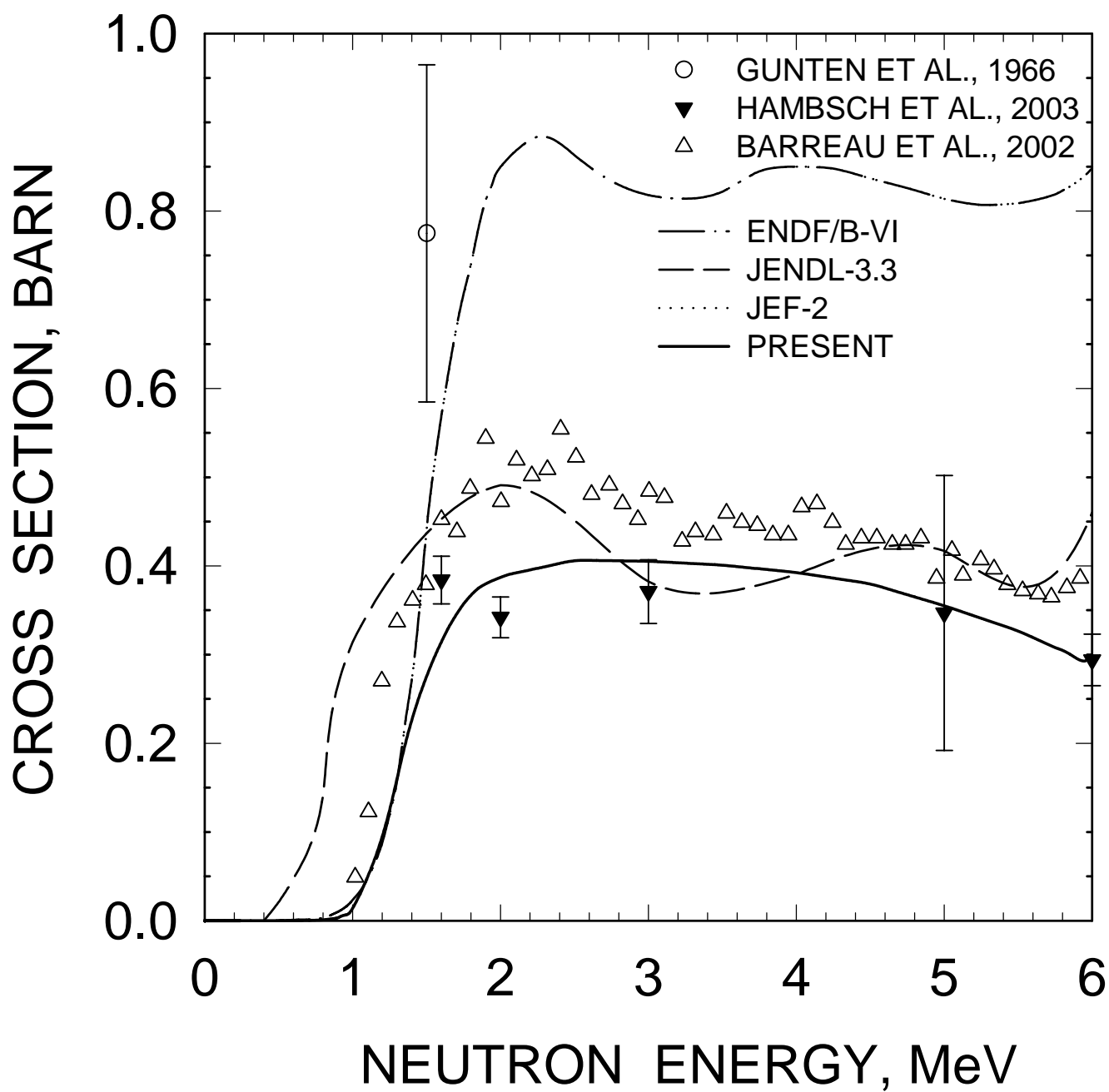


FIG. 25

# $^{233}\text{Pa}$ FISSION CROSS SECTION

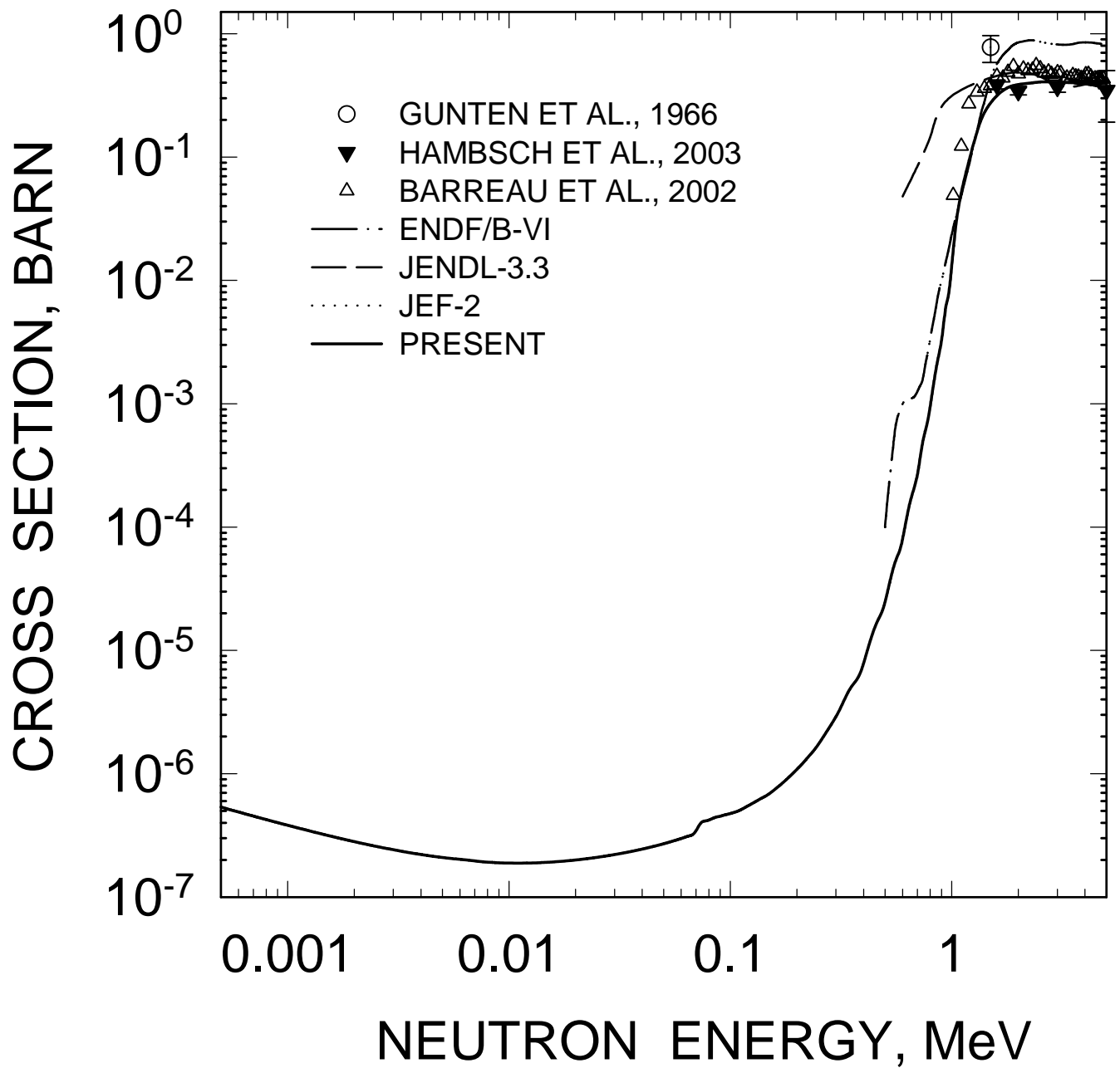


FIG. 26

$^{233}\text{Pa}$ : 0.0067,  $1/2^-$  LEVEL EXCITATION

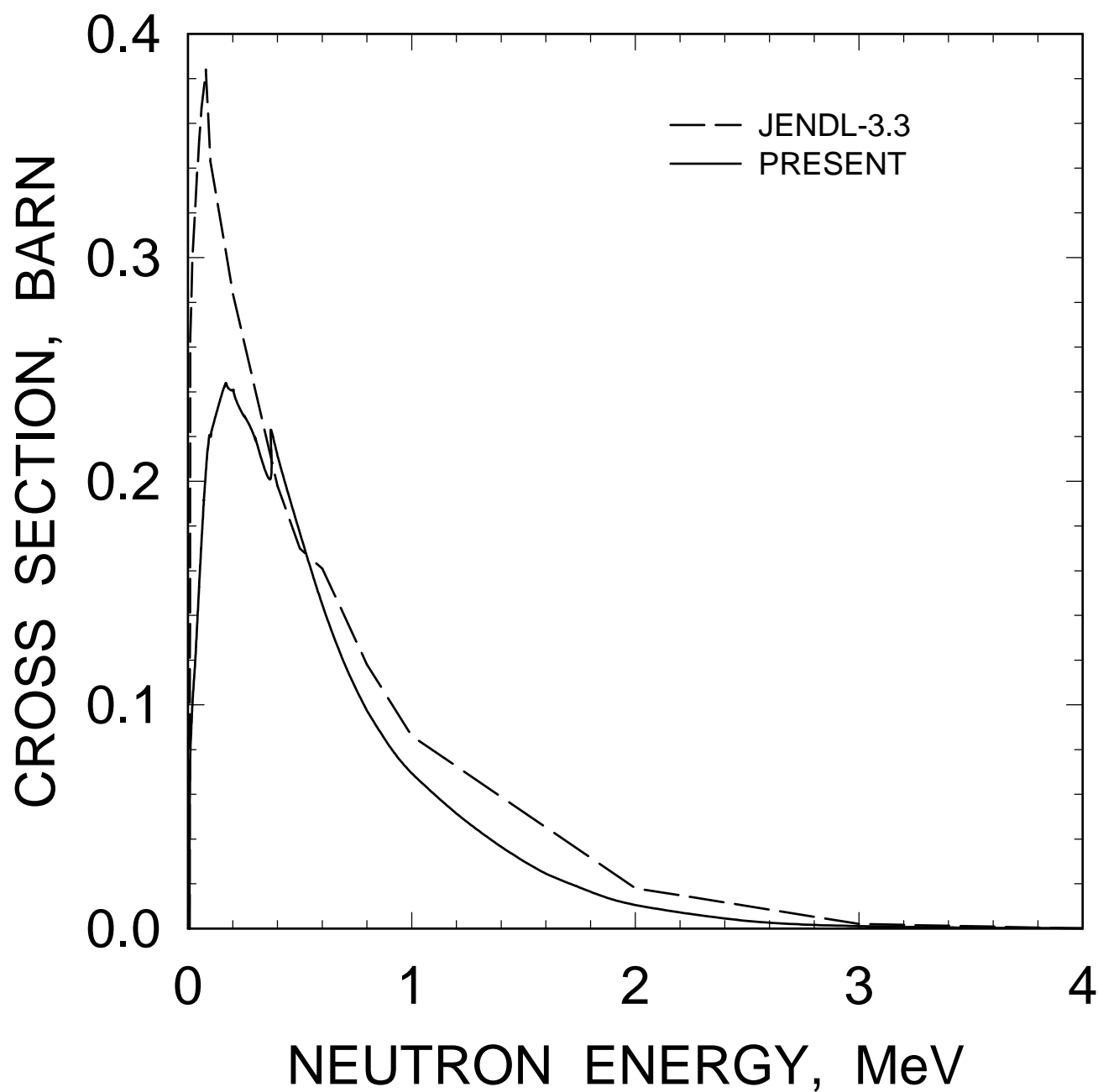


FIG. 27



$^{233}\text{Pa}$ : 0.0572,  $7/2^-$  LEVEL EXCITATION

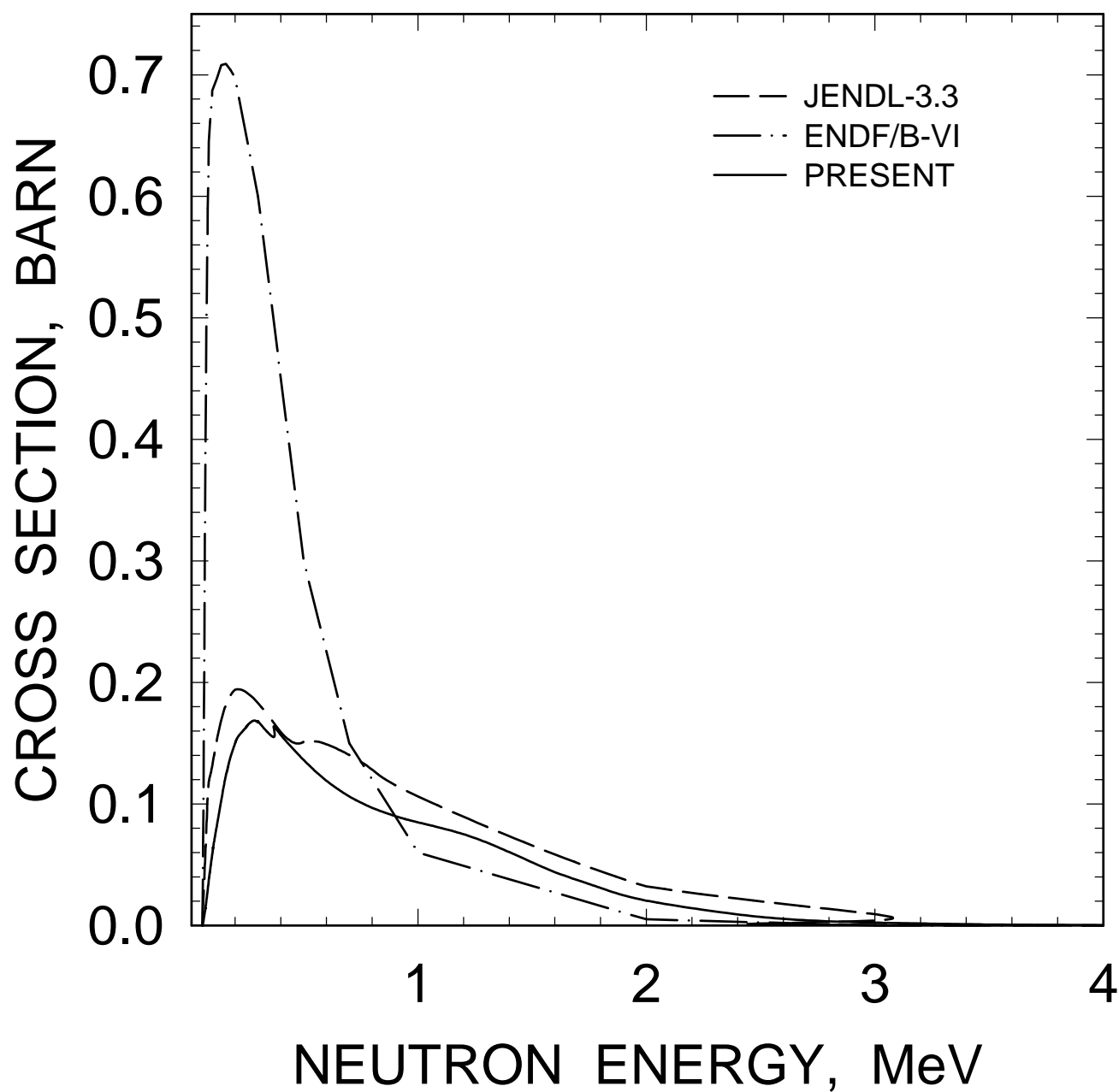


FIG. 28

$^{233}\text{Pa}$ : 0.0706,  $5/2^-$  LEVEL EXCITATION

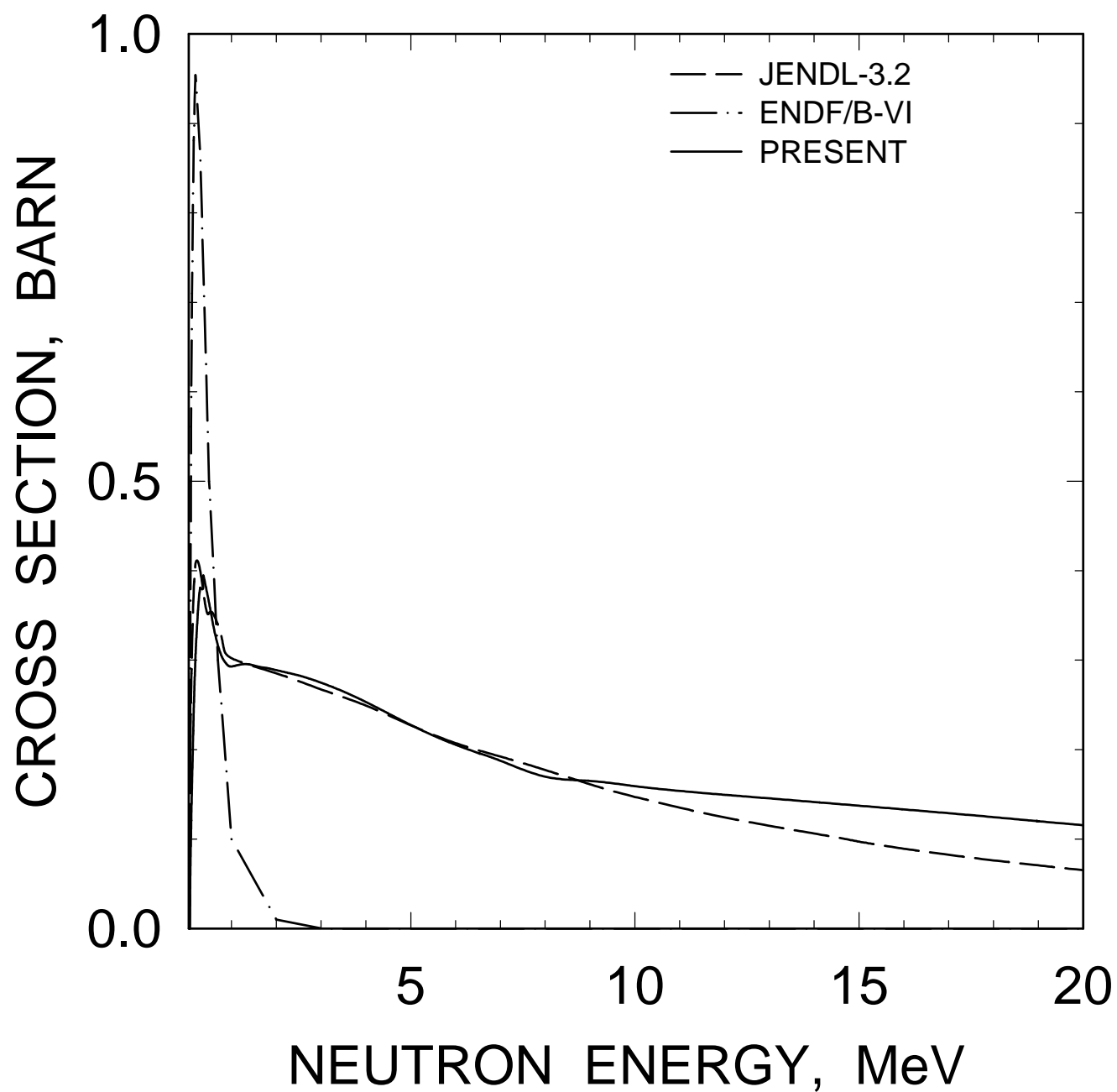


FIG. 29

$^{233}\text{Pa}$ : 0.0865,  $5/2^+$  LEVEL EXCITATION

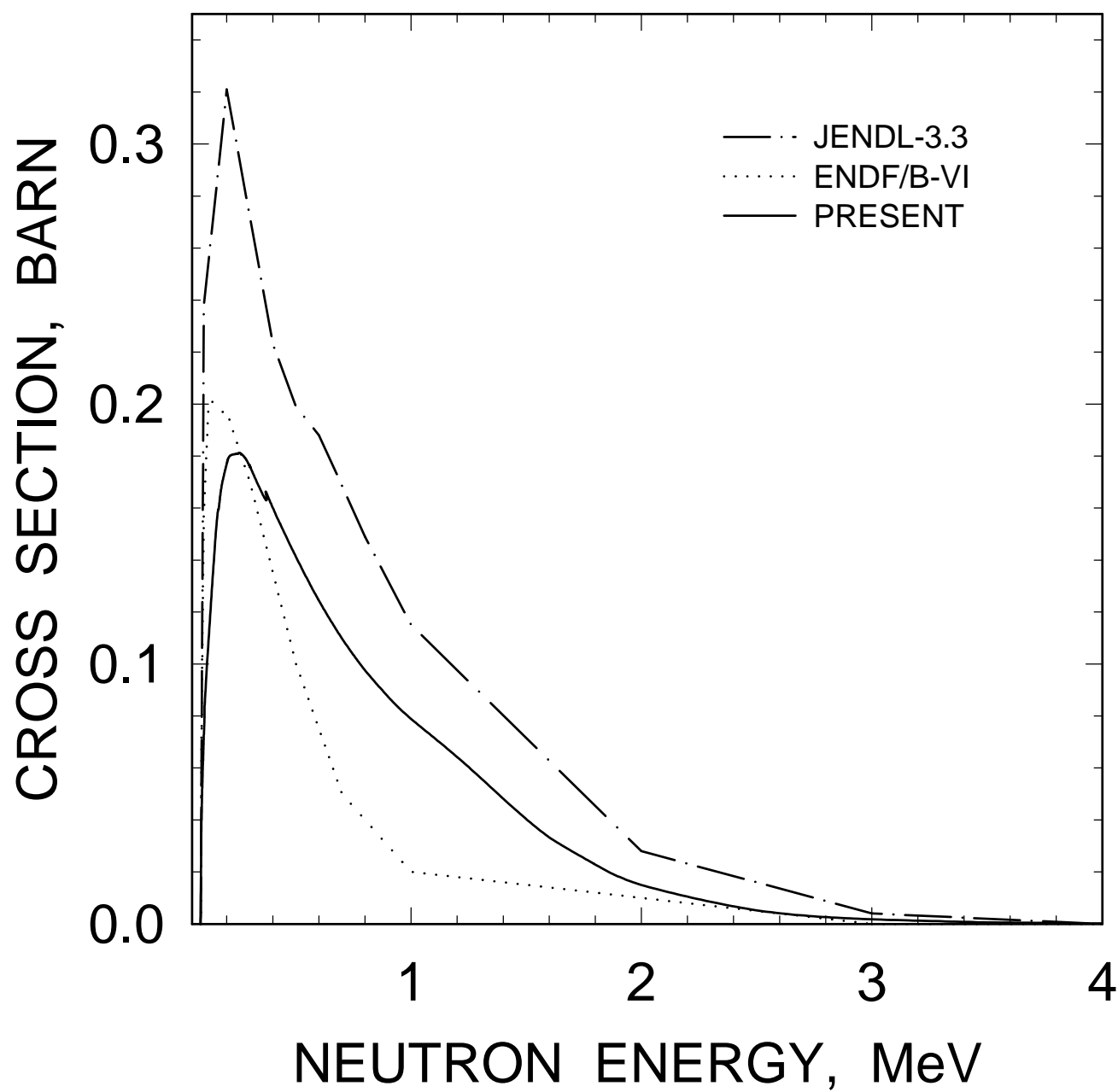


FIG. 30

$^{233}\text{Pa}$ : 0.0947,  $3/2^+$  LEVEL EXCITATION

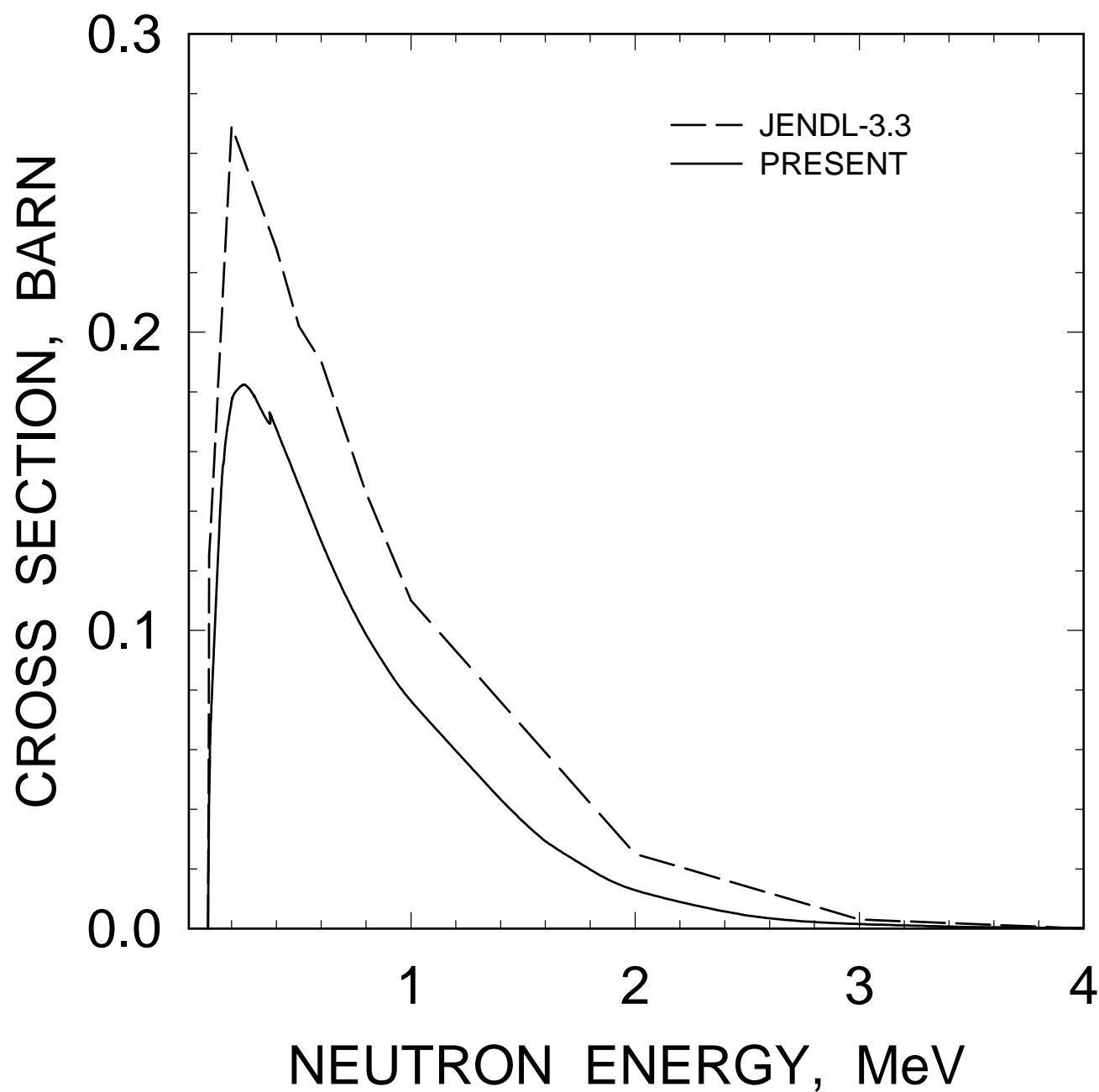


FIG. 31

$^{233}\text{Pa}$ : 0.1036,  $7/2^+$  LEVEL EXCITATION

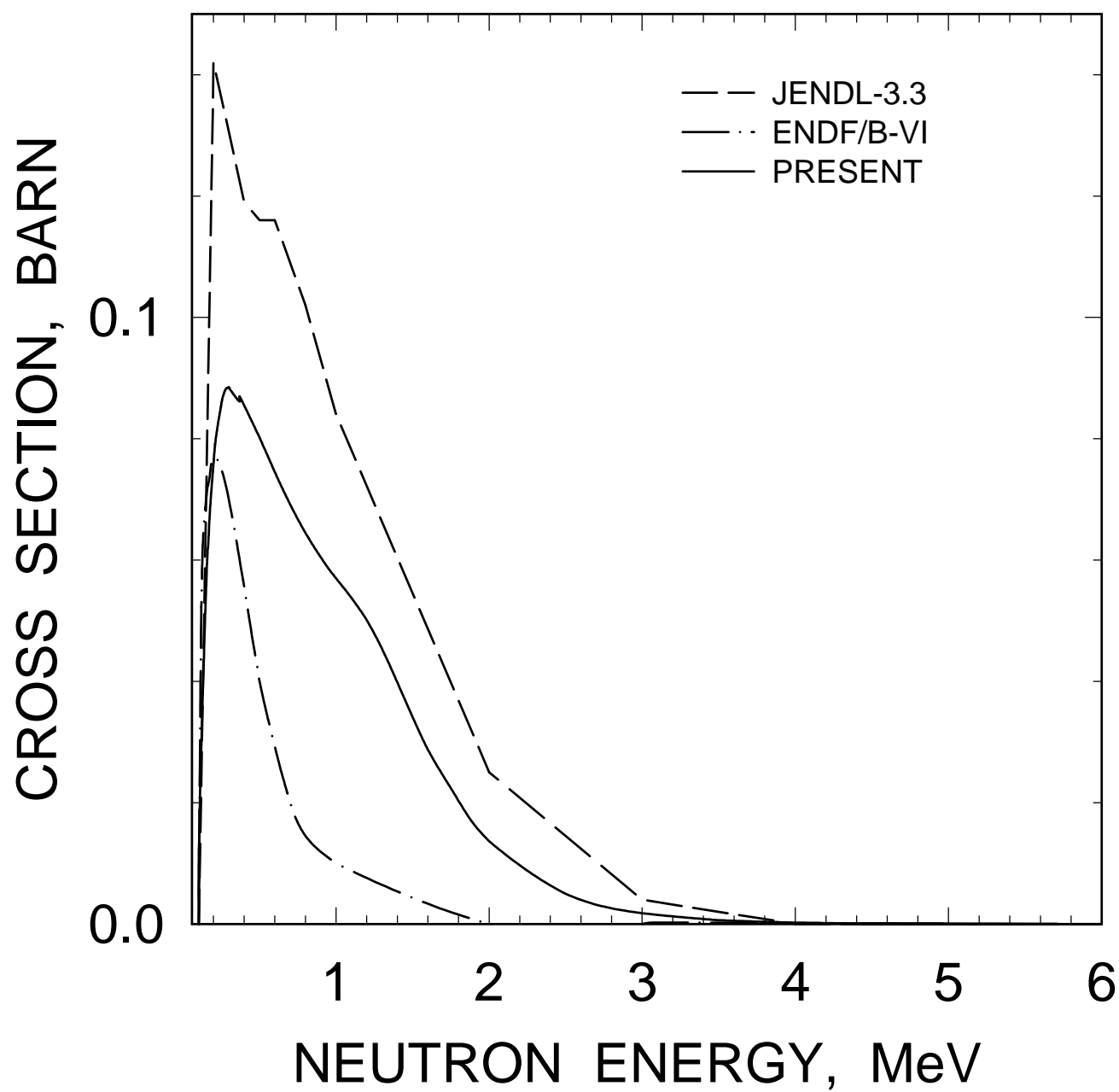


FIG. 32

$^{233}\text{Pa}$ : 0.1090,  $9/2^+$  LEVEL EXCITATION

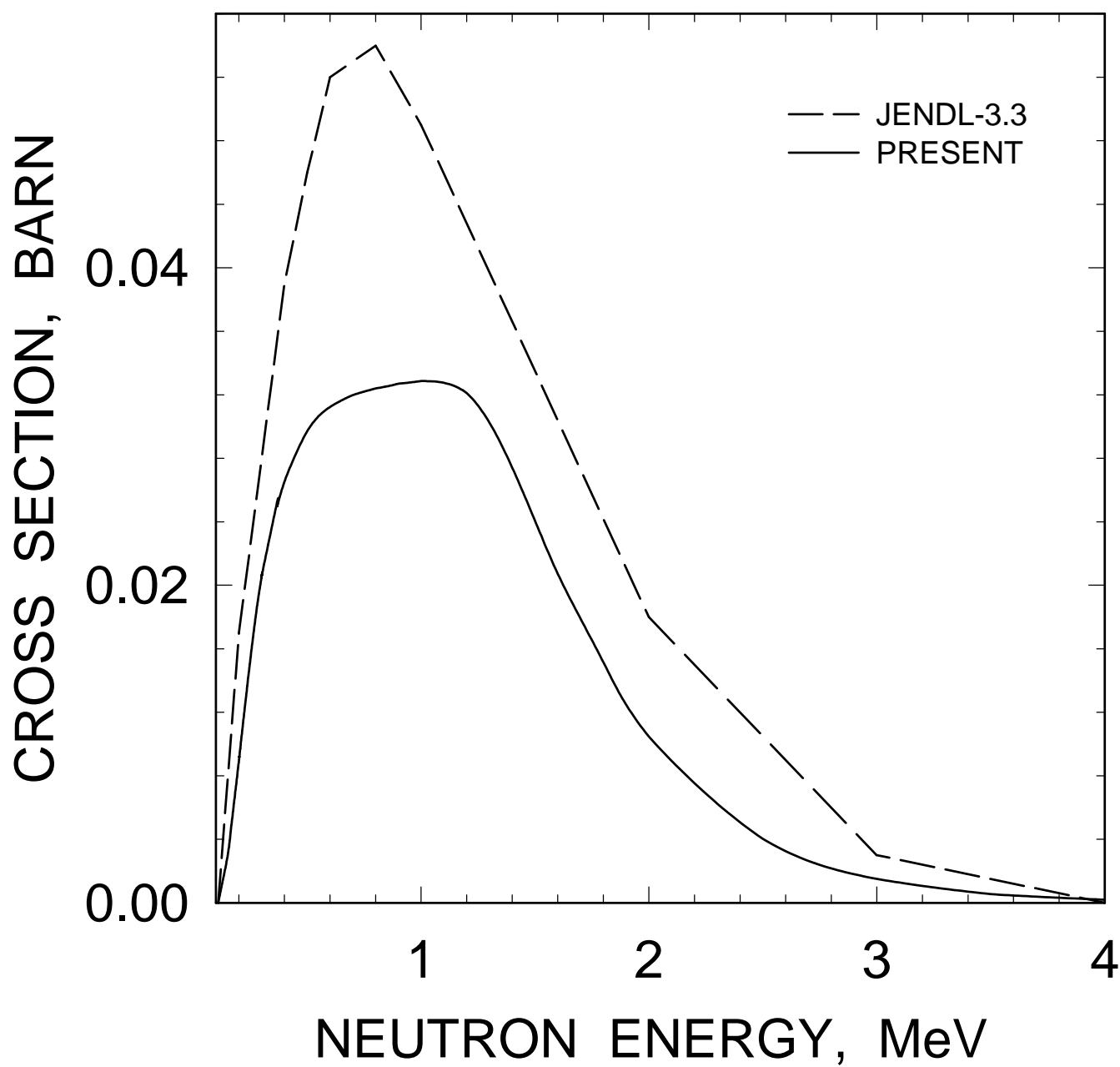


FIG. 33

$^{233}\text{Pa}$ : 0.1634,  $11/2^+$  LEVEL EXCITATION

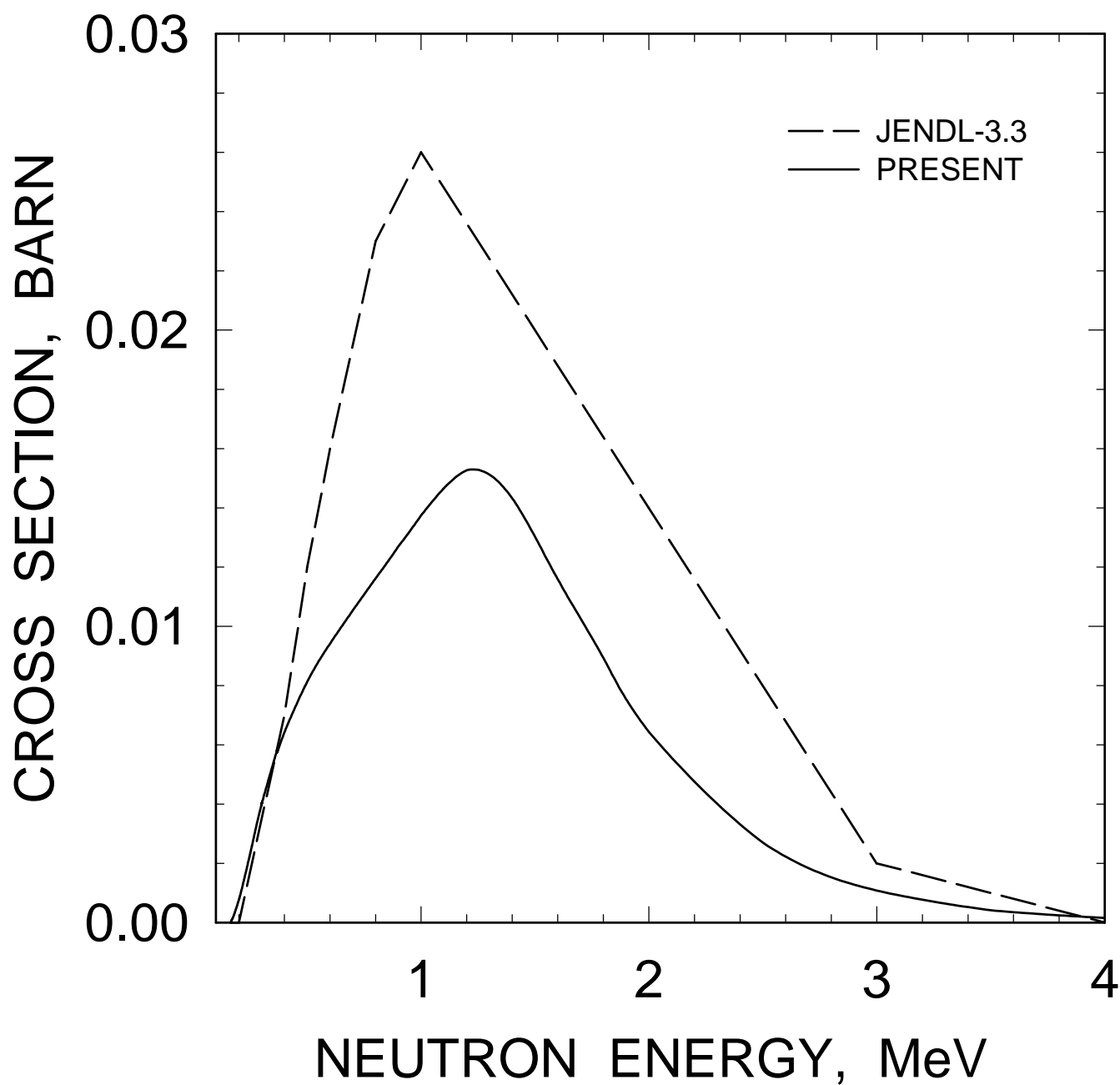


FIG. 34

$^{233}\text{Pa}$ : 0.1691,  $1/2^+$  LEVEL EXCITATION

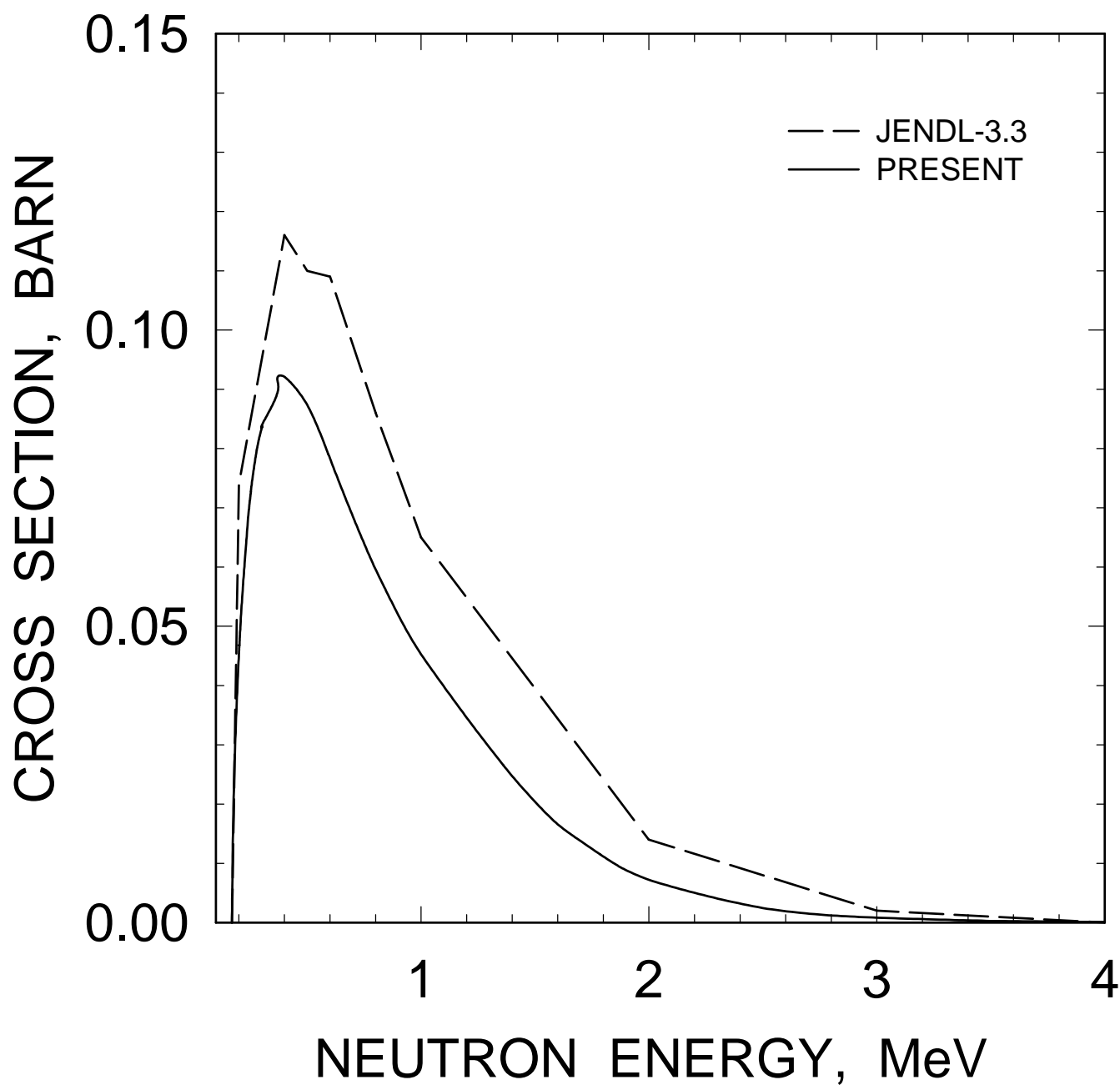


FIG. 35



$^{233}\text{Pa}$ : 0.1792,  $9/2^-$  LEVEL EXCITATION

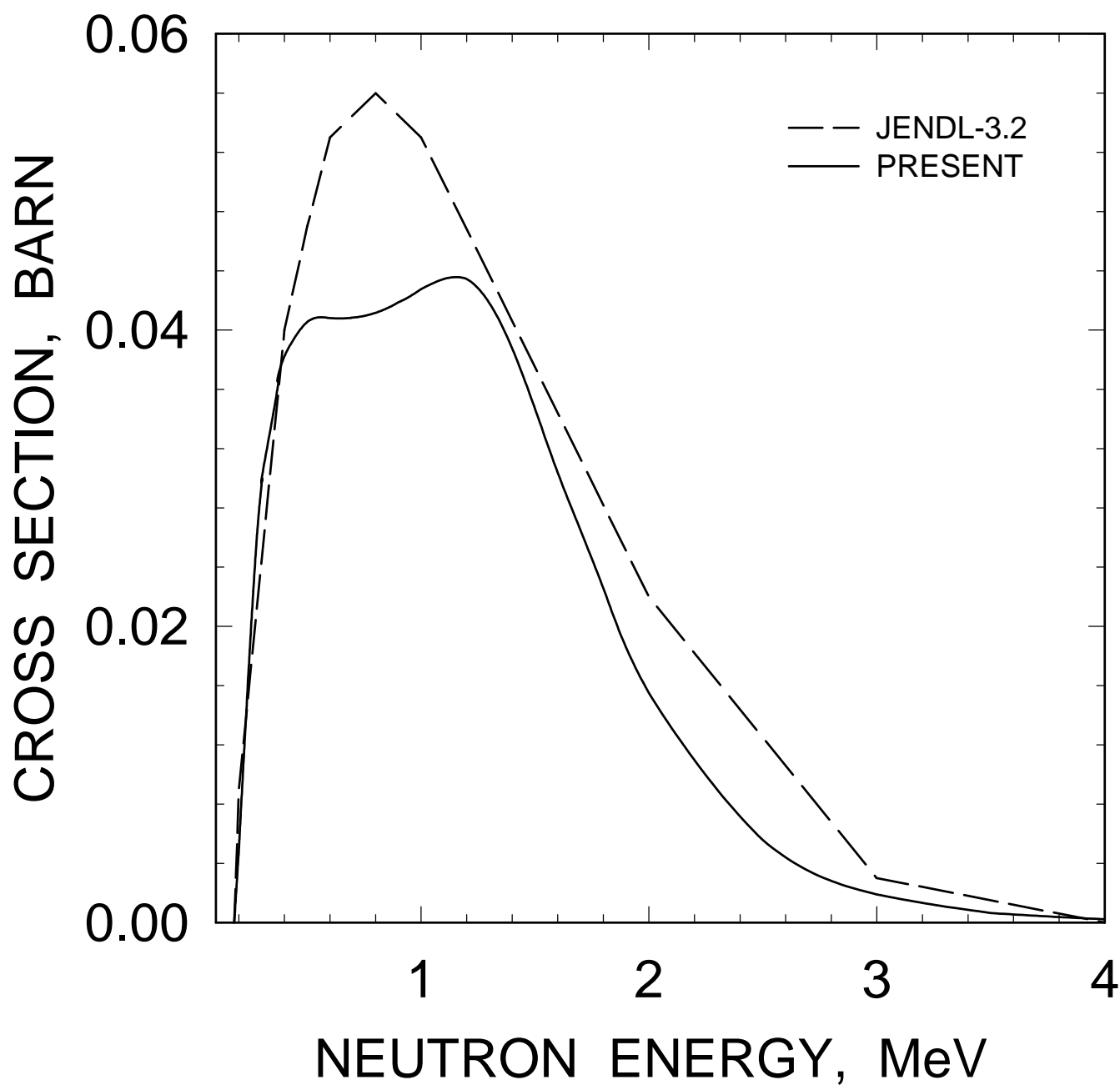


FIG. 36

$^{233}\text{Pa}$ : 0.2017,  $3/2^+$  LEVEL EXCITATION

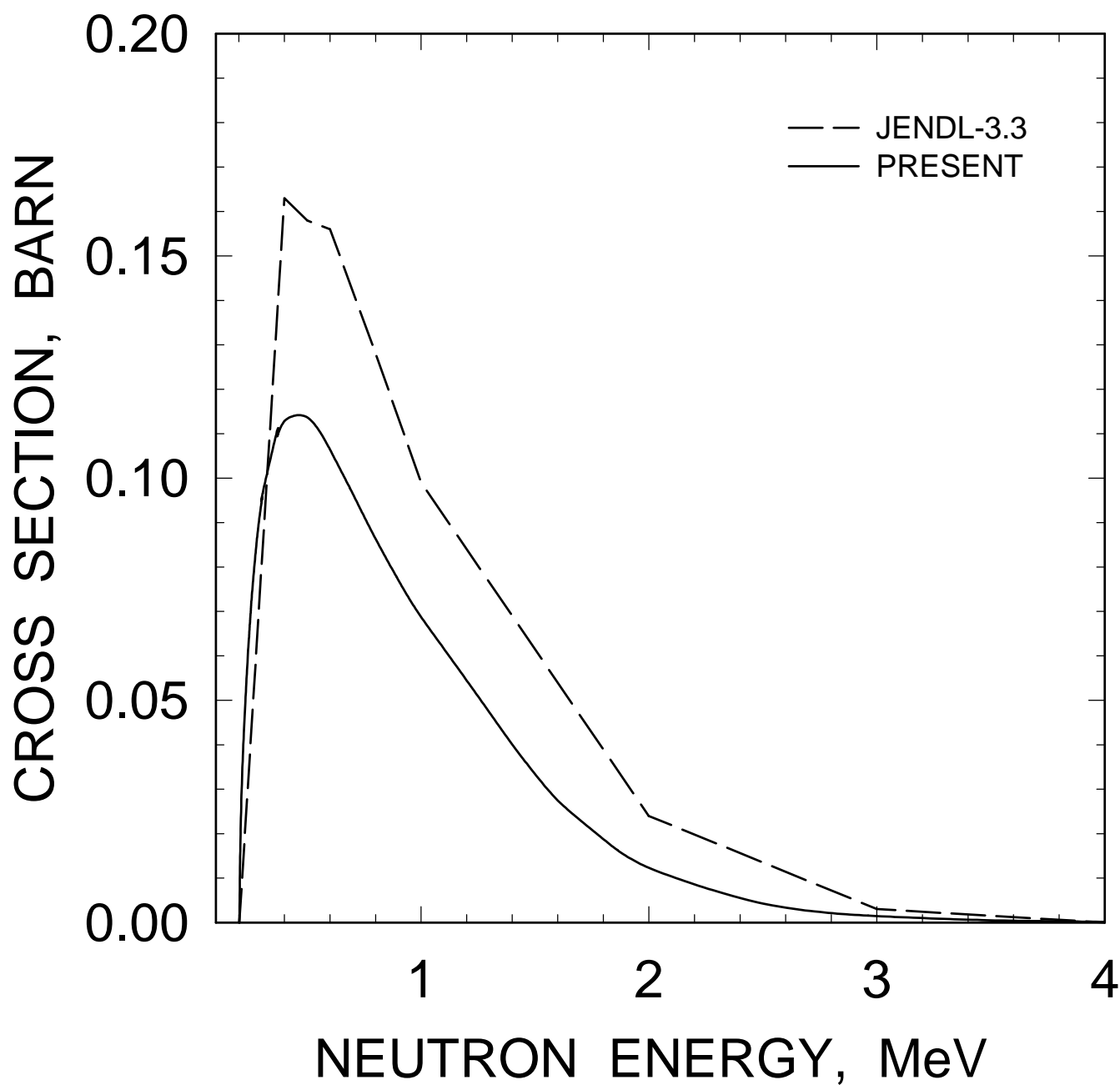


FIG. 37

$^{233}\text{Pa}$ : 0.2123,  $5/2^+$  LEVEL EXCITATION

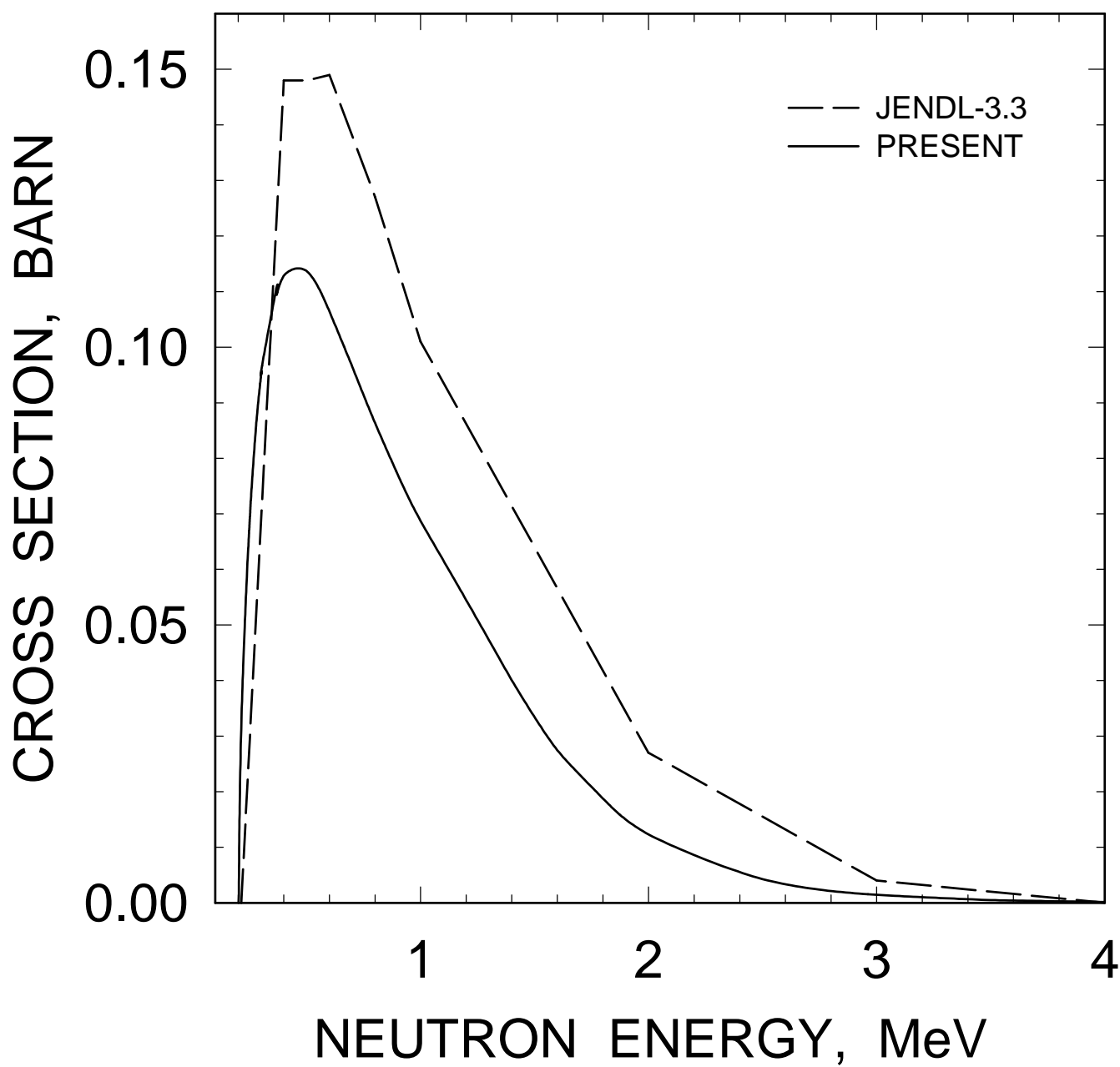


FIG. 38

$^{233}\text{Pa}$ : 0.2379,  $9/2^+$  LEVEL EXCITATION

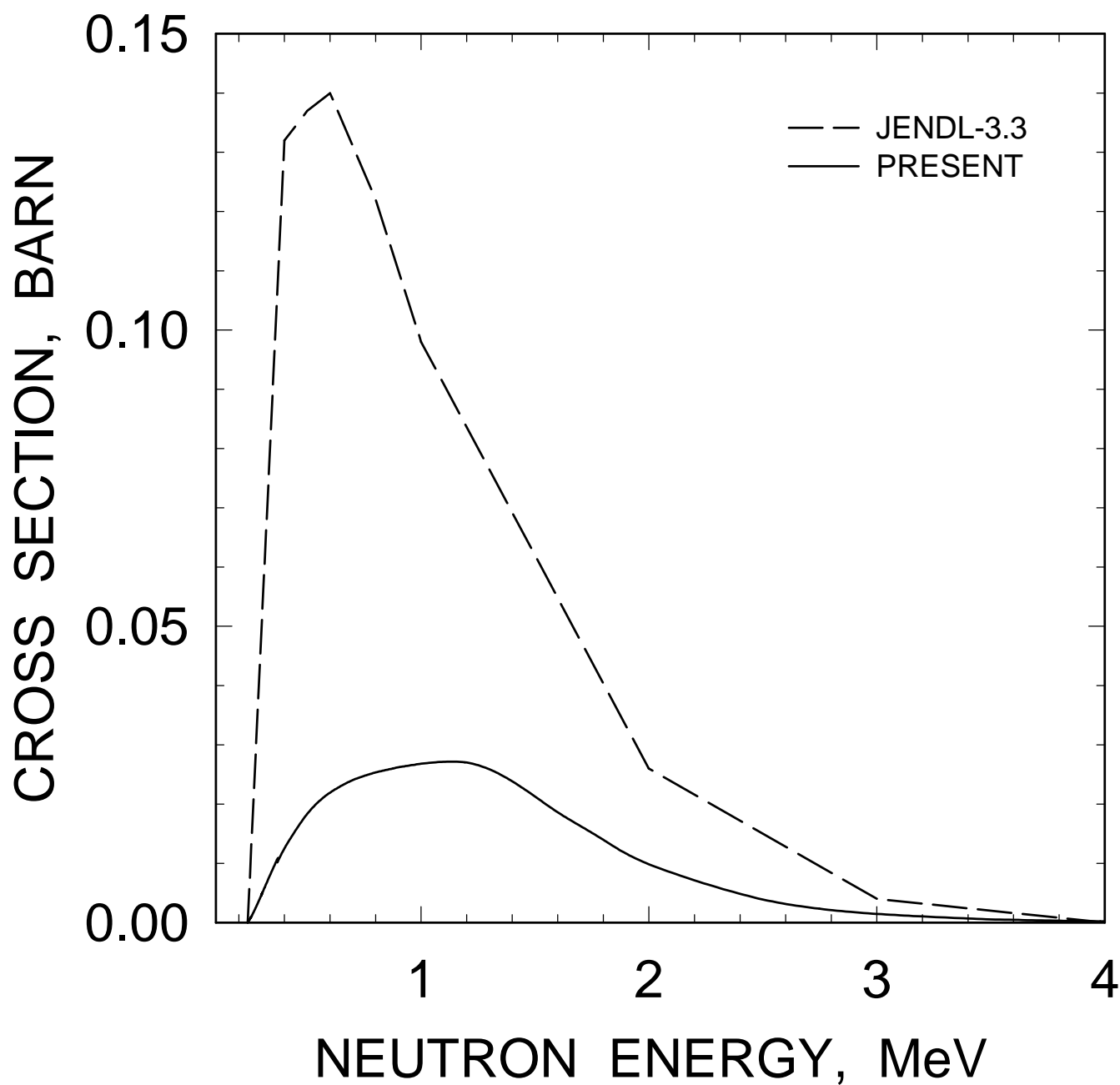


FIG. 39

$^{233}\text{Pa}$ : 0.2573,  $5/2^-$  LEVEL EXCITATION

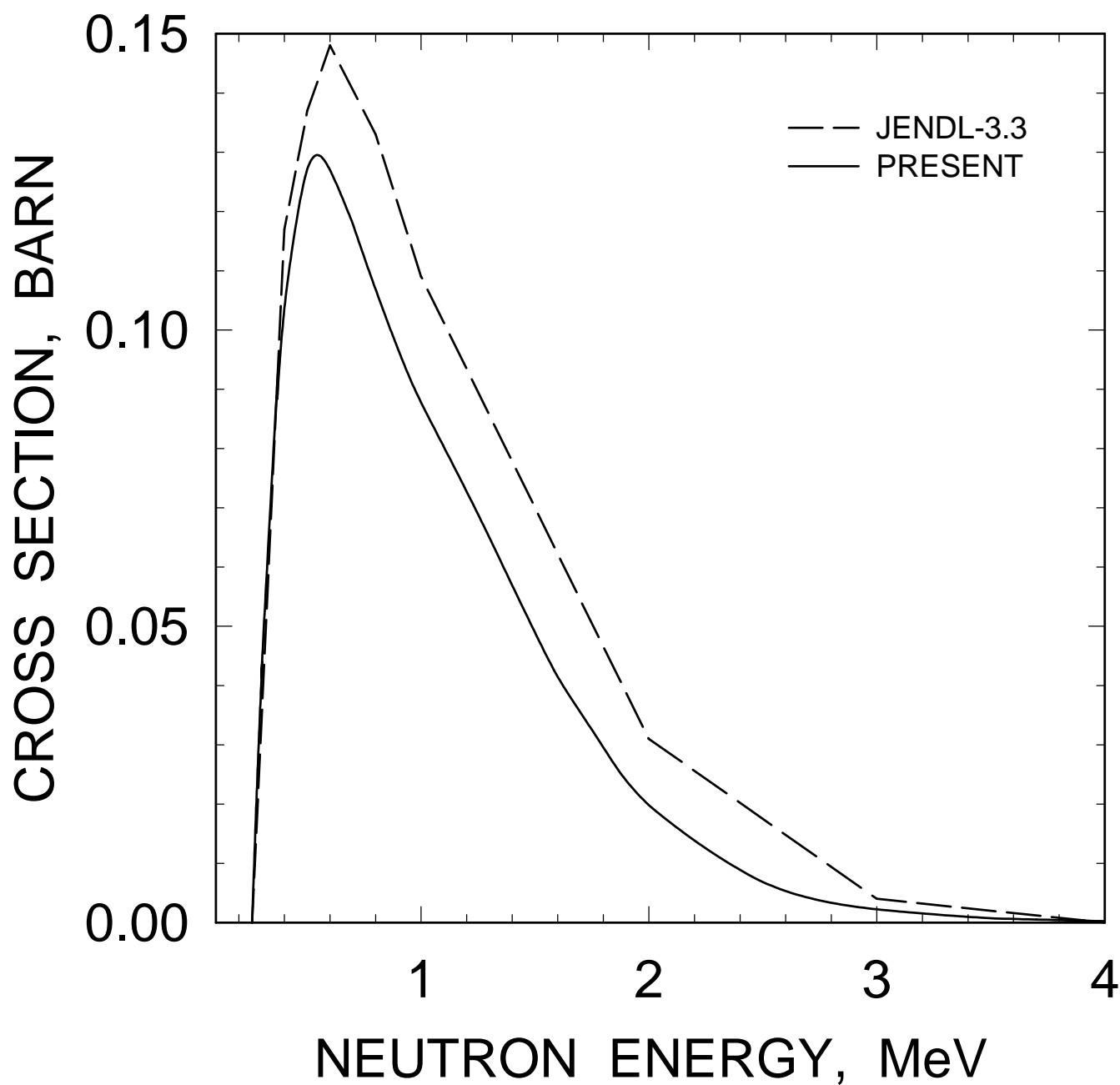


FIG. 40

$^{233}\text{Pa}$ : 0.2796,  $7/2^+$  LEVEL EXCITATION

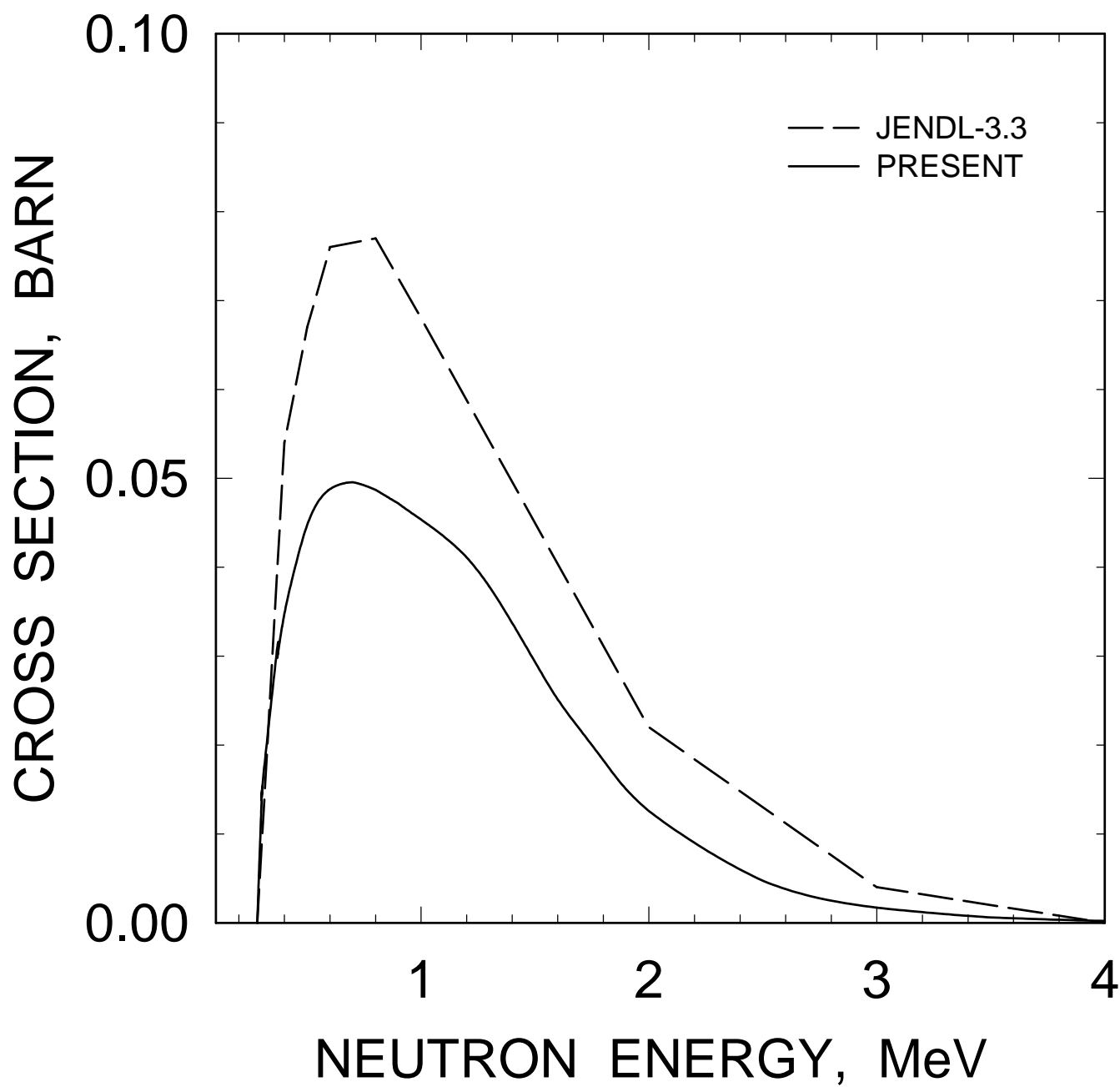


FIG. 41

$^{233}\text{Pa}$ : 0.3004,  $7/2^-$  LEVEL EXCITATION

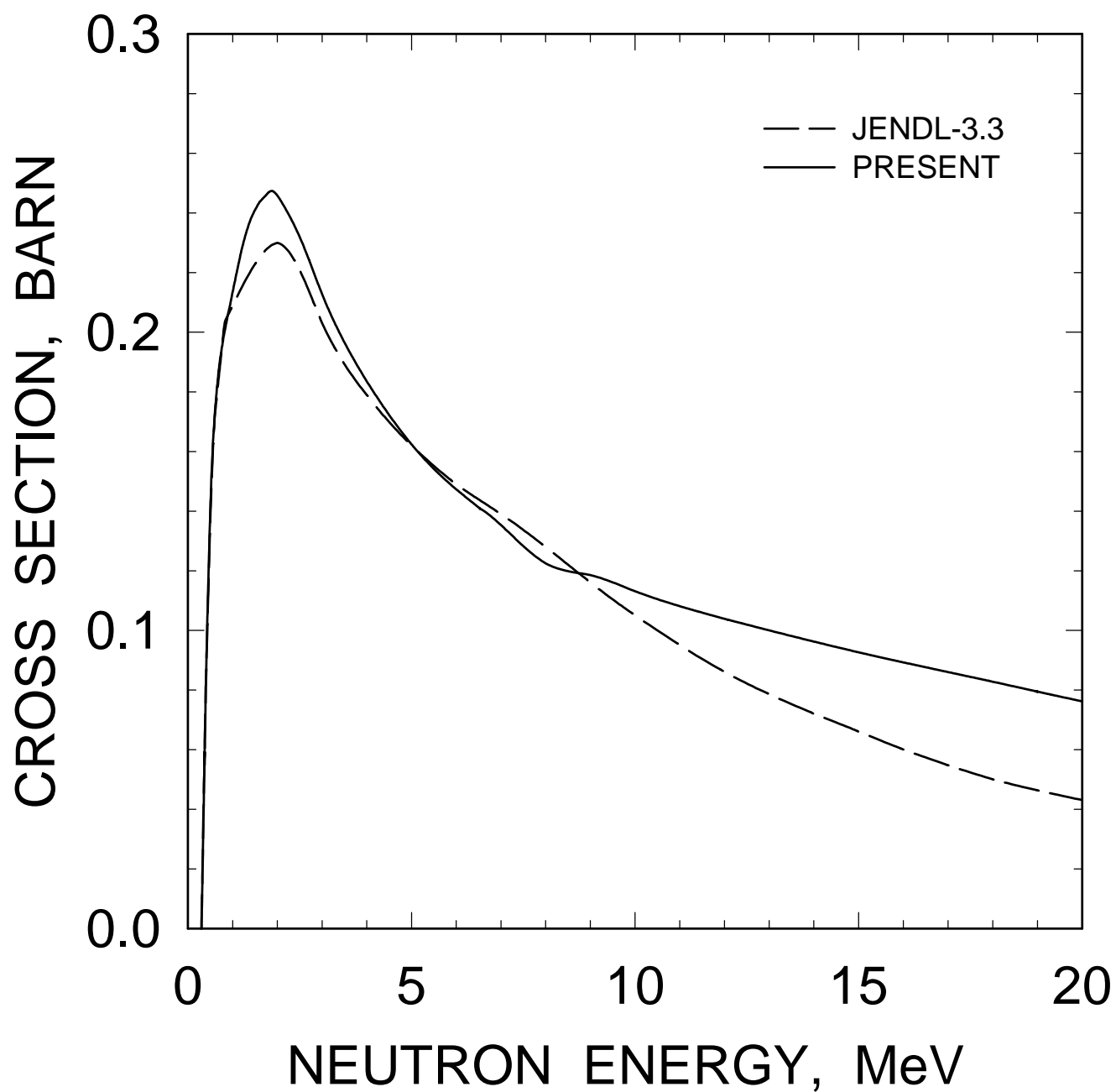


FIG. 42

$^{233}\text{Pa}$ : 0.3061,  $7/2^+$  LEVEL EXCITATION

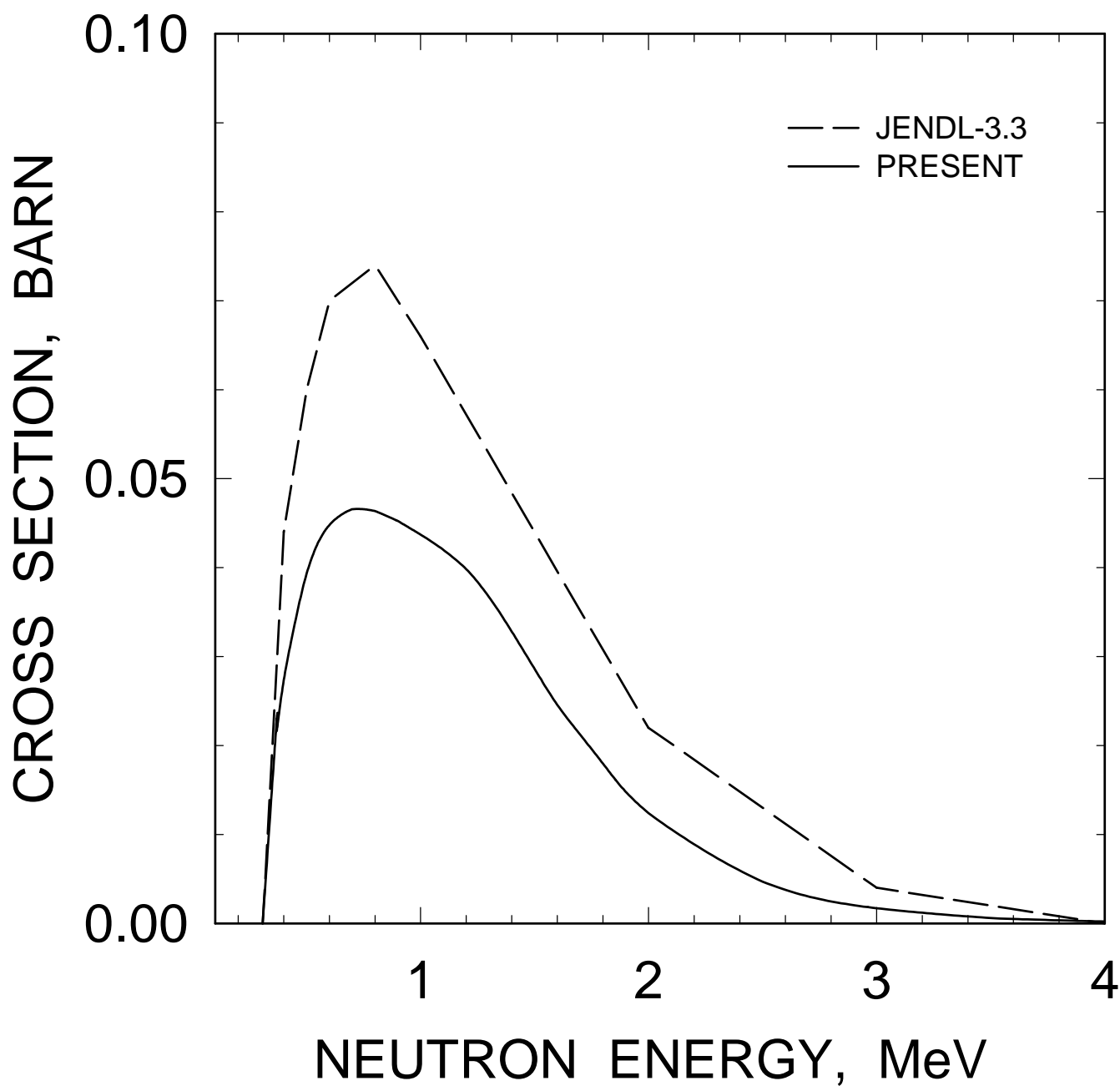


FIG. 43



$^{233}\text{Pa}$ : 0.3661,  $9/2^+$  LEVEL EXCITATION

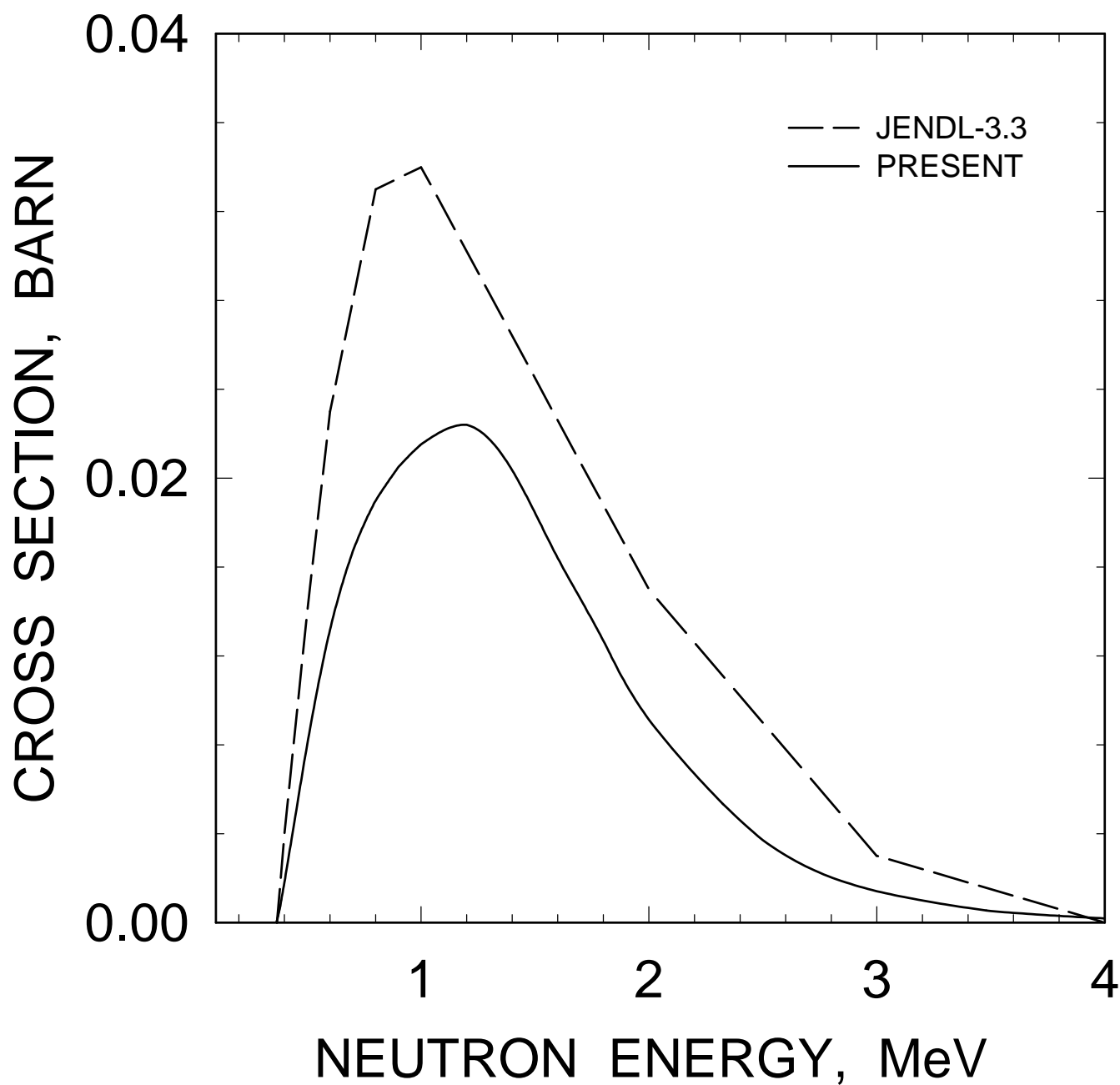


FIG. 44

# $^{233}\text{Pa}$ INELASTIC CROSS SECTION

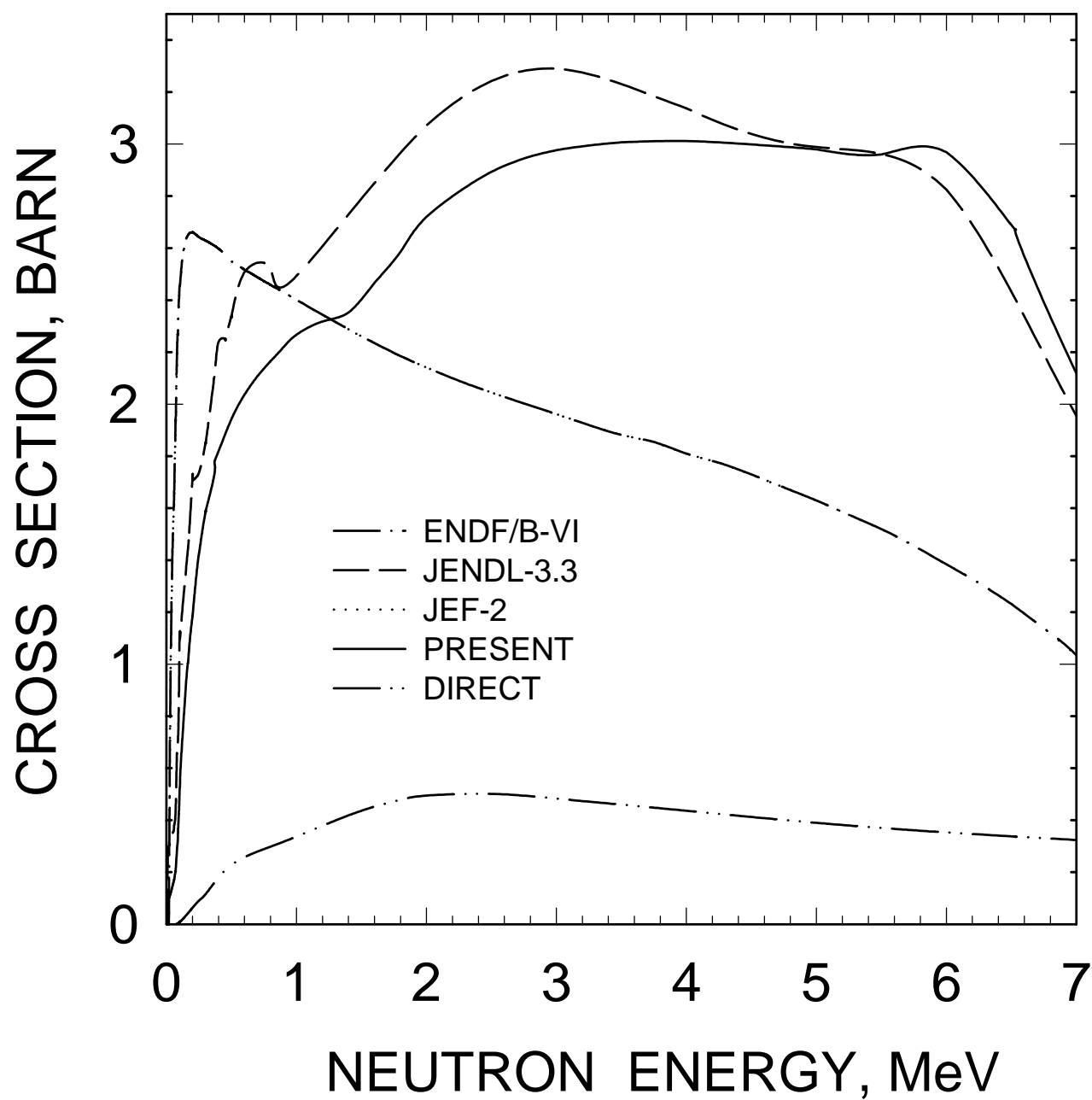


FIG. 45

# $^{233}\text{Pa}$ INELASTIC CROSS SECTION

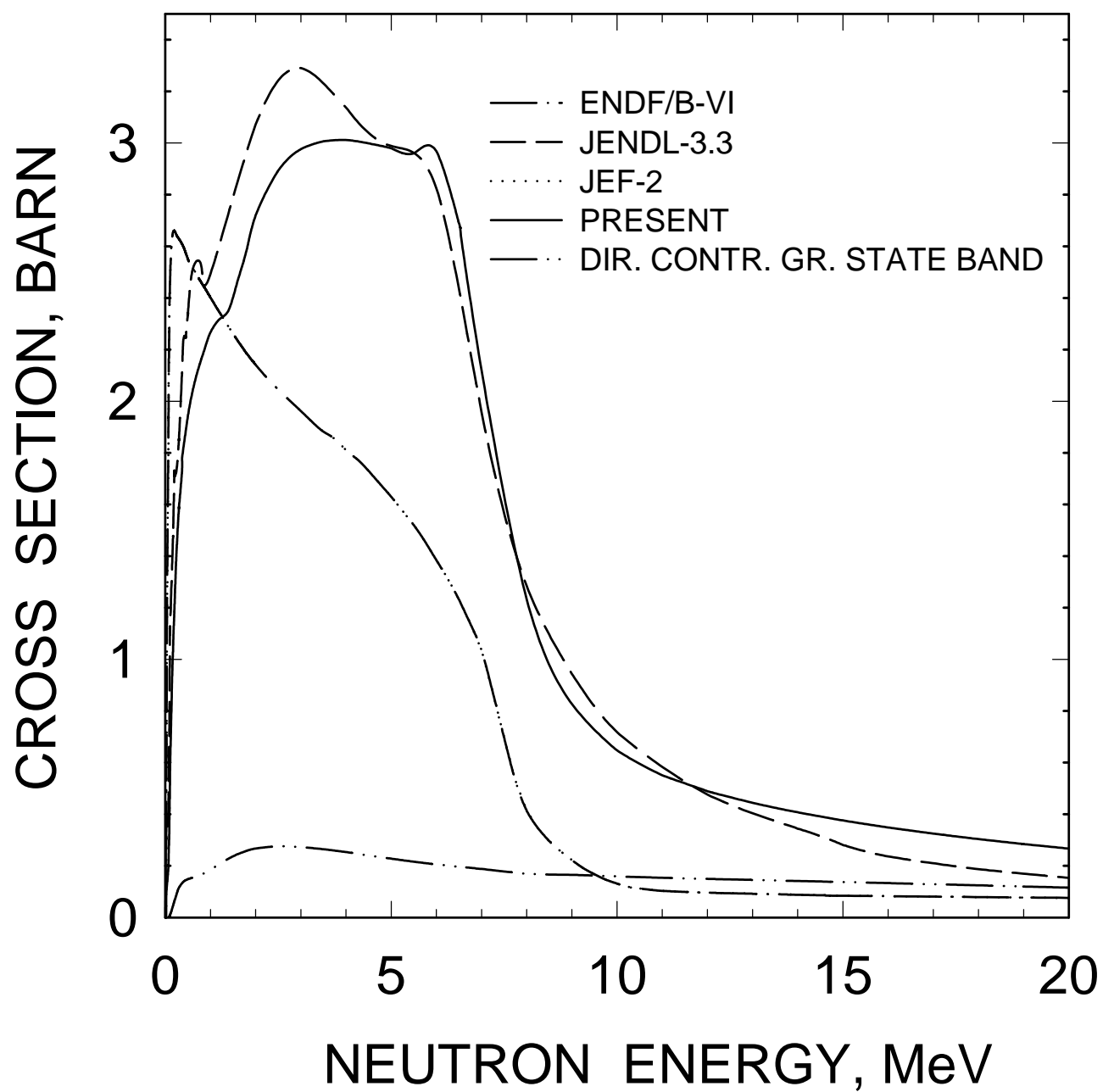


FIG. 46

$^{233}\text{Pa}$  INELASTIC CROSS SECTION  
(CONTINUUM CONTRIBUTION)

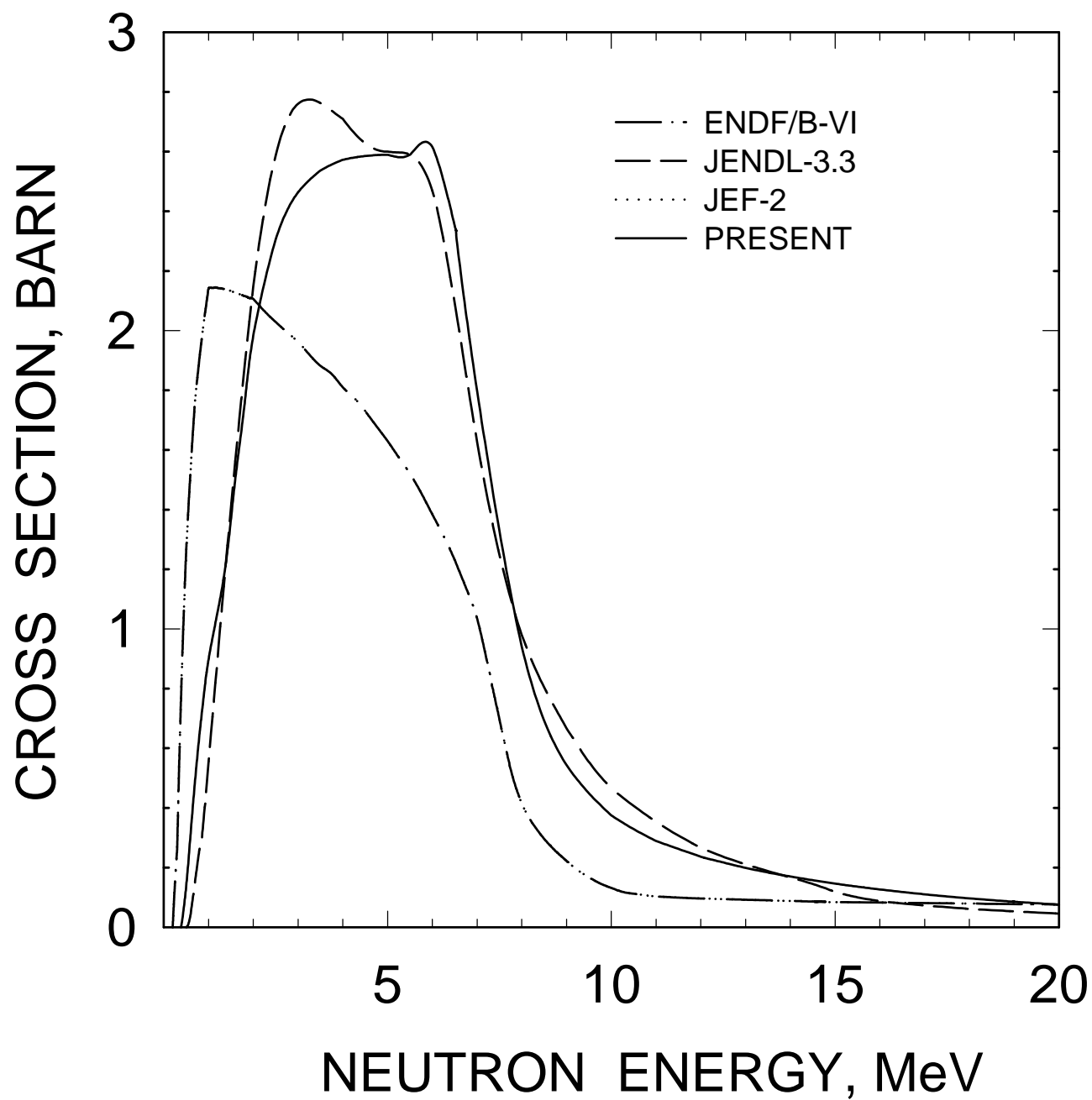


FIG. 47

# $^{233}\text{Pa}$ ( $n,\gamma$ ) CROSS SECTION

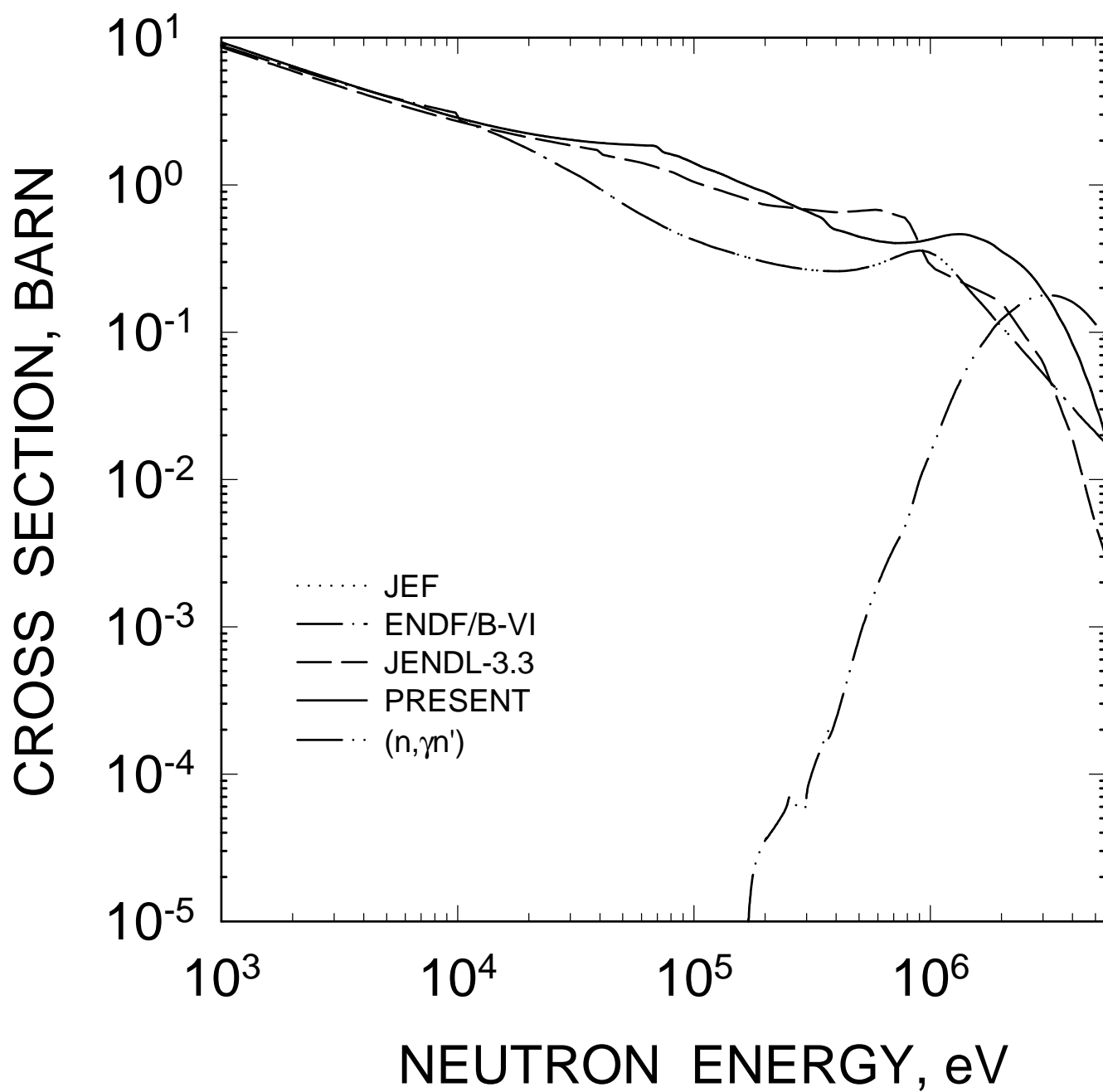


FIG. 48

# $^{233}\text{Pa}$ FISSION CROSS SECTION

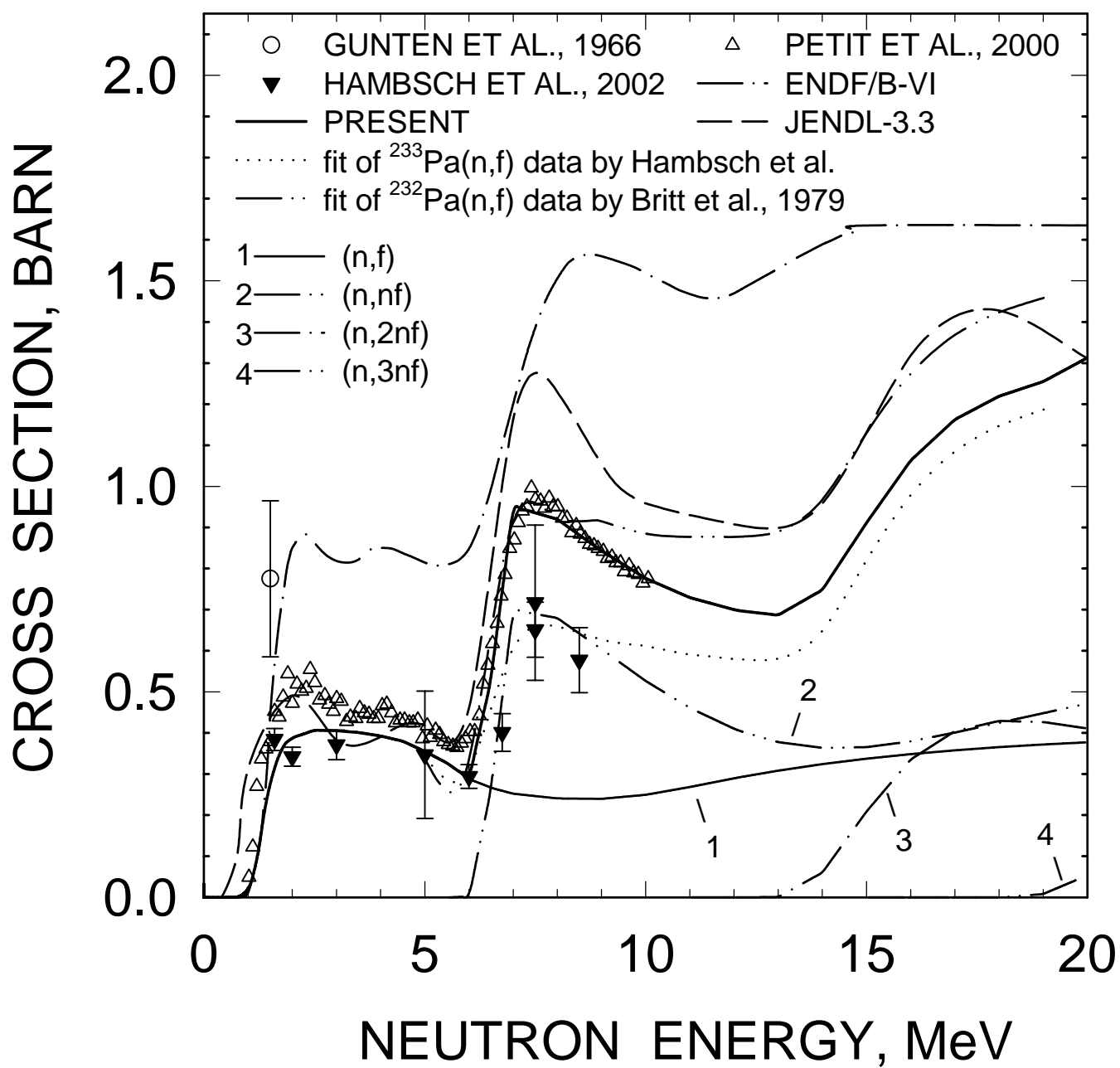


FIG. 49

# $^{233}\text{Pa}(\text{n},\text{f})$ CHANCE FISSION CONTRIBUTIONS

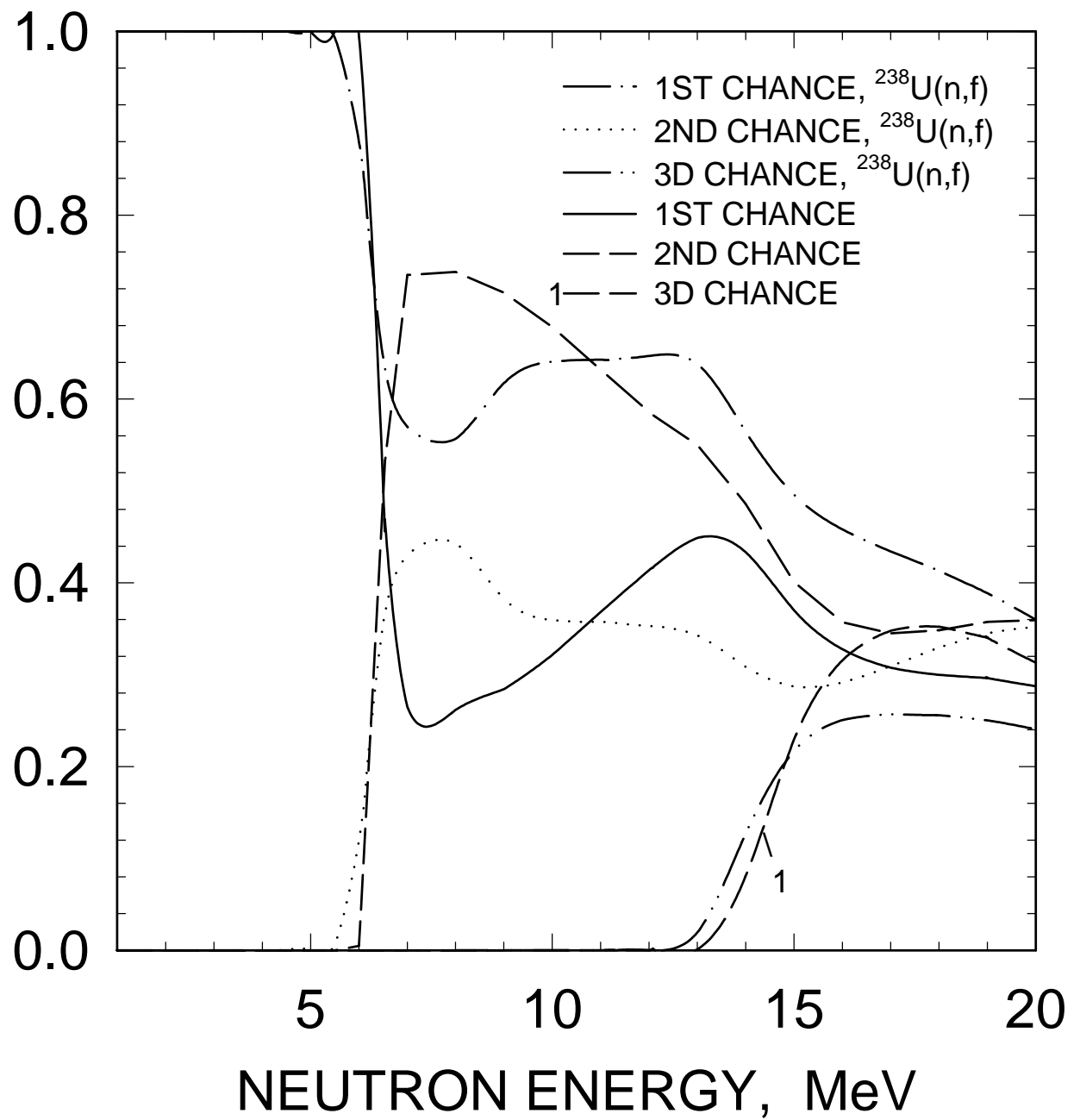


FIG. 50

# $^{232}\text{Pa}$ FISSION CROSS SECTION

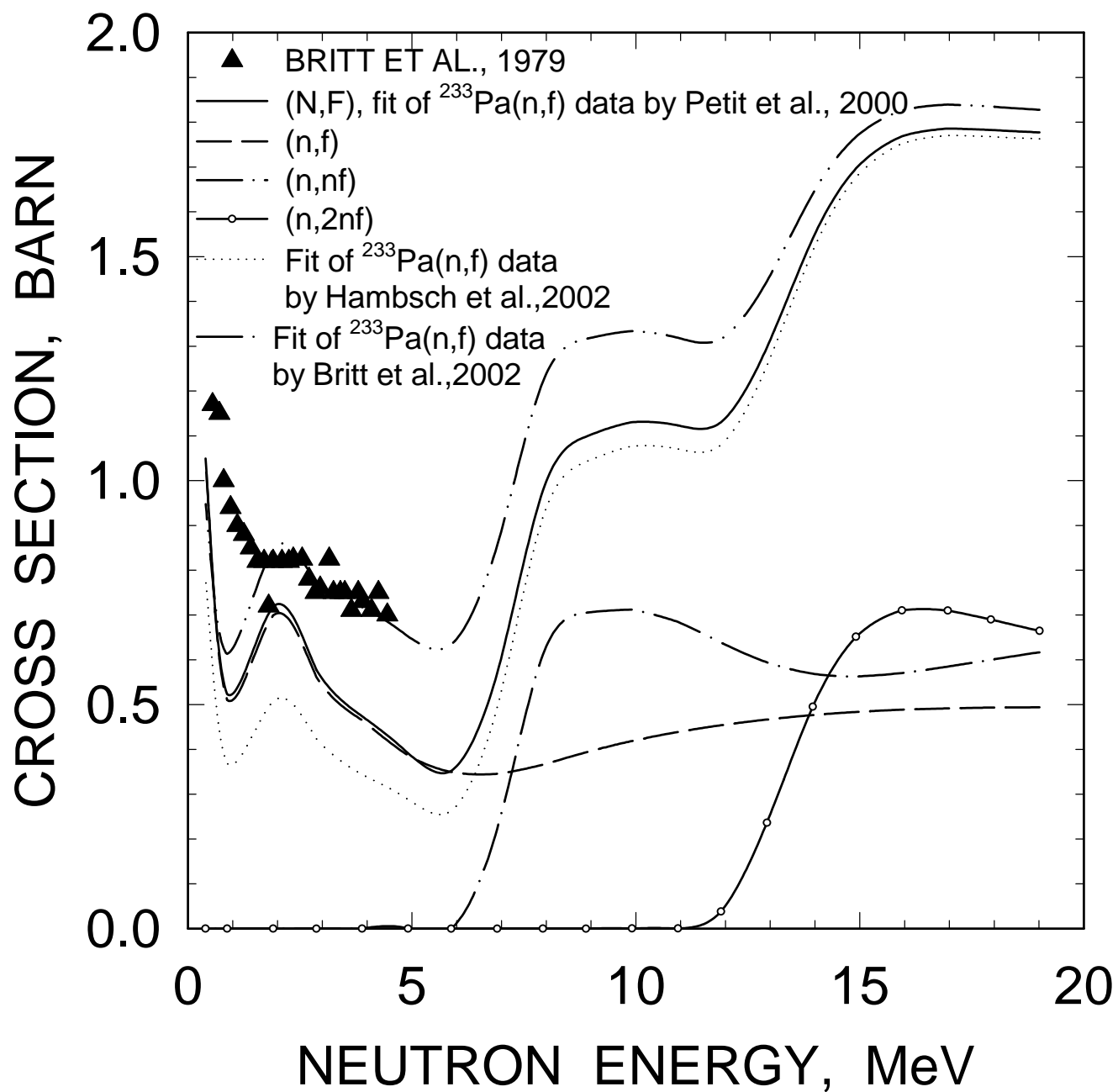
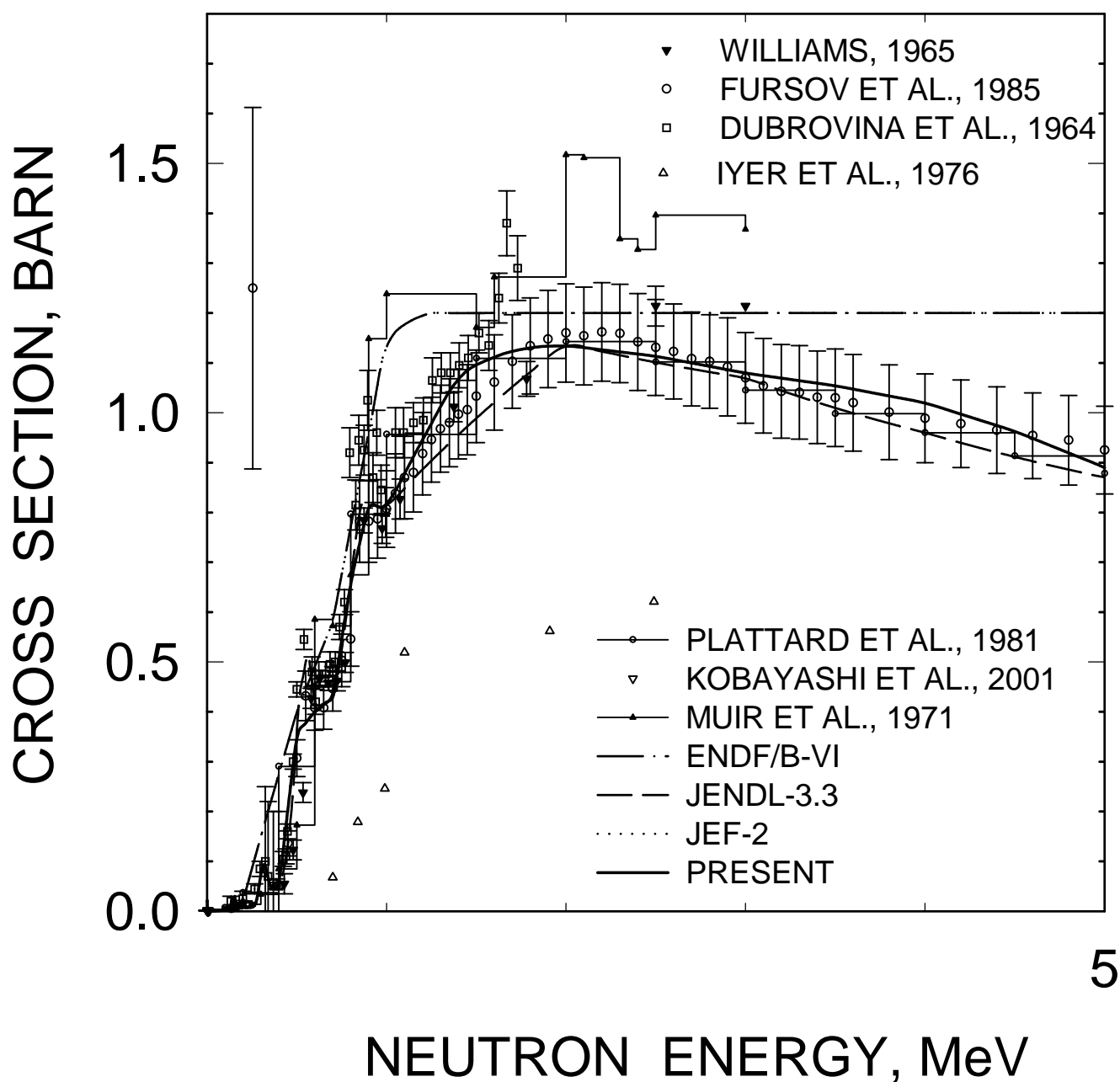


FIG. 51



# $^{231}\text{Pa}$ FISSION CROSS SECTION



5

FIG. 52

# $^{233}\text{Pa}$ (N,2N) CROSS SECTION

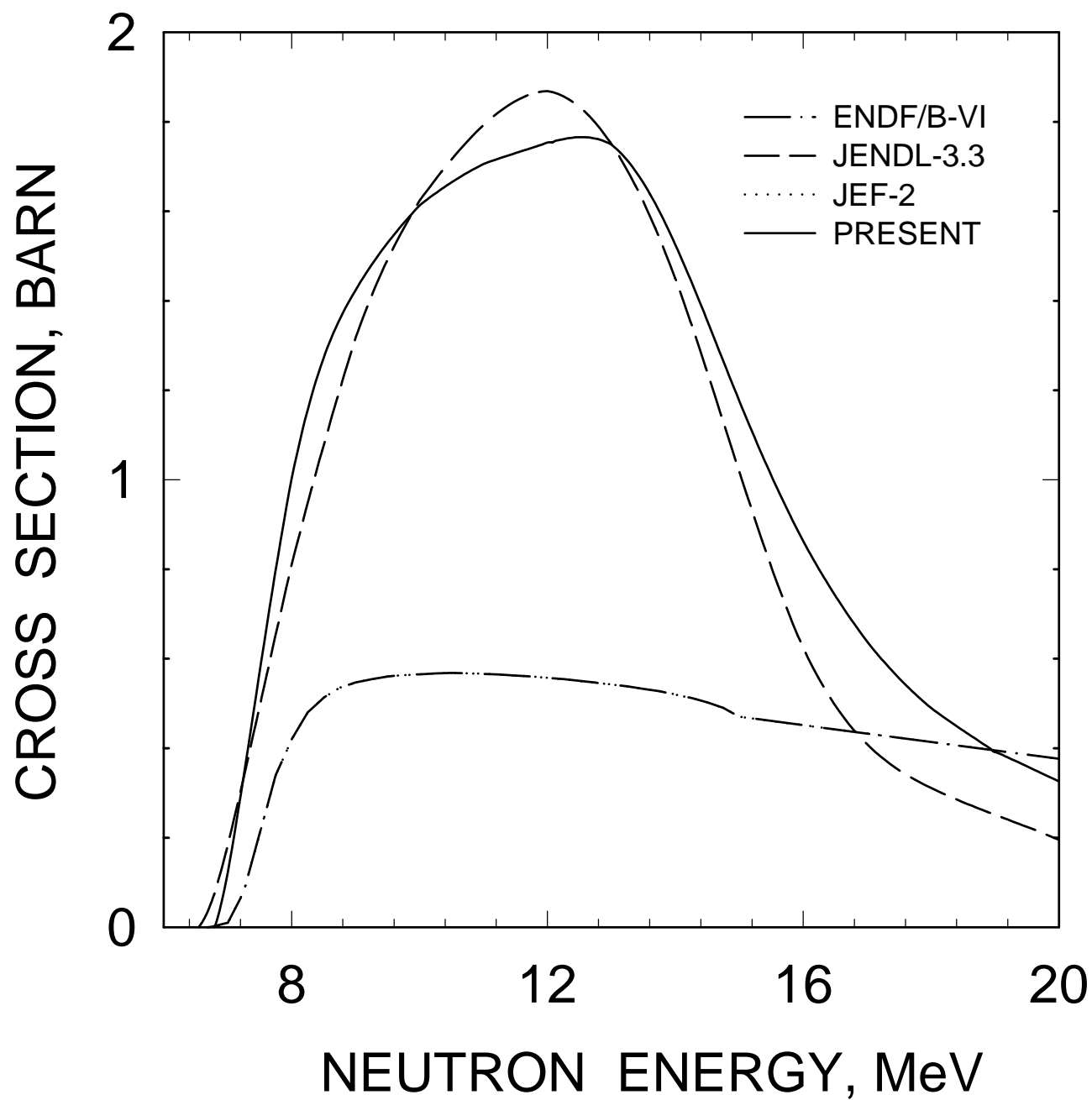


FIG. 53

# $^{233}\text{Pa}$ (N,3N) CROSS SECTION

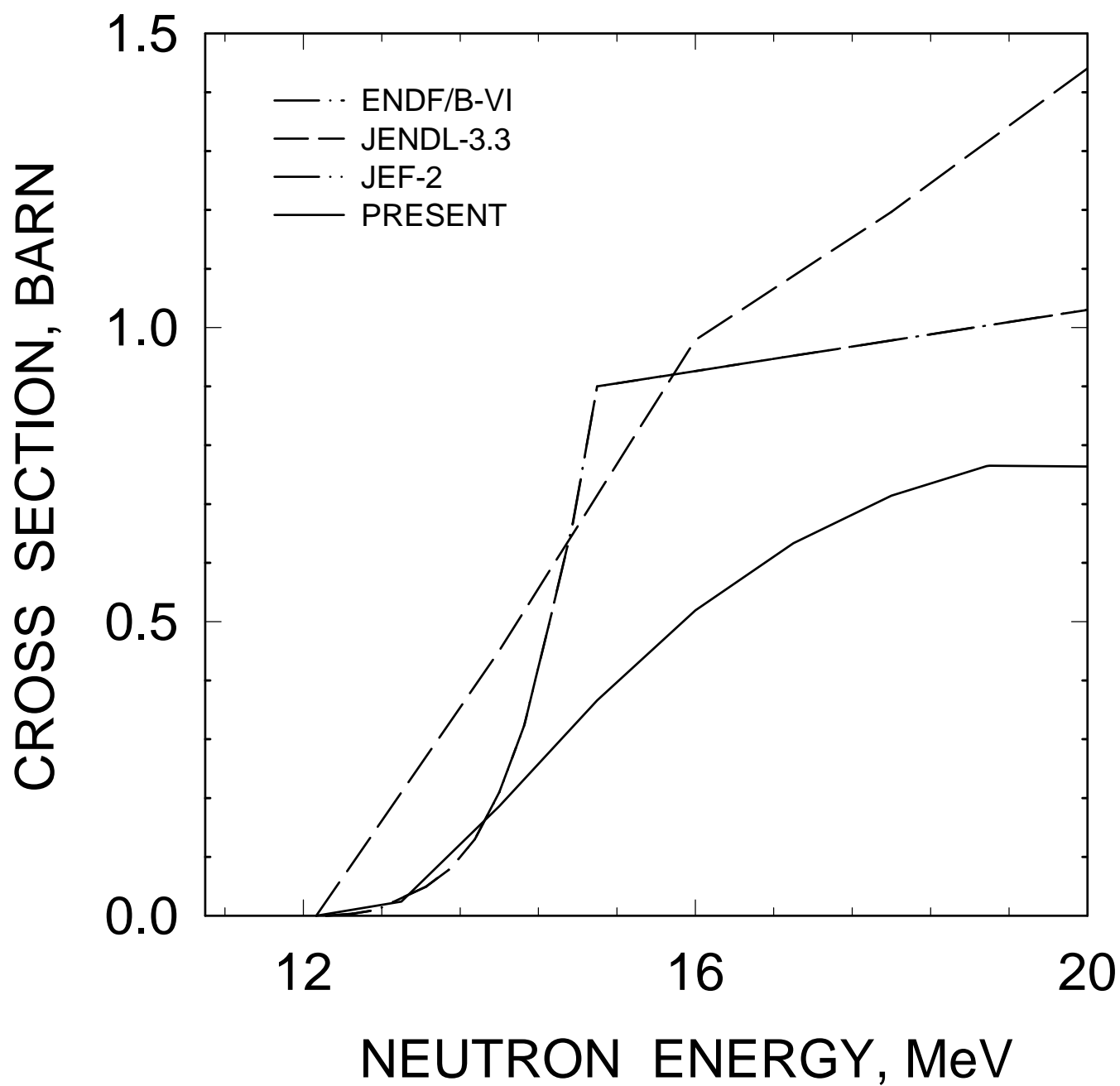


FIG. 54

# $^{233}\text{Pa}$ , NEUTRON MULTIPLICITY

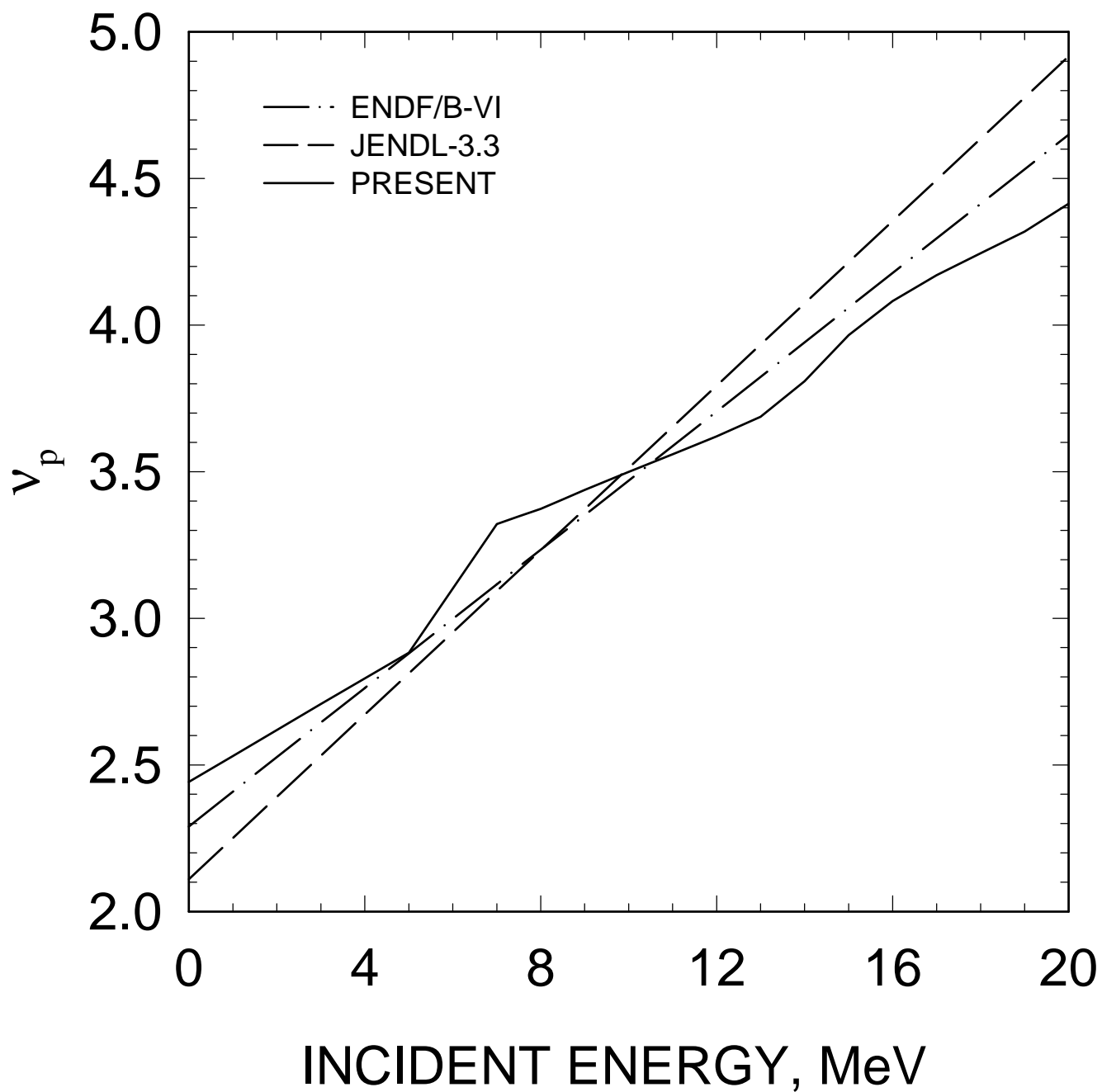


FIG. 55

# $^{233}\text{Pa}$ , NEUTRON MULTIPLICITY

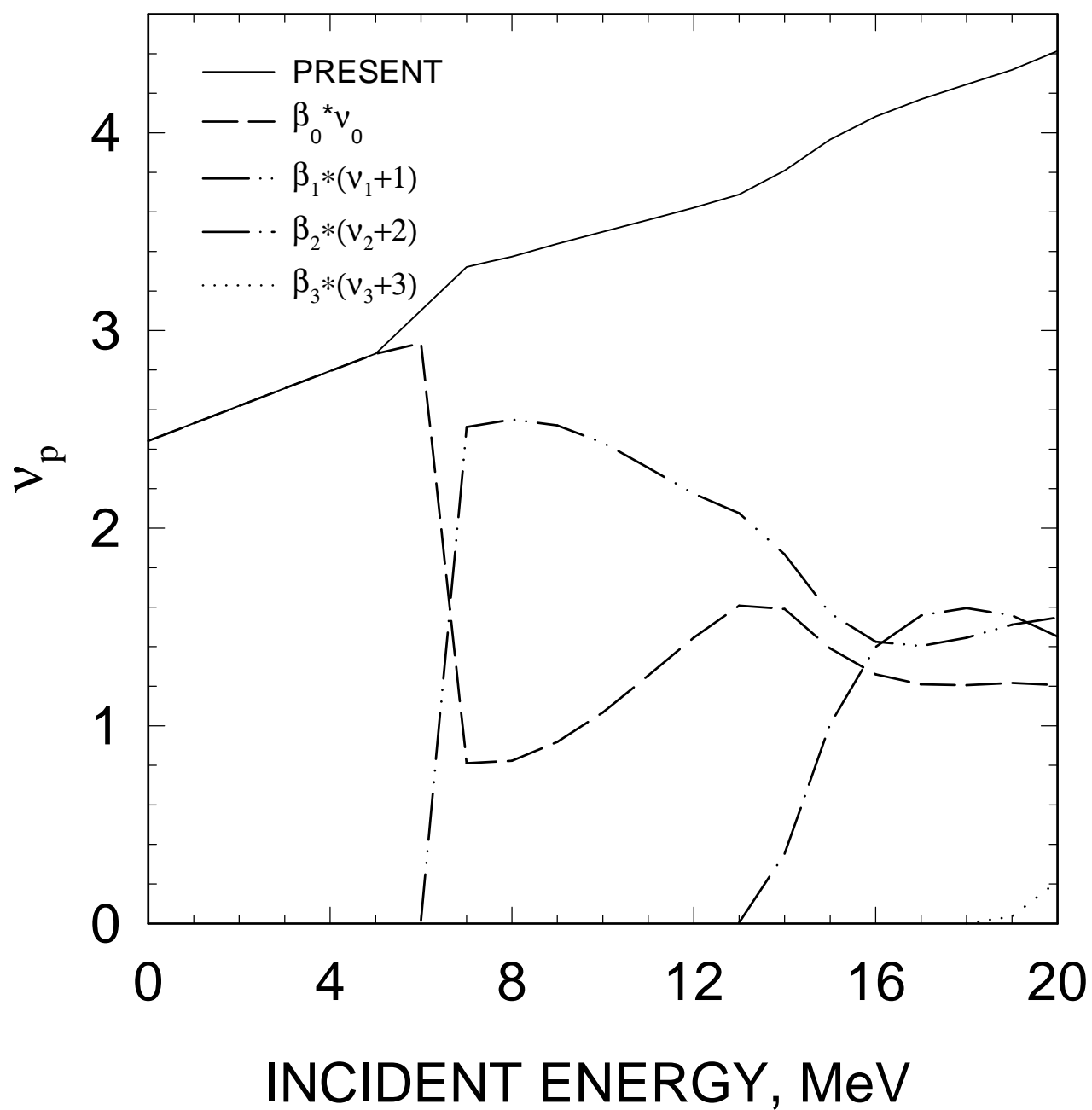


FIG. 56

$^{233}\text{Pa}$      $E_n=20 \text{ MeV}$   
 COMPONENTS OF FIRST NEUTRON  
 SPECTRUM

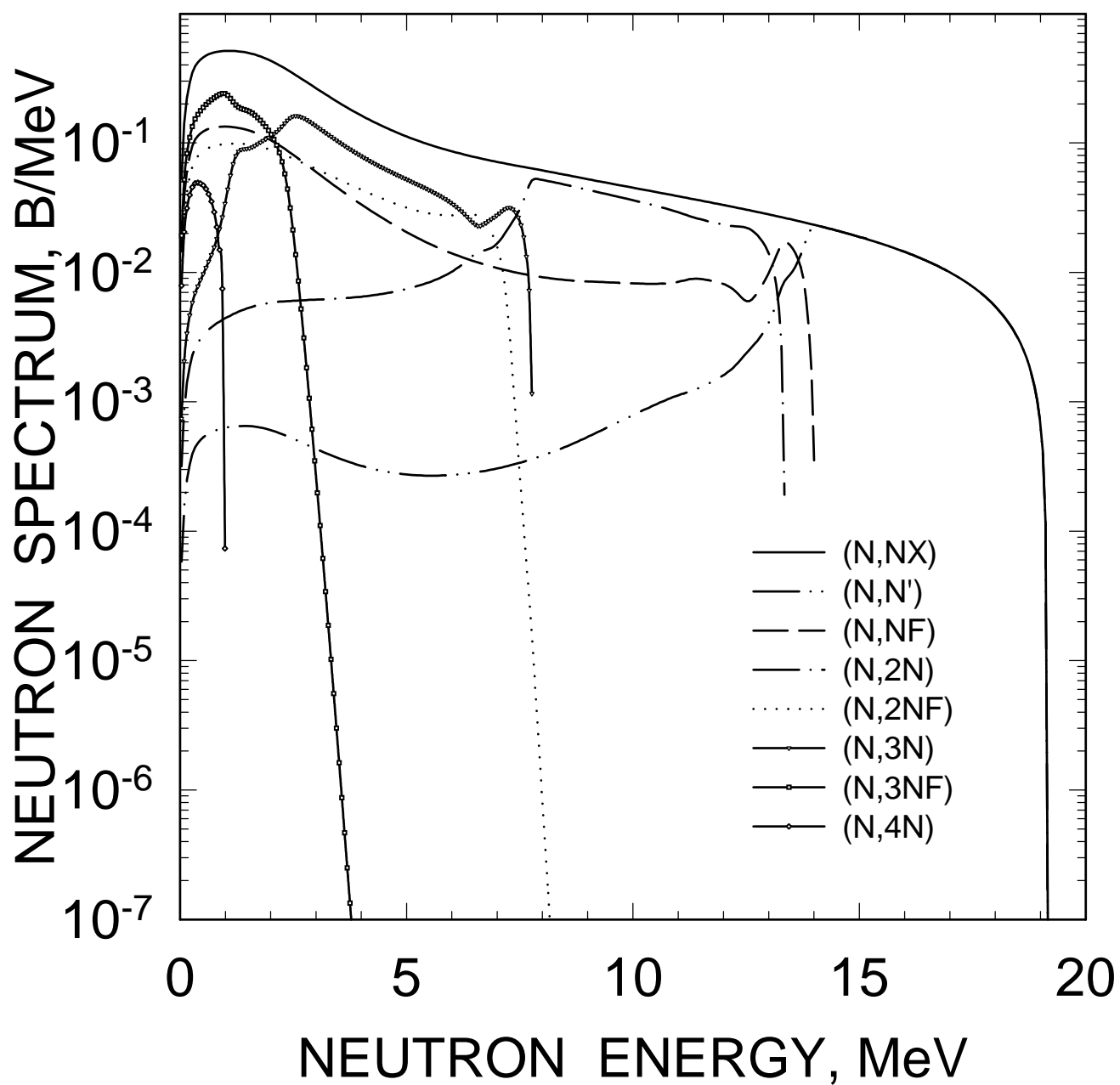


FIG. 57

$^{233}\text{Pa}$      $E_n = 20 \text{ MeV}$   
COMPONENTS OF SECOND NEUTRON  
SPECTRUM

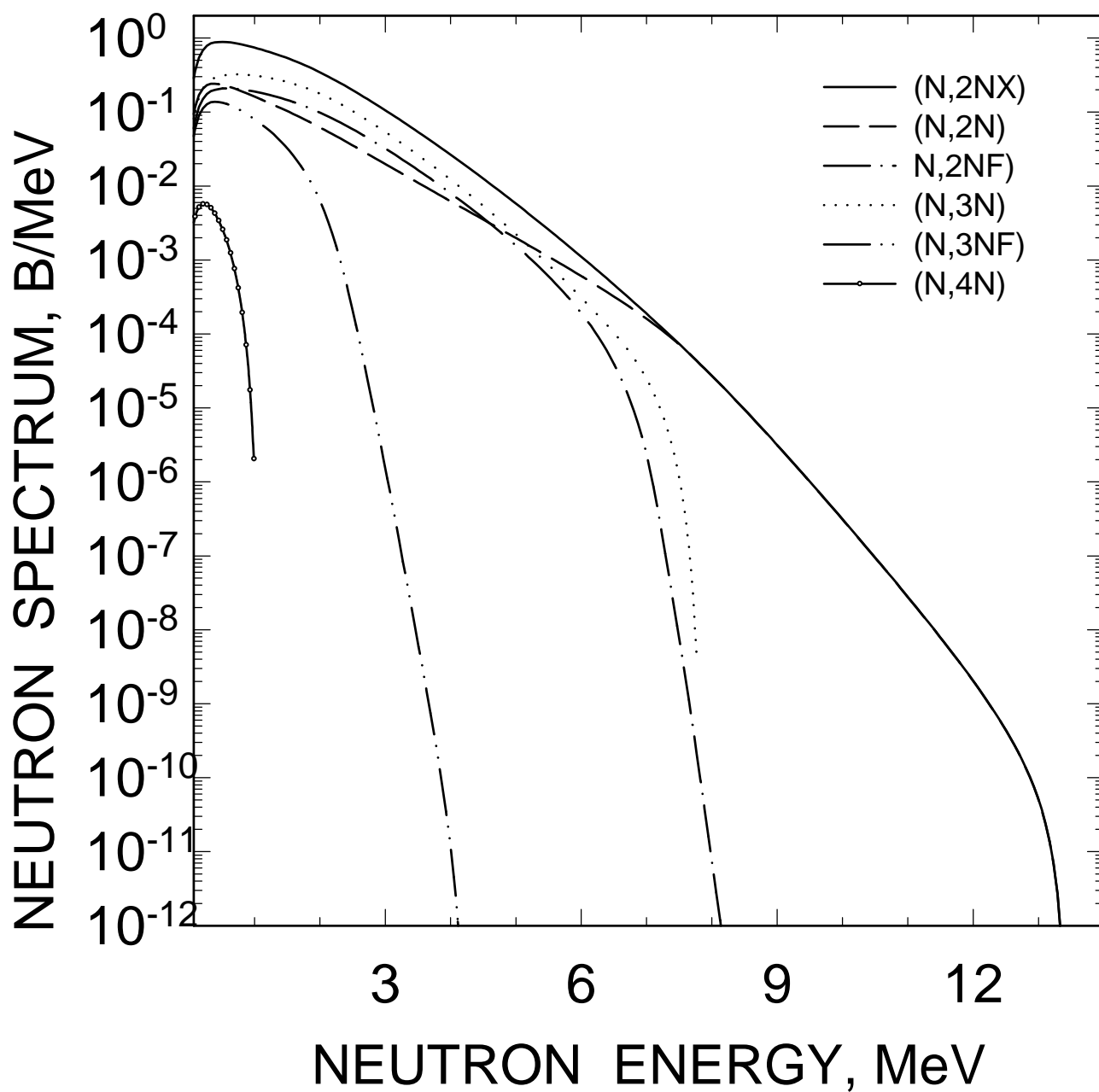


FIG. 58

$^{233}\text{Pa}$      $E_n = 20 \text{ MeV}$   
COMPONENTS OF THIRD NEUTRON  
SPECTRUM

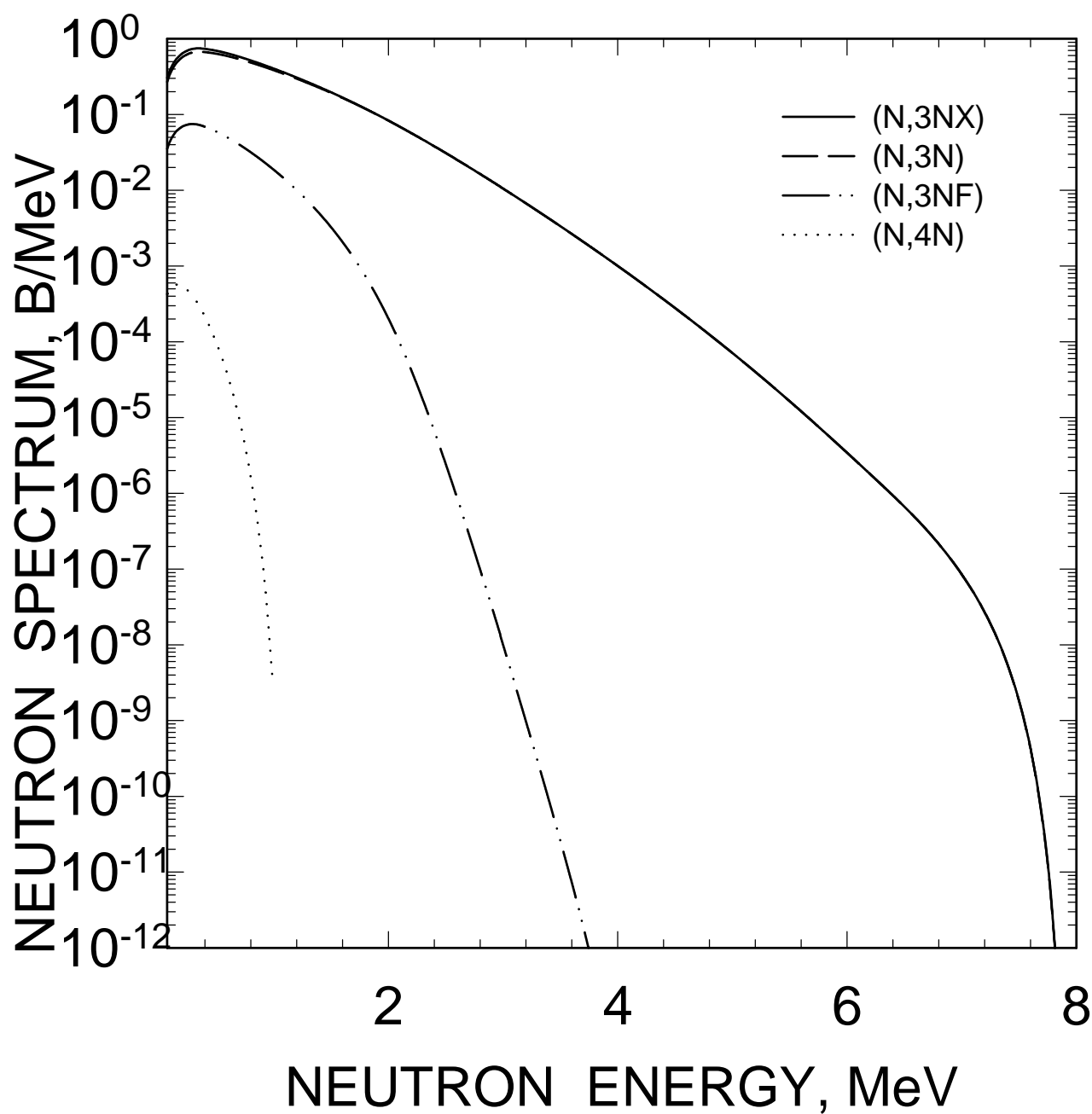


FIG. 59



$^{233}\text{Pa}$      $E_n = 20 \text{ MeV}$   
COMPONENTS OF FOURTH NEUTRON  
SPECTRUM

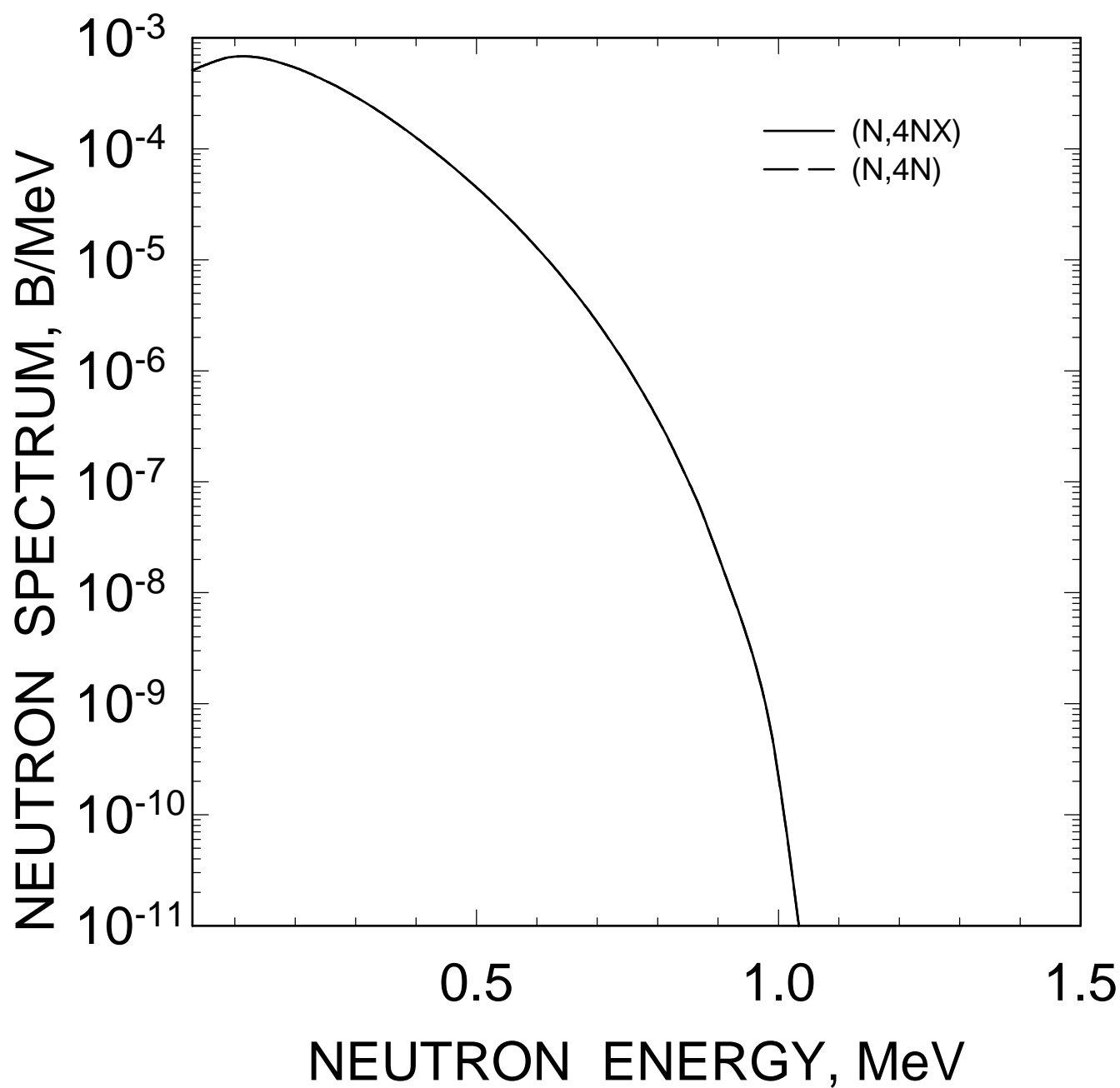


FIG. 60

$^{233}\text{Pa}$   $E_n=14\text{ MeV}$   
COMPONENTS OF FIRST NEUTRON  
SPECTRUM

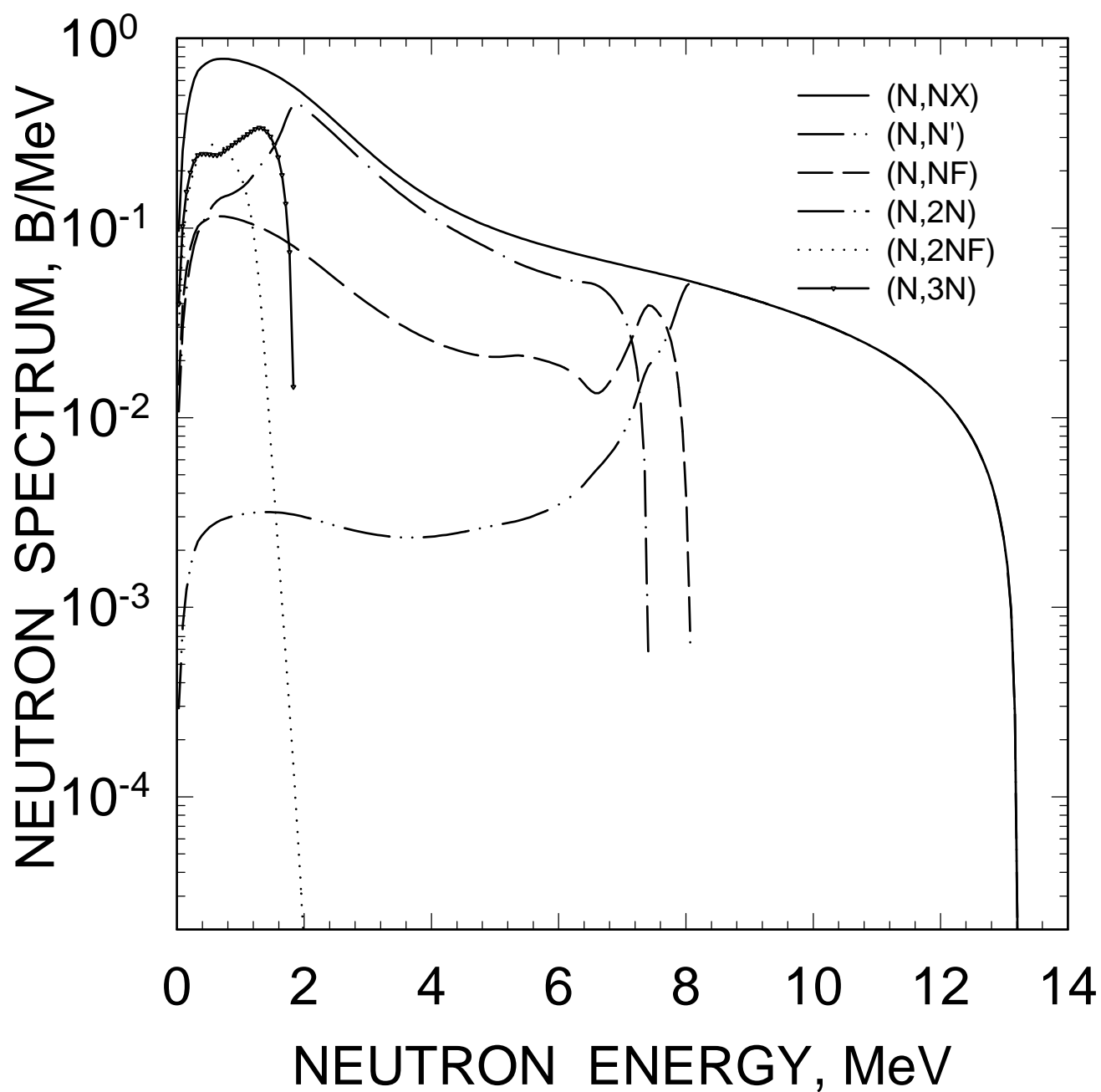


FIG. 61

$^{233}\text{Pa}$      $E_n = 14 \text{ MeV}$   
COMPONENTS OF SECOND NEUTRON  
SPECTRUM

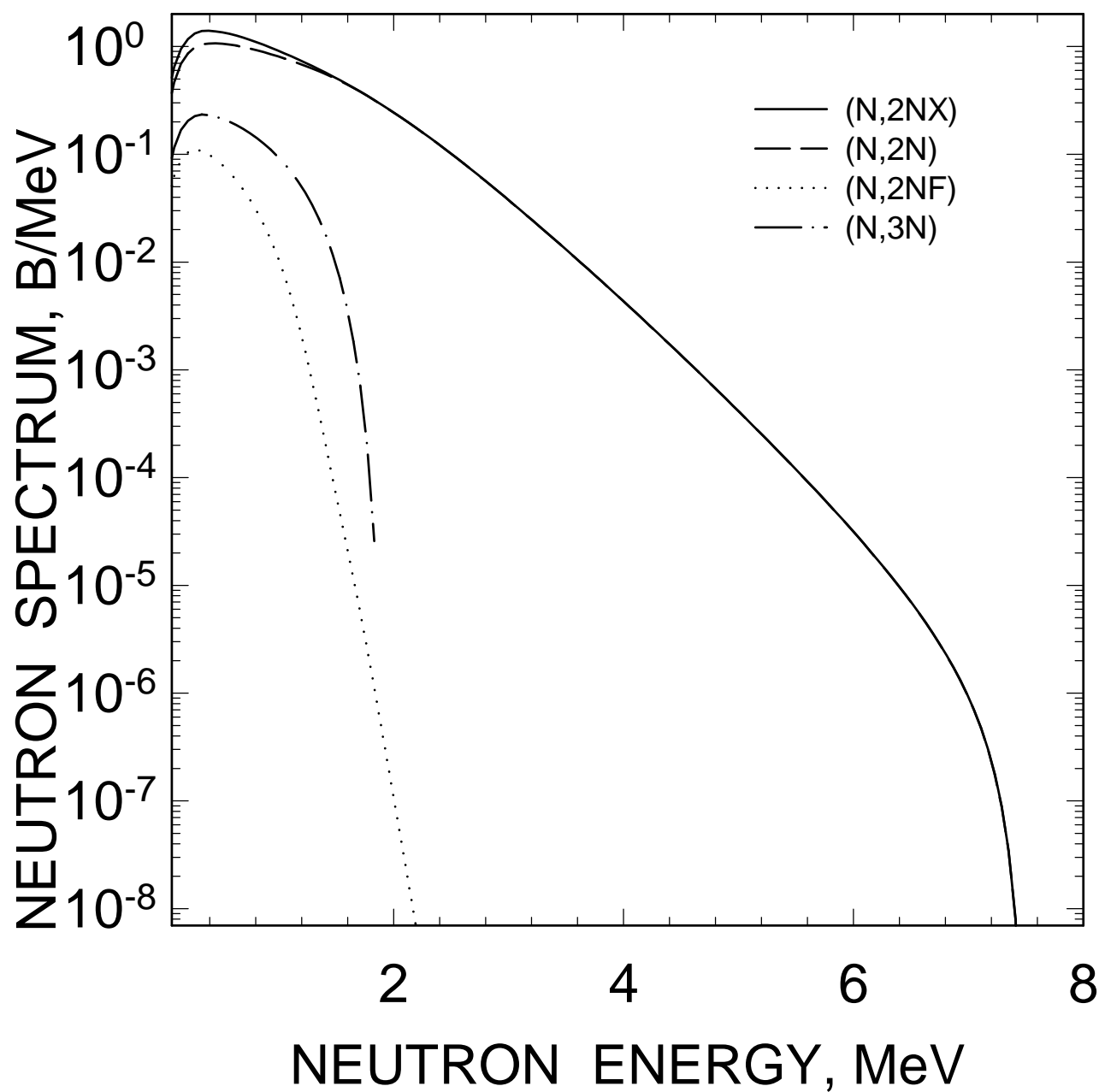


FIG. 62

$^{233}\text{Pa}$      $E_n=14 \text{ MeV}$   
COMPONENTS OF THIRD NEUTRON  
SPECTRUM

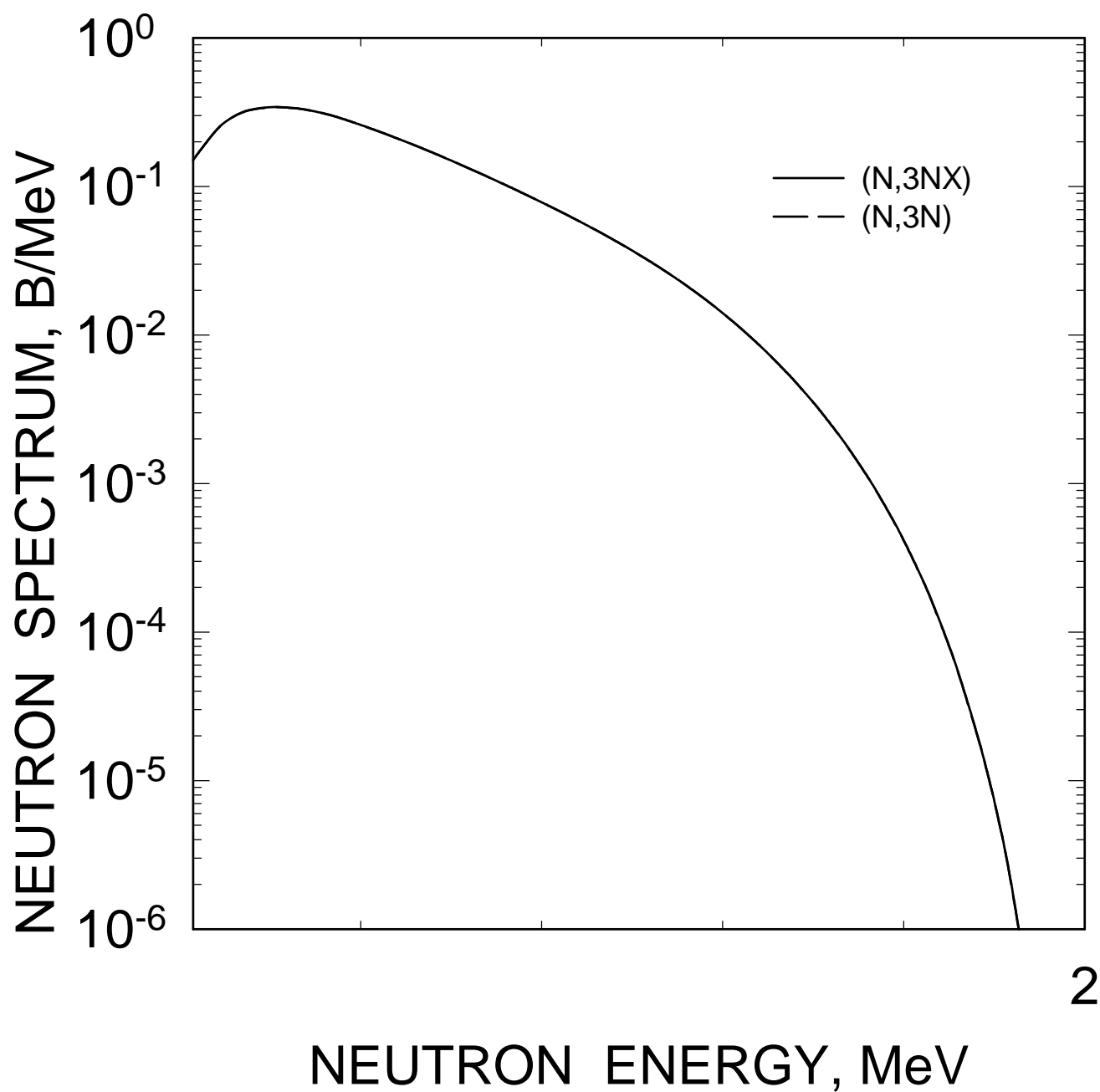


FIG. 63

$^{233}\text{Pa}$      $E_n = 8 \text{ MeV}$   
COMPONENTS OF FIRST NEUTRON  
SPECTRUM

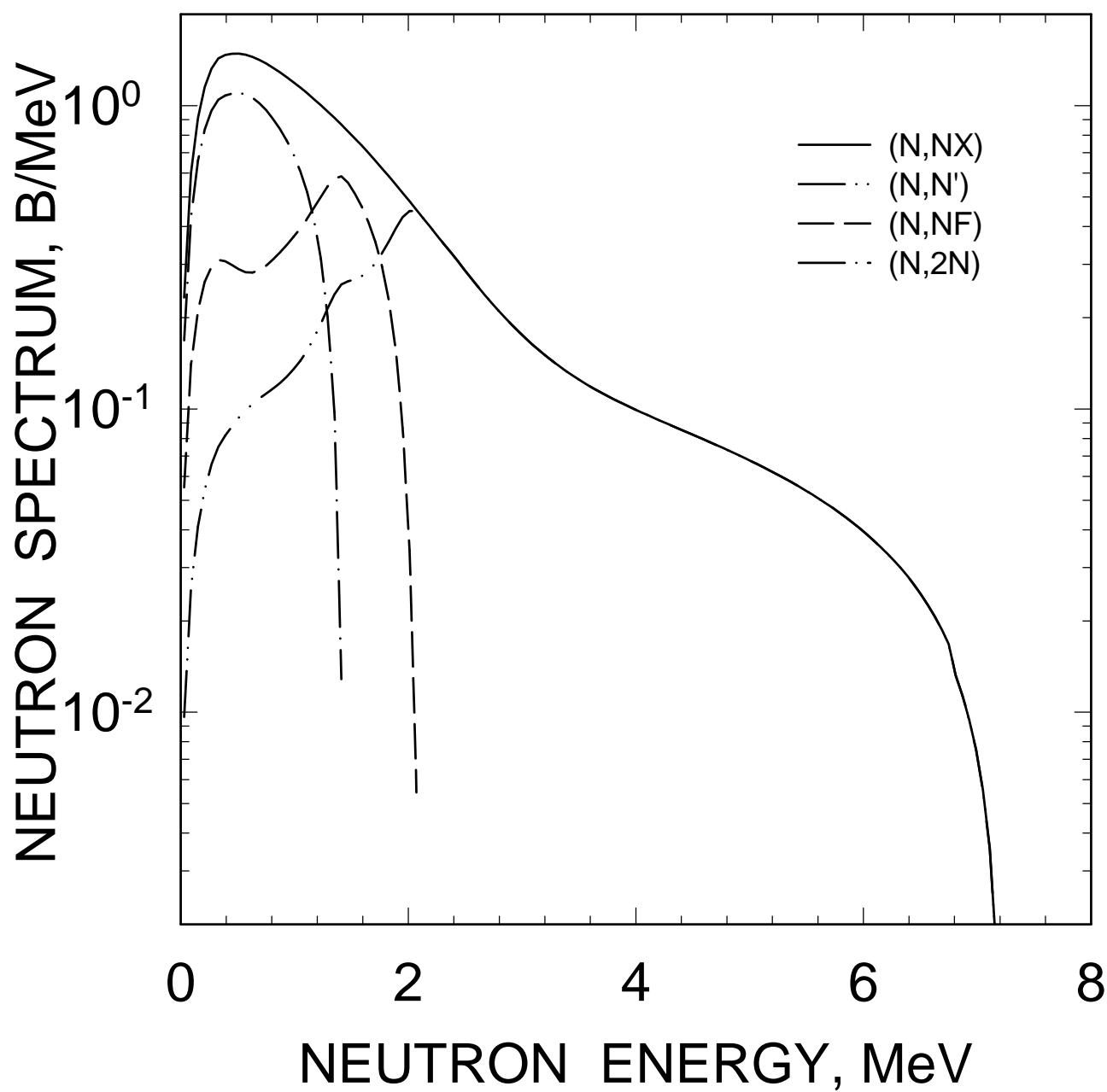


FIG. 64

$^{233}\text{Pa}$      $E_n = 8 \text{ MeV}$   
COMPONENTS OF SECOND NEUTRON  
SPECTRUM

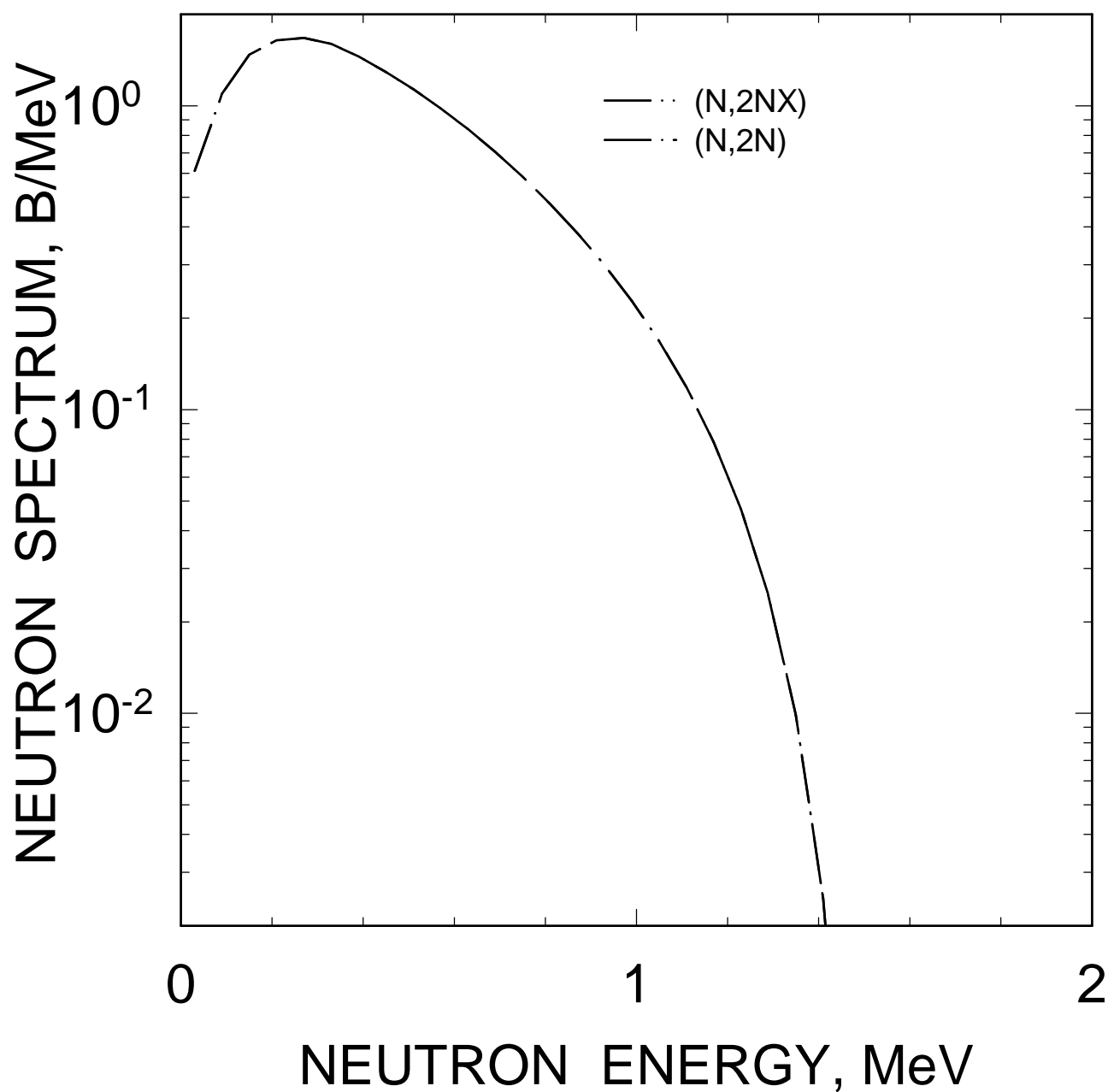


FIG. 65

<sup>233</sup>Pa FISSION NEUTRON SPECTRUM  
 $E_n=2$  MeV

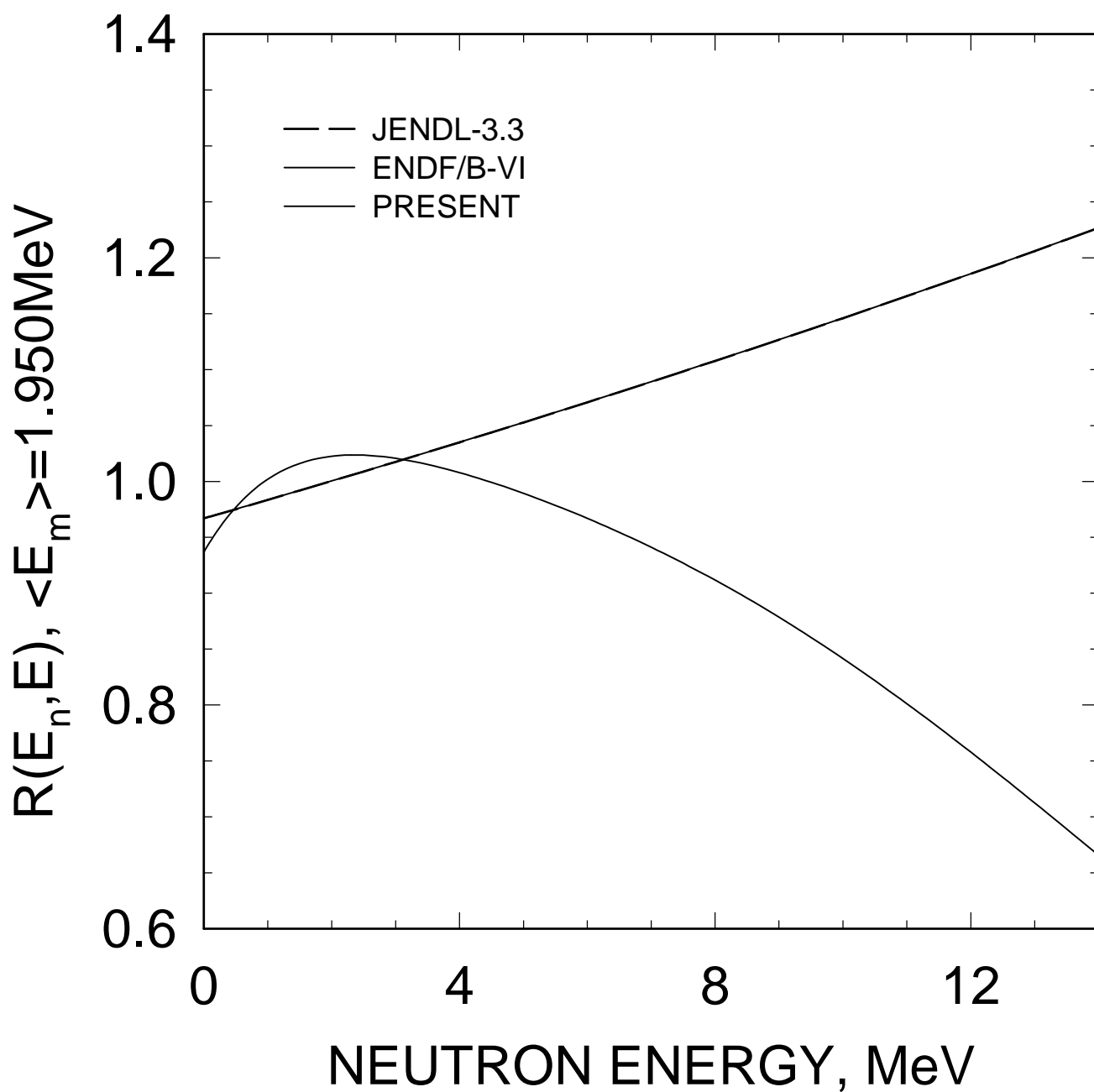


FIG. 66

$^{233}\text{Pa}$  FISSION NEUTRON SPECTRUM  
 $E_n=7\text{ MeV}$

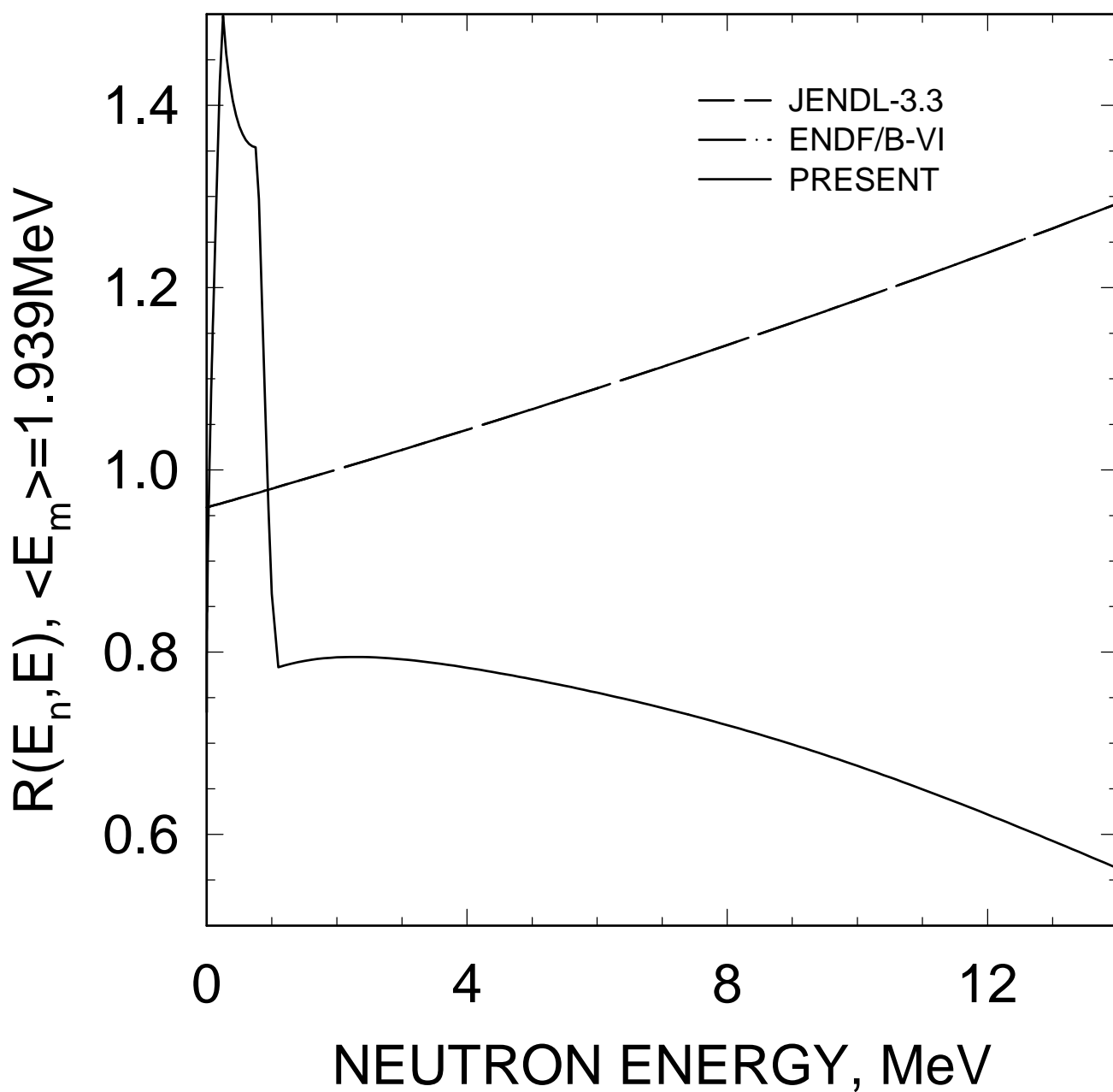


FIG. 67



<sup>233</sup>Pa FISSION NEUTRON SPECTRUM  
E<sub>n</sub>=14 MeV

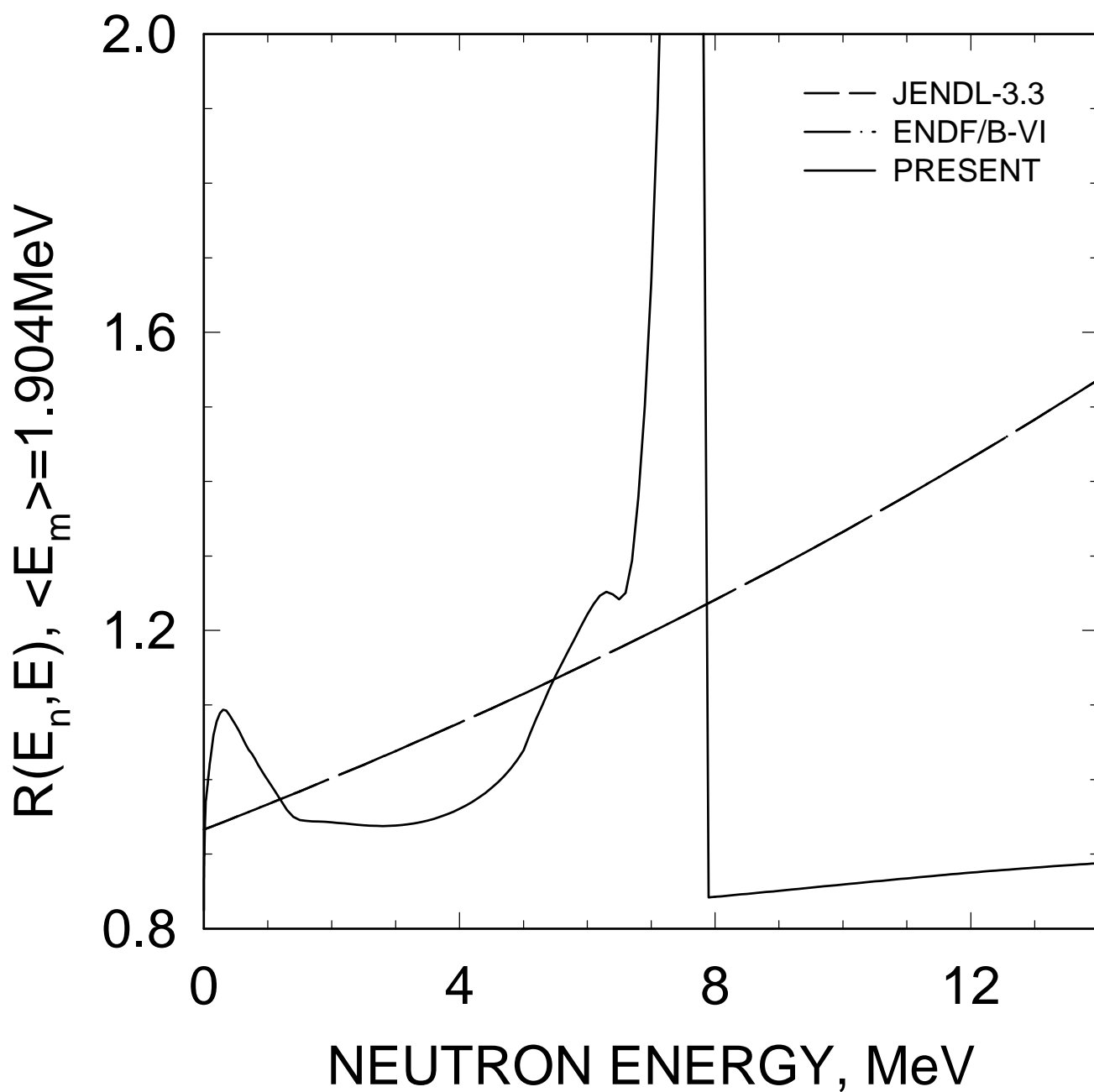


FIG. 68

$^{231}\text{Pa}$  FISSION NEUTRON SPECTRUM  
 $E_n=20\text{ MeV}$

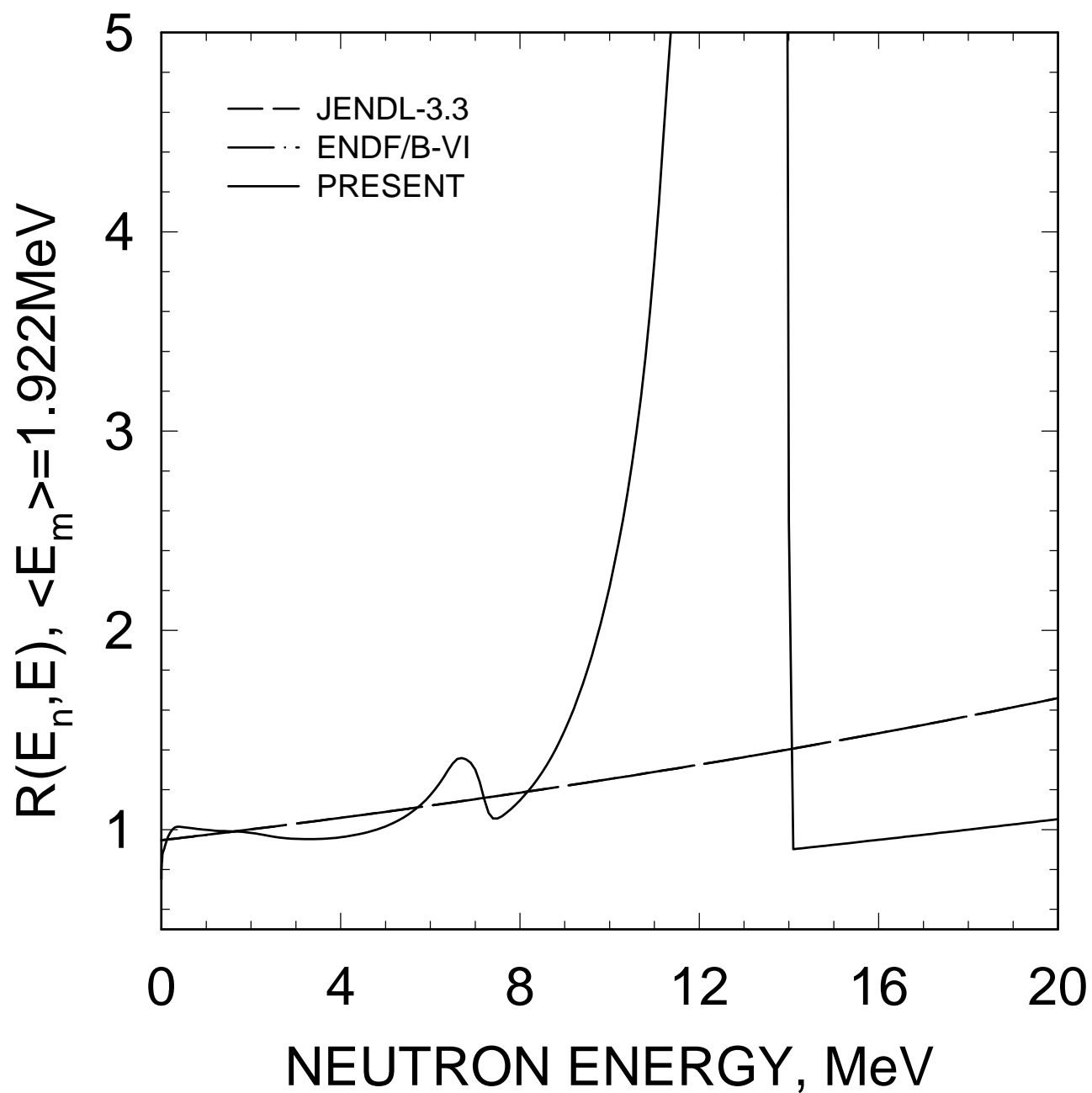


FIG. 69

$^{233}\text{Pa}$ , AVERAGE NEUTRON ENERGY

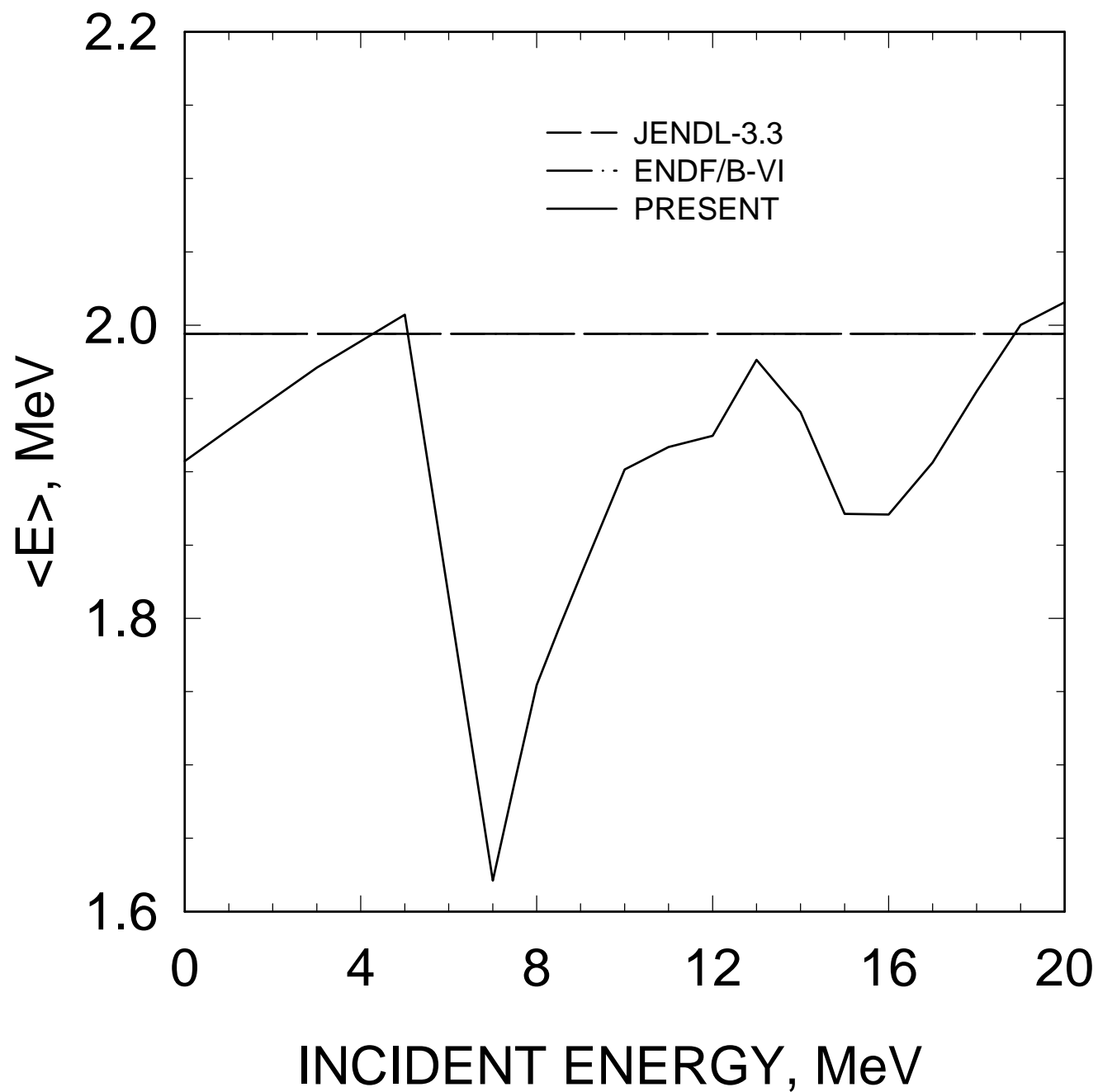


FIG. 70

$^{233}\text{Pa}$   $E_n = 20 \text{ MeV}$   
COMPARISON WITH JENDL-3.3  
AND ENDF/B-VI

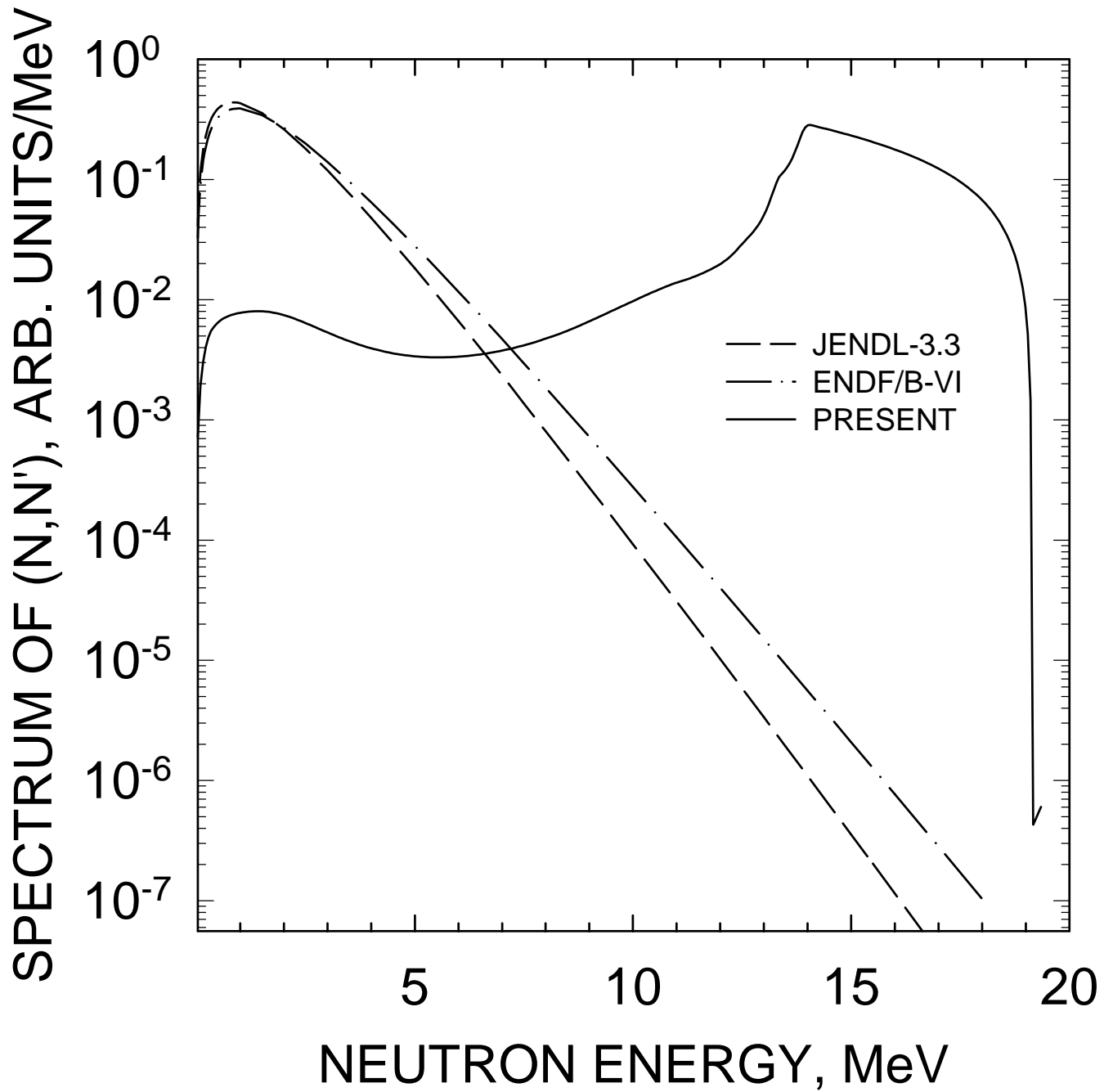


FIG. 71

$^{233}\text{Pa}$   $E_n = 14$  MeV  
COMPARISON WITH JENDL-3.3

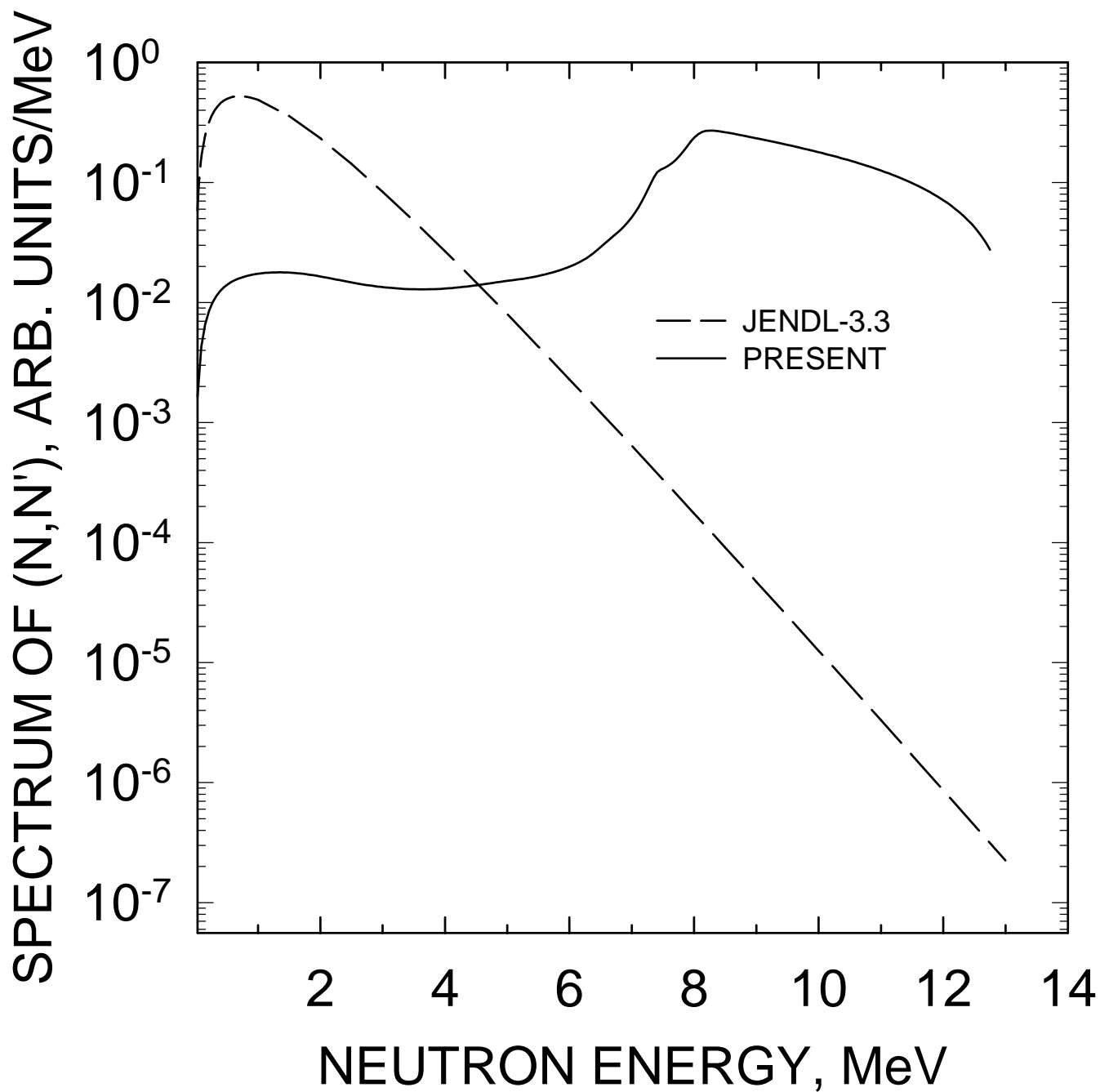


FIG. 72

$^{233}\text{Pa}$   $E_n = 10 \text{ MeV}$   
COMPARISON WITH JENDL-3.3

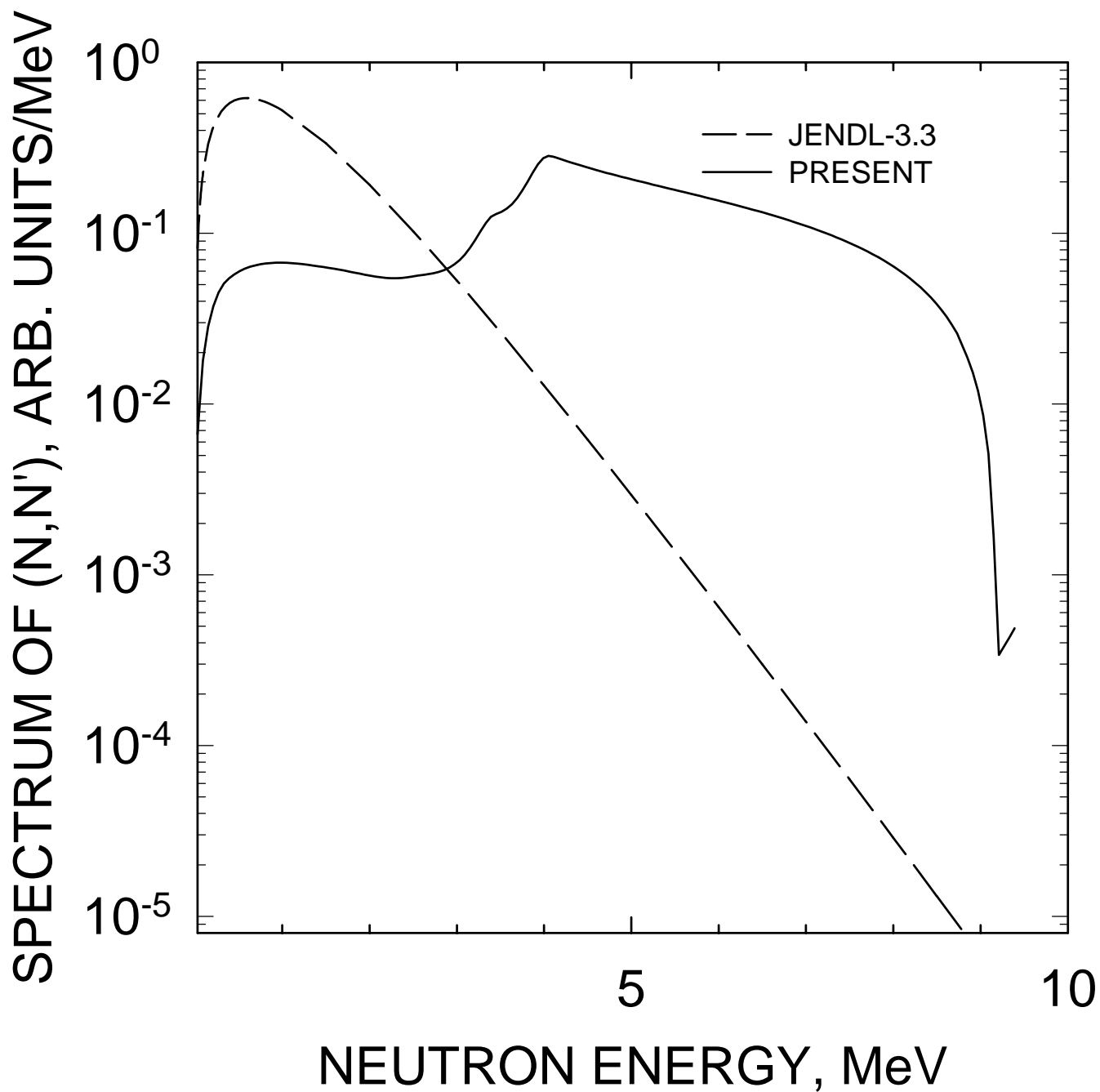


FIG. 73

$^{233}\text{Pa}$   $E_n = 8 \text{ MeV}$   
COMPARISON WITH JENDL-3.3

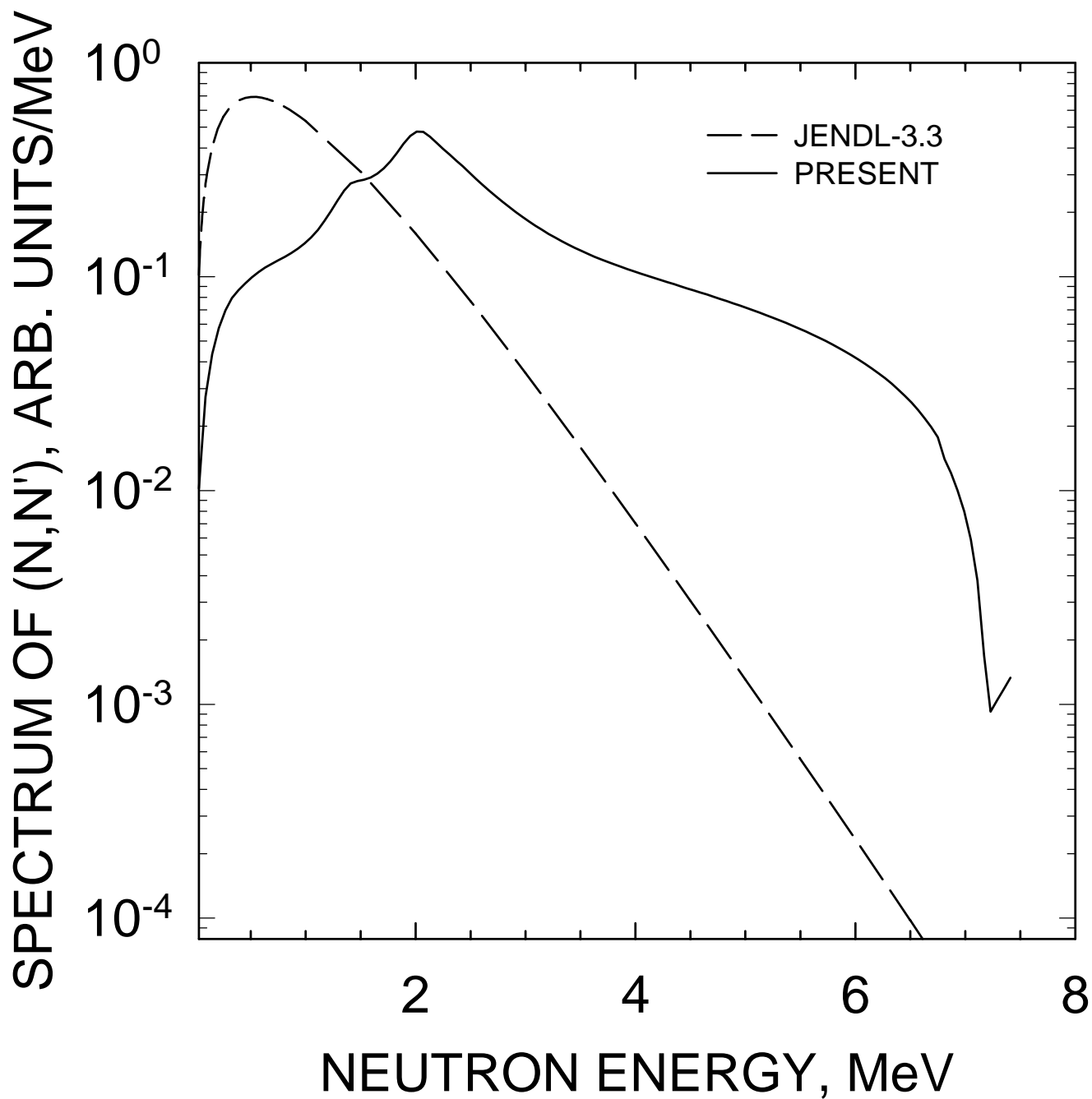


FIG. 74

$^{233}\text{Pa}$   $E_n = 6 \text{ MeV}$   
COMPARISON WITH JENDL-3.3

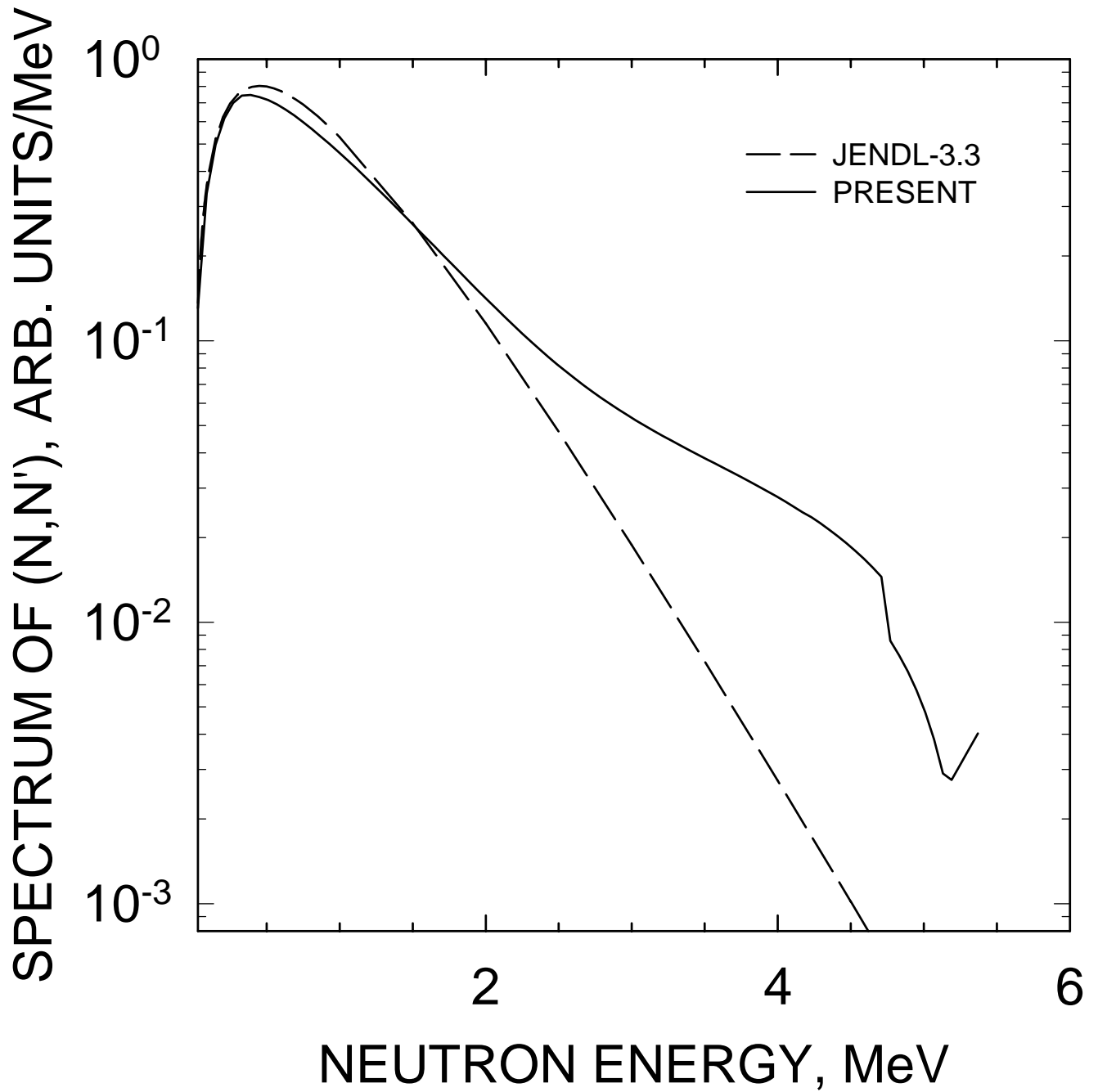


FIG. 75



$^{233}\text{Pa}$   $E_n = 4 \text{ MeV}$   
COMPARISON WITH JENDL-3.3

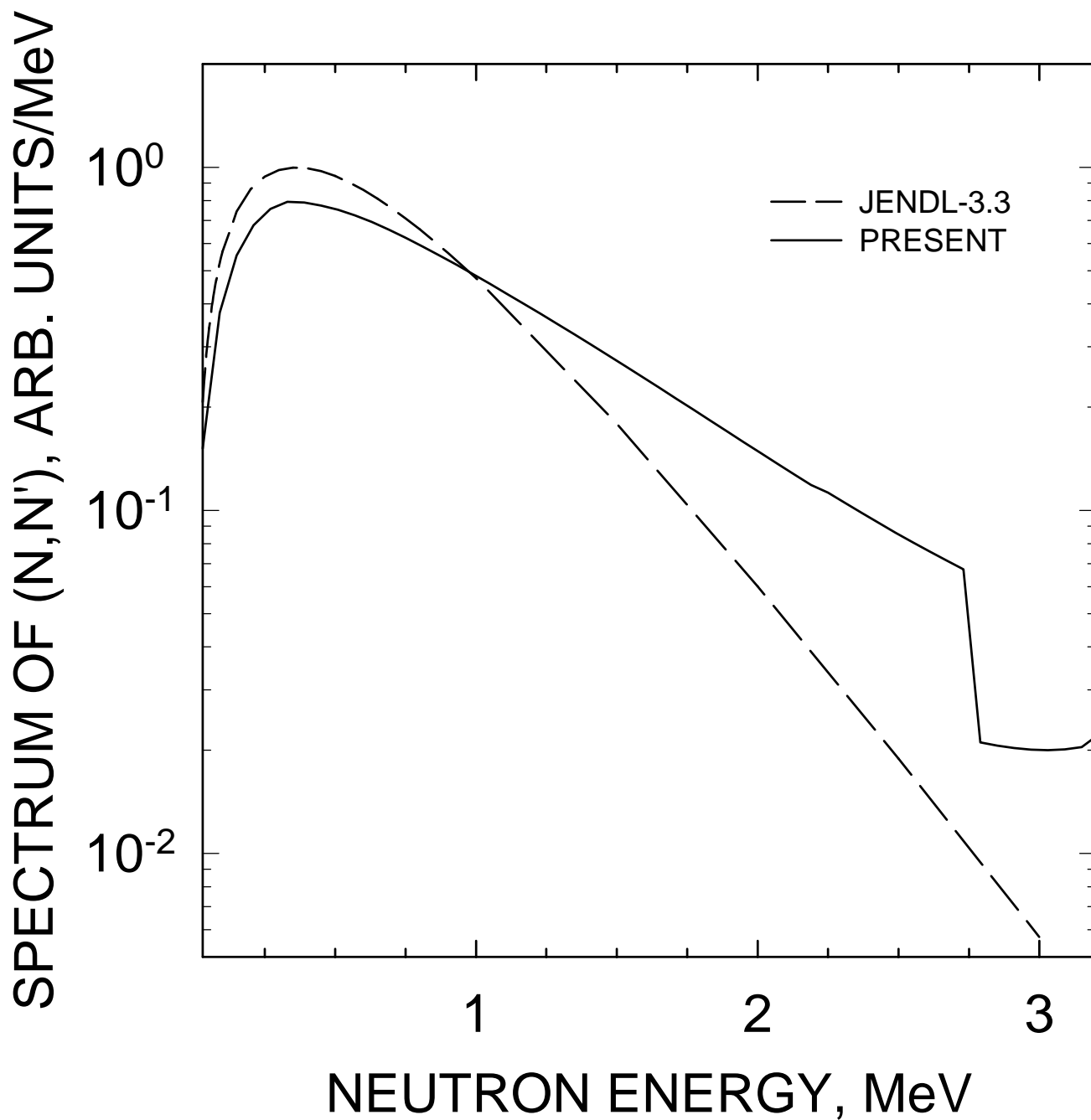


FIG. 76

$^{233}\text{Pa}$   $E_n = 20$  MeV  
COMPARISON WITH JENDL-3.3  
AND ENDF/B-VI

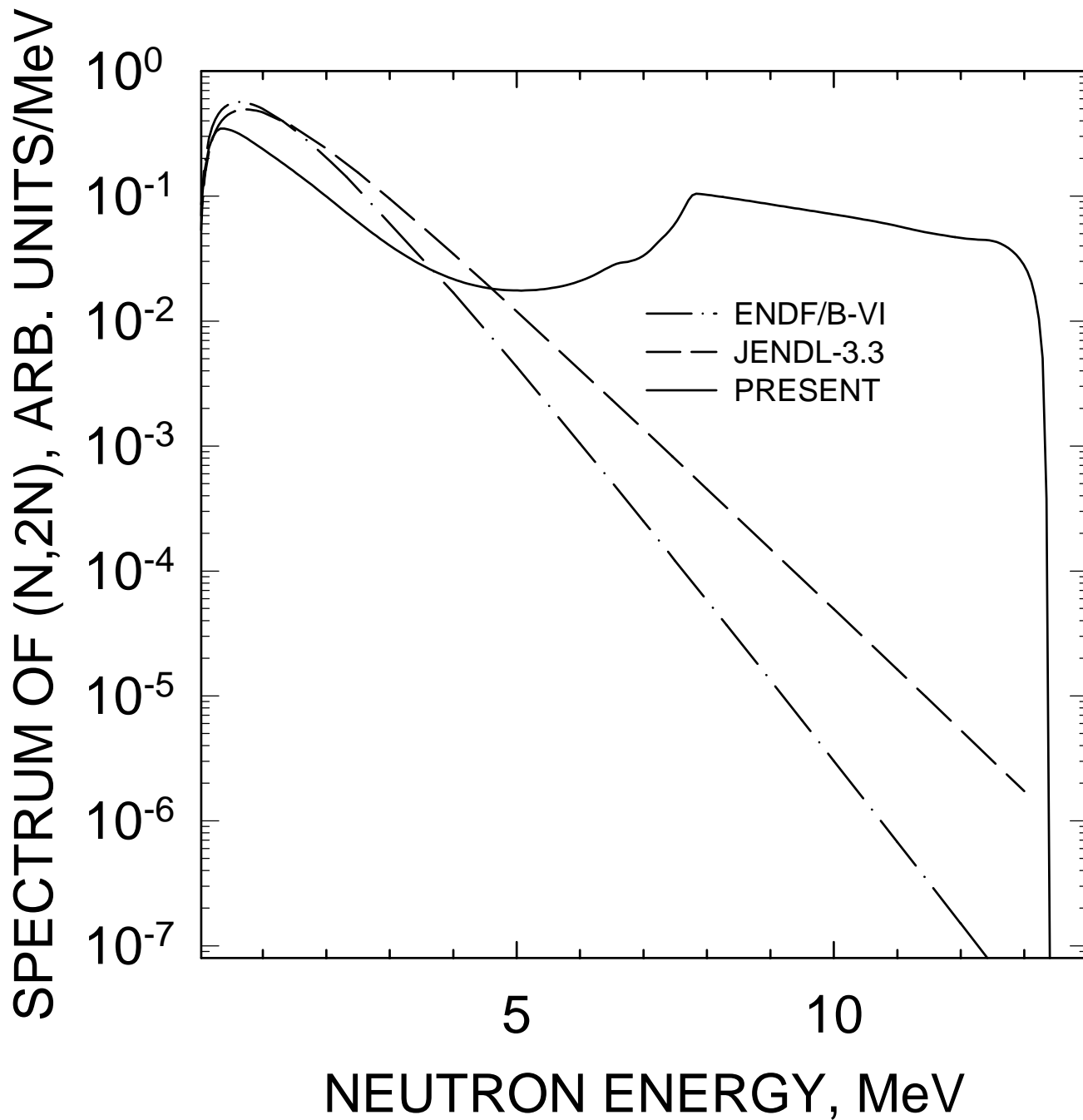


FIG. 77

$^{233}\text{Pa}$   $E_n = 14$  MeV  
COMPARISON WITH JENDL-3.3

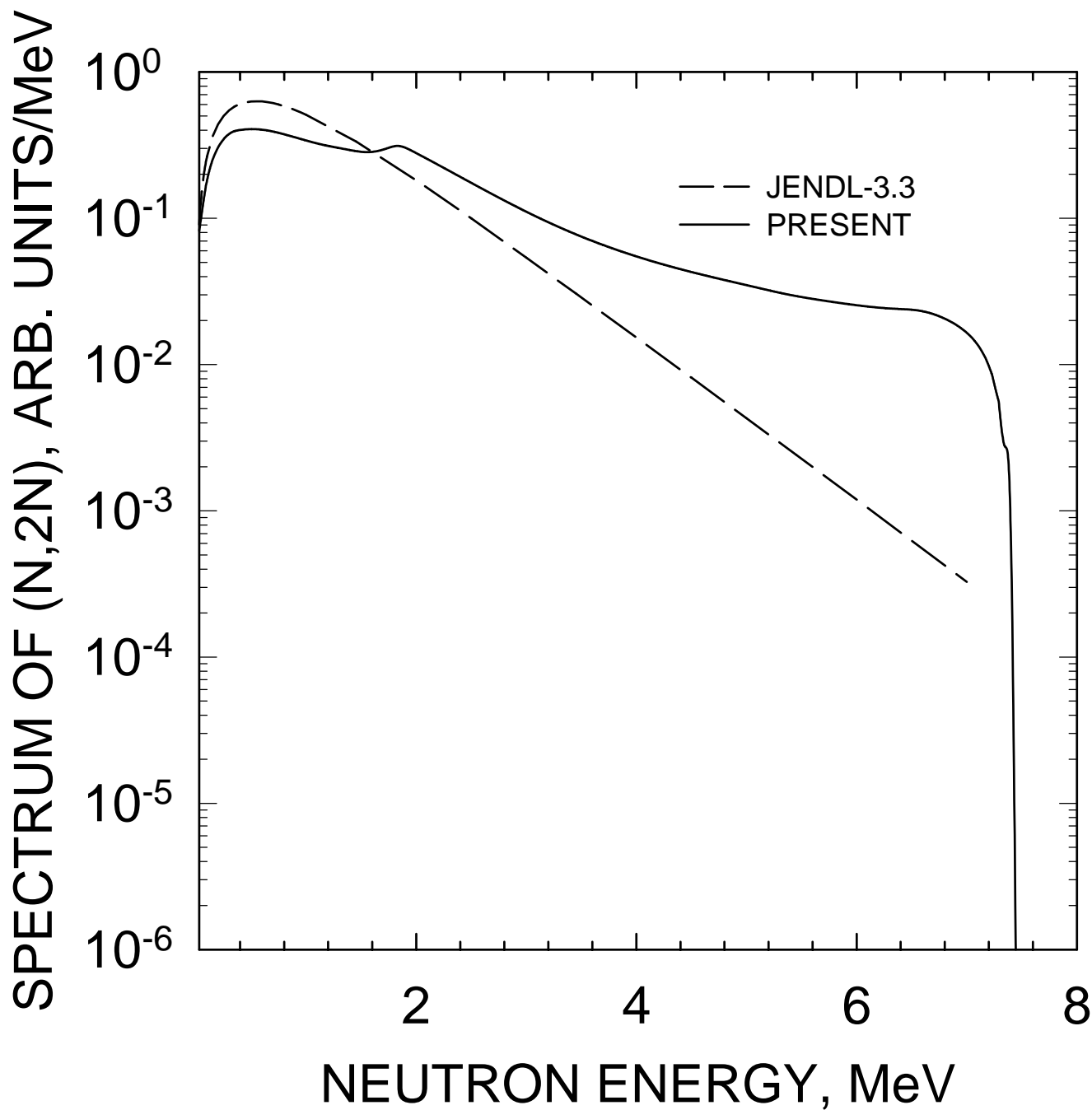


FIG. 78

$^{233}\text{Pa}$   $E_n = 10$  MeV  
COMPARISON WITH JENDL-3.3

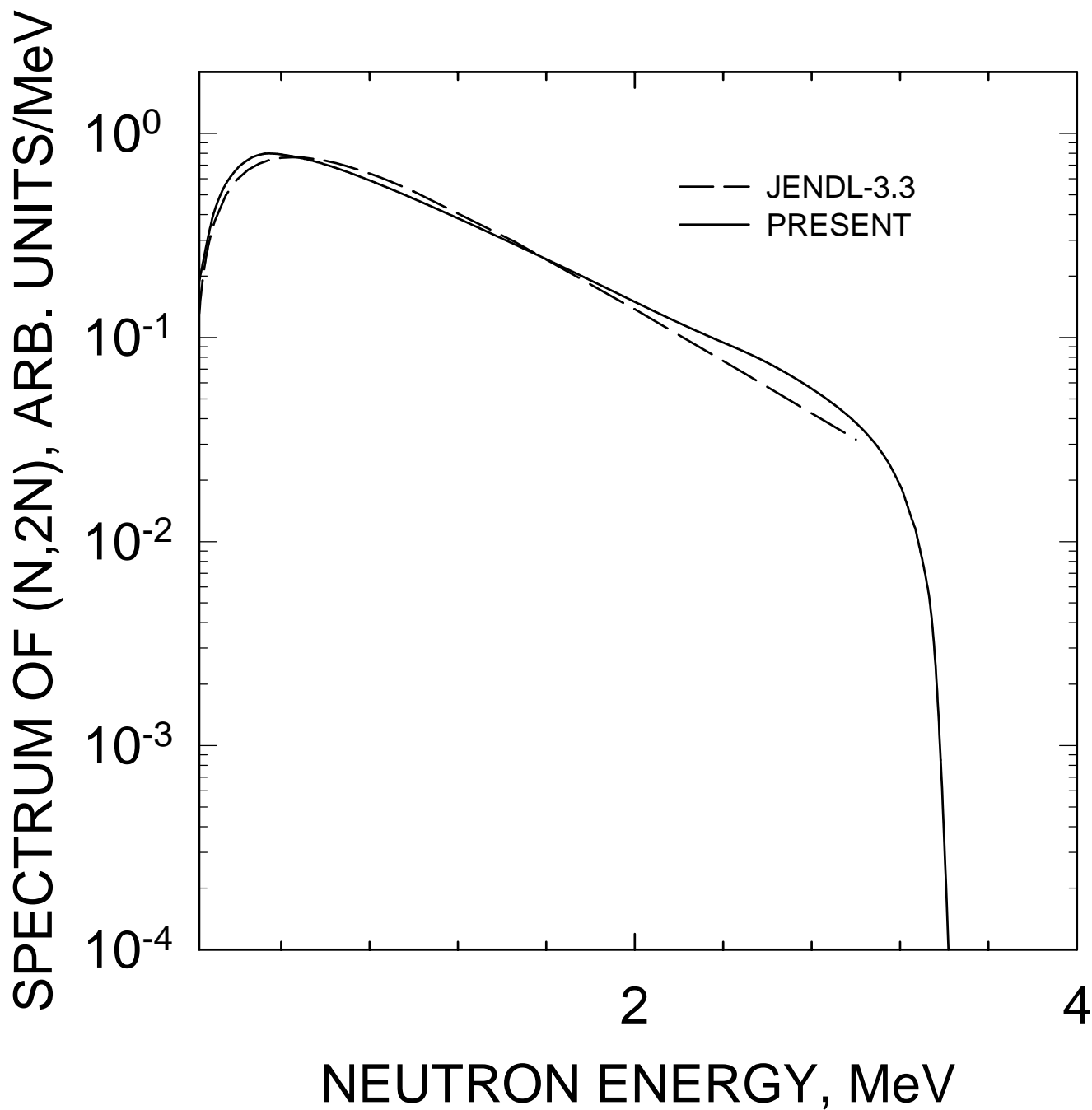


FIG. 79

$^{233}\text{Pa}$   $E_n = 20 \text{ MeV}$   
COMPARISON WITH JENDL-3.3  
AND ENDF/B-VI

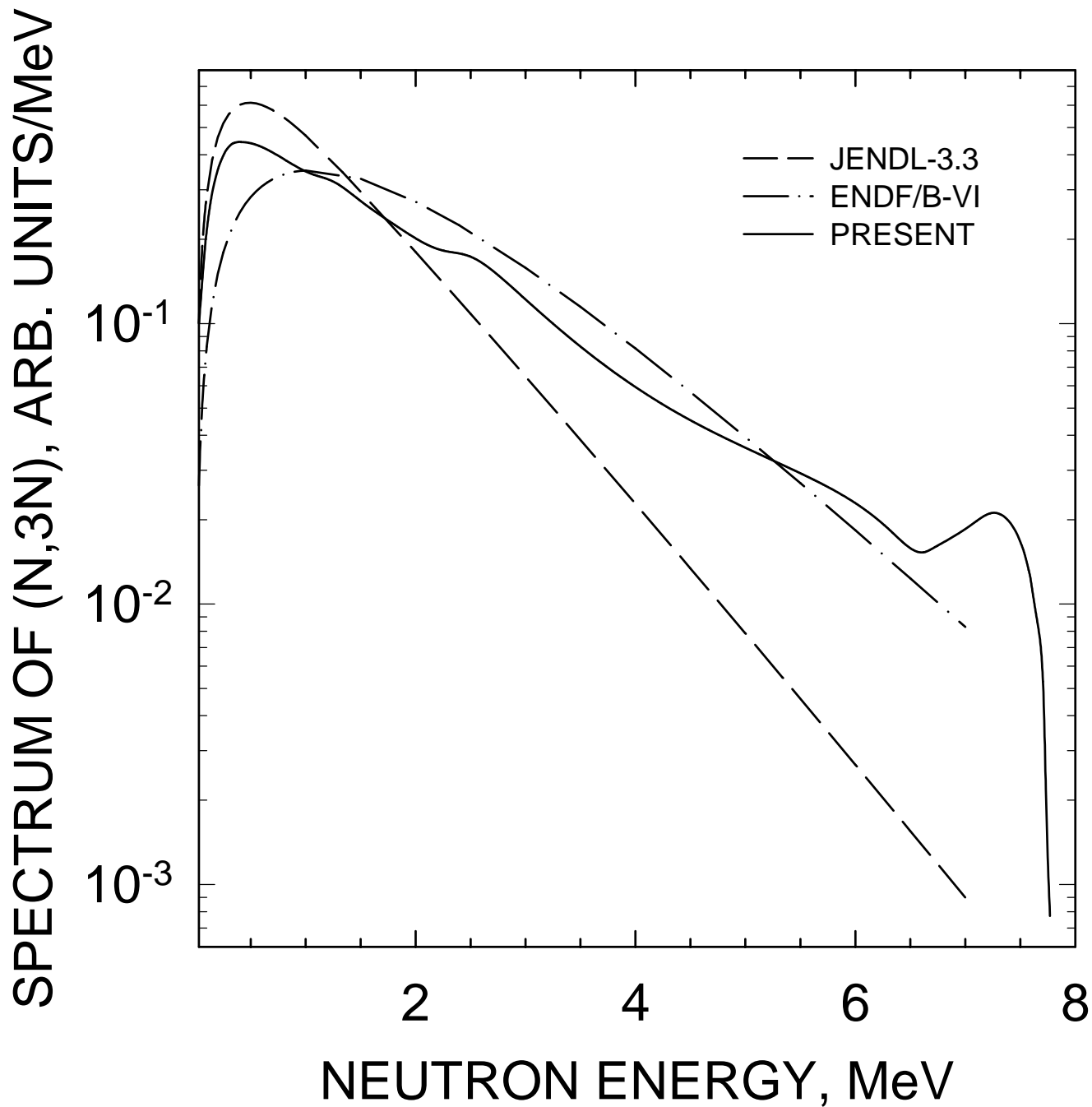


FIG. 80

$^{233}\text{Pa}$   $E_n = 14$  MeV  
COMPARISON WITH JENDL-3.3  
AND ENDF/B-VI

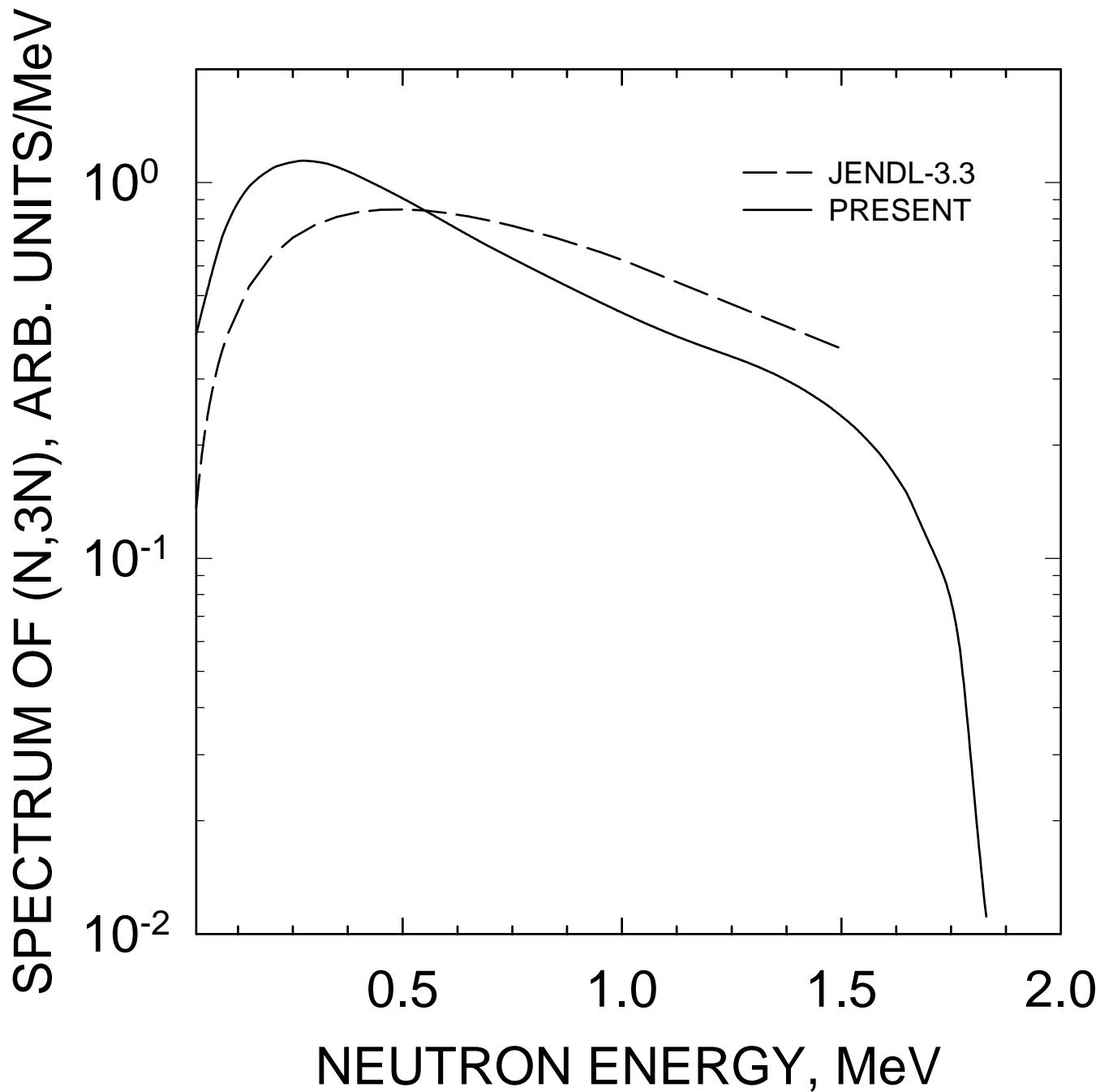


FIG. 81



---

Nuclear Data Section	e-mail: <a href="mailto:services@iaeand.iaea.org">services@iaeand.iaea.org</a>
International Atomic Energy Agency	fax: (43-1) 26007
P.O. Box 100	cable: INATOM VIENNA
A-1400 Vienna	telex: 1-12645
Austria	telephone: (43-1) 2600-21710

---

Online: TELNET or FTP: [iaeand.iaea.org](http://iaeand.iaea.org)  
username: IAEANDS for interactive Nuclear Data Information System  
usernames: ANONYMOUS for FTP file transfer;  
FENDL2 for FTP file transfer of FENDL-2.0;  
RIPL for FTP file transfer of RIPL;  
NDSOHL for FTP access to files saved in "NDIS" Telnet session.

Web: <http://www-nds.iaea.org>

---